Electro-optical simulations of organic light emitting diodes

Webster, Matthew Arthur

Award date:
2003

Awarding institution:
University of Bath

Electro-Optical Simulations of Organic Light Emitting Diodes

Matthew Arthur Webster

December 2003

Submitted in partial fulfilment of the requirements for the degree of Doctor of Philosophy at the University of Bath, Bath, England

ProQuest LLC
789 East Eisenhower Parkway
P.O. Box 1346
Ann Arbor, MI 48106-1346

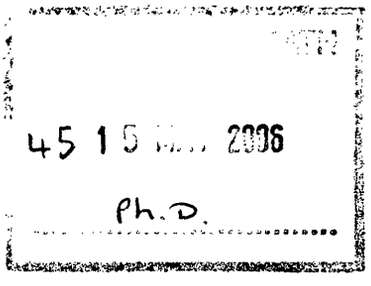
45 15 ... 2006
Ph.D.

Abstract

This work in this thesis is concerned with modelling the electrical and optical behaviour of organic light emitting diodes (OLEDs) by means of computer simulation. The electrical model is based on the drift-diffusion theory of charge transport, conventionally used when studying crystalline, inorganic semiconductors (e.g Si). This model uses the current drift-diffusion and continuity equations, along with Poisson's equation, to detail the transport of charge (electrons and holes) through a semiconductor. Charge is injected into the semiconductor through a metal contact-the metal/semiconductor interface is treated as a Schottky contact. The disordered structure of an organic semiconductor is modelled by field-dependent carrier mobilities, which are also used in the calculation of a Langevin optical recombination rate. The optical model is based on the emission of an oscillating dipole antenna within a thin-film structure. The variation of dipole emission due to microcavity effects is used to determine the behaviour of a radiatively-decaying dipole (an exciton).

Chapter 4 contains results of simulating OLEDs with the electrical model. After a brief study of two methods by which an organic heterojunction can be simulated, the model is used to study statistical copolymer and tri-layer small molecule devices. A crude approximation between recombination and photon emission is used to qualitatively reproduce experimentally observed emissive shifts for a tri-layer device. The emissive shift is attributed to the device having two seperate recombination zones with differing voltage responses.

Initial simulations of devices constructed from a novel blue copolymer showed the drift-diffusion simulation to be inadequate in reproducing experimental data. Resistive effects, ascribed to interfacial defects, were introduced into the model to explain the behaviour of degraded devices. With the inclusion of traps into the simulation an apparent relationship was derived between trap density and certain low-bias resistive effects. The explanation was proposed that impurity conduction via trap energy levels was responsible for the observed low-bias device behaviour.

Chapter 6 contains results generated with both the optical and electro-optical models. The electro-optical model was used to simulate the external quantum ef-

ficiencies of a series of bilayer devices. The simulated results were consistent with experimental measurements for equivalent devices, demonstrating the validity of the model. The sensitivity of the external quantum efficiency to parameters such as exciton diffusion length and Schottky barrier height was also investigated.

The optical and electro-optical models were then used to study anti-glare techniques. Out-coupling profiles and L-V curves were simulated for device structures incorporating a thin-metal anti-glare layer to determine an optimal device configuration.

Dedicated to Amelia.

Acknowledgements

Firstly I would like to thank my supervisor Dr Alison Walker for invaluable help and assistance over my post-graduate years, and the rest of the physics staff at Bath University, especially Eva Ashford, Peter Ford and Adrian Hooper. I would also like to thank Sharp Laboratories for their financial and scientific support. I would particularly like to express my gratitude to Dr Geraldine Verschoor and Dr Sandra Gilmour for their supervision and expertise. I would like to thank Professor Donal Bradley's group at Imperial College London for their interactions, especially Dr Riz Khan for his experimental data and insights into modelling blue polymers.

A huge amount of thanks must go to my fellow post-graduates in the group: Michael Cass for his uncanny ability to always ask the right questions, lending me a seemingly never-ending supply of science fiction and fantasy books and providing a skilled opponent at chess and go. Simon Martin for explaining how the drift-diffusion model worked, and teaching me all he knew about organic semiconductors and demonstrating those obscure but useful unix commands. Diego Oratio for showing me the right way to teach undergraduates and the value of perseverance in research. Pete Watkins for his challenging debates on philosophy and programming paradigms. James Auld for his invaluable assistance in producing quantum efficiency curves and proof-reading my thesis. I would also like to thank the originator of our model, Chris Blades, for his comprehensive look at numerical techniques and Dr Kjeld Jensen for his "test-difeq" code.

I would also like to thank my parents and my grandmother for their support and help during my student years.

Finally, I would like to conclude by thanking Amelia for her patience and encouragement (especially in the final six months of my Phd).

Contents

Chapter 1

Introduction

The study of Organic Light Emitting Devices (OLEDs) really begins in the latter half of the 1980's with the work of Tang and VanSlyke [1][2]. Pope et al [3] had observed electroluminescent behaviour in single crystals of anthracene some 25 years previously, but the large operating voltages (100V-1000V) and difficulties of manufacturing single crystals meant this approach was not suitable for practical devices. [1][2] studied electroluminescence in thin-film OLEDs whose small size ($\sim$100nm layer thickness) allowed much lower operating voltages (5V-10V). These prototypes were bi-layer small-molecule devices, with an emissive layer of tris-(8-hydroxyquinoline) aluminium (Alq) and a hole transporting layer of N,N'-diphenyl-N,N'-(3- methylphenyl) -[1,1'biphenyl]-4,4'-diamine (TPD). Burroughes et al [4] also studied thin-film OLEDs; however instead of using multiple layers of molecular materials, their devices used a single emissive layer of the polymer poly(p-phenylene vinylene) (PPV). Figure 1.1 shows the structure of the above-mentioned materials.

This demonstration that practical light-emitting devices could be fabricated from organic semiconductors provided the impetus for a large amount of research into organic materials and device construction. At the present time OLEDs have already been used in low-information content consumer applications, perhaps most famously the Philips Sensotec 8894XL shaver featured in the film "Die Another Day" . Additionally high-information content applications, such as flat-panel monitors/laptop monitors [5] are in the prototype stage. Organic semiconductors also show great promise in other electrical applications such as photovoltaics

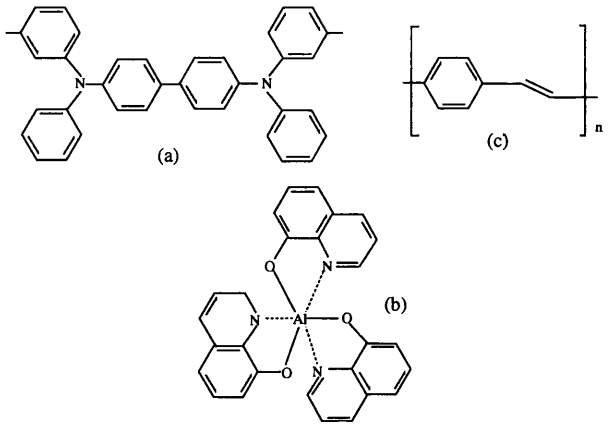

Figure 1.1: The chemical structure of three organic semiconductors TPD, Alq PPV.

[6] and lasing [7] .

Much of the commercial interest in OLEDs comes from their potential for thin, flexible, lightweight displays. Some of the key advantages of OLEDs are:

(a) They exhibit fast switching speeds ($< \mu s$) [8].

(b) The emission wavelengths can be tuned by introducing dyes (for small molecule devices) or blending (for polymers) [9].

(c) Displays can be produced with wide viewing angles.

(d) high emission efficiencies have been reached (LED's have been made that are ten times more efficient than back-lit, colour liquid crystal displays [10]).

1.1 Semiconducting behaviour in organic materials

There are two main classes of organic semiconductor - small-molecular and polymer. A common property of each class (and the fundamental reason for their semiconducting characteristics) is that they are conjugated materials; that is the carbon-carbon bonds can be seen as alternating between single and double bonds.

In a conjugated structure (such as benzene) carbon atoms form three equally spaced in-plane sp_2 hybrid orbitals and a p_z orbital which is orthogonal to the sp_2 orbital plane [11]. Overlap of the sp_2 orbitals between neighbouring carbon atoms forms strong, highly localised σ bonds. However these bonds, while being important to the molecular structure, do not contribute to electrical conduction. Instead it is the overlap of p_z orbitals, forming delocalised π-bonds which support electrical conduction [8]. Figure 1.2 illustrates the above processes.

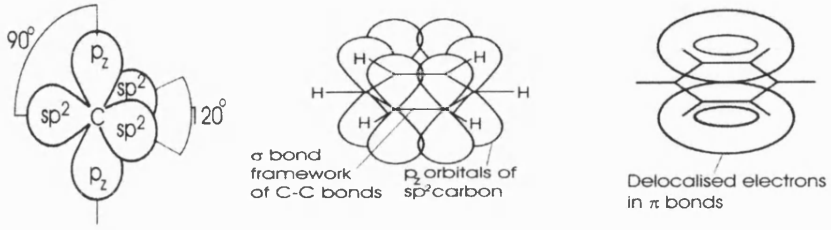

Figure 1.2: The sp^2 and p_z orbitals of a carbon atom (left), overlapping sp^2 (middle) and p_z (right) orbitals forming localised σ and delocalised π bonds respectively.

The tight-binding model [12] explains how iso-energetic states can become degenerate when they overlap. In this case the p_z orbitals overlap to form a low energy π (bonding) orbital, and a higher energy π^* (anti-bonding) orbital. If this overlap occurs over a sufficient number of states, valence and conduction bands, with a well-defined bandgap (given by $\pi - \pi^*$) are formed. The valence and conduction bands are alternatively known as the HOMO (Highest Occupied Molecular Orbital) and LUMO (Lowest Unoccupied Molecular Orbital) energy levels. Typical organic semiconductors have bandgap energies in the range 2-3eV [13], allowing emission in the visible spectrum (400-700nm). The presence of an excited state (an electron or hole) can cause distortion of the molecule or polymer where it is located. Thus as an electron or hole moves, the associated distortion will also appear to move. This combination of charge carrier and distortion is known as a polaron. For reasons of simplicity, charge carriers are referred to as electrons and hole in this thesis, and any effects due to molecular distortion are not explicitly modelled.

An organic semiconductor can be seen as consisting of a number of hopping sites (molecules or polymer segments) which vary in position and energy. Carriers are transported by tunnelling "hopping" between sites. A characteristic of transport in organic semiconductors is the field-dependence of the carrier mobilities, which has the form:

$$\mu(\mathrm{E}) = \mu_0 \exp\left(\sqrt{\frac{\mathrm{E}}{\mathrm{E}_0}}\right) \tag{1.1}$$

where $\mu(\mathrm{E})$ is the carrier mobility at a particular electric field, μ_0 is the carrier mobility for zero field, E is the electric field strength, and E_0 is a material parameter which defines the mobilities' field dependence for a particular organic semiconductor, although this is often sample dependent since it is related to the amount of disorder in a material. Compared to the mobilities in crystalline inorganic semiconductors (e.g. 0.1450 m^2/Vs for electrons in Si [14]) organic semiconductors have very low zero-field mobilities, with a range from 1×10^{-7} to 1×10^{-14} m^2/Vs [15]. This field-dependent form for carrier mobilities has been determined empirically from experimental measurements of carrier mobilities as a function of electric field [16] [17]. The field-dependent mobilities are attributed to both energetic and morphological disorder within organic semiconductors [18].

1.2 Device operation

OLEDs are manufactured from one or more organic semiconductor layers sandwiched between two electrodes. Device operation is as follows; Charges are injected from a metal contact into the organic semiconductor(s). Electrons are injected from the cathode and holes are injected from the anode. These charge carriers are transported through the organic layer(s) due to the twin processes of concentration diffusion and drifting due to an electric field. The carriers may then recombine to form a singlet or triplet exciton (a Coulombically bound electron-hole pair) which then further diffuse through the device. The singlet excitons can decay radiatively while triplets generally only decay non-radiatively. The photons produced by exciton decay may be absorbed by a metal electrode, trapped in a layer by waveguiding effects or (ideally) propagated to outside the device. The above processes are illustrated for a mono-layered device in Figures 1.3 and 1.4.

The optimum electrical efficiency is achieved if carrier injection and transport are balanced. However most materials transport one carrier preferentially (in fact, the majority of materials are hole transporters) which is why multi-layered devices, such as those originally investigated by [1], are studied as it is much

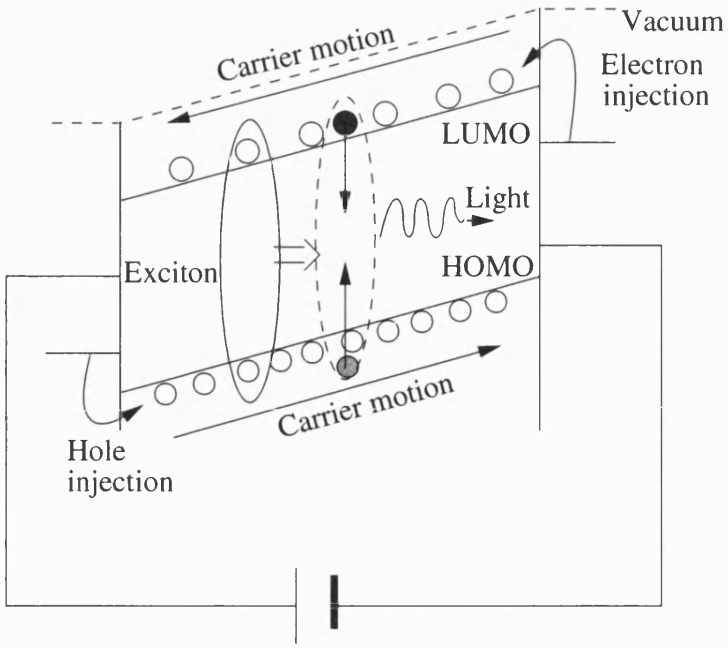

Figure 1.3: Schematic energy band diagram illustrating electrical operation for a mono-layer OLED.

easier to control charge injection/transport. Optically, the radiative efficiency of a singlet decay will vary with position through the device. Multi-layered OLEDs are again useful as they can confine the carriers to specific, optically-efficient, regions within the device.

1.3 Overview

This thesis presents work concerning the electrical and optical modelling of organic light emitting diodes (OLEDs) by means of computer simulation. The optical model is based on the emission of an oscillating dipole antenna within a thin-film structure. The variation of dipole emission due to microcavity effects is used to determine the behaviour of a radiatively-decaying dipole (an exciton). The electrical model is based on the drift-diffusion theory of charge transport, conventionally used when studying crystalline, inorganic semiconductors (e.g Si). This model uses the carrier drift-diffusion and continuity equations along with Poisson's equation, to describe the transport of charge (electrons and holes) through a semiconductor. Charge is injected into the semiconductor through a metal contact-the metal/semiconductor interface is treated as a Schottky contact.

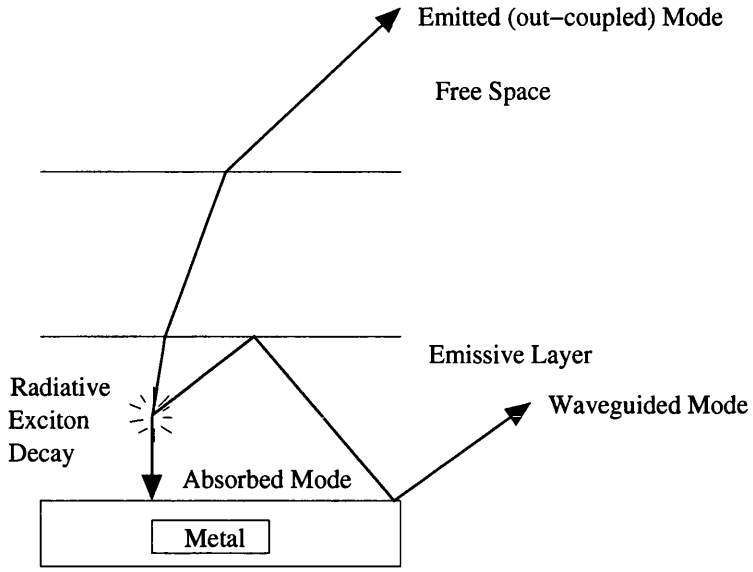

Figure 1.4: Schematic of a dielectric stack illustrating optical effects for a mono-layer OLED.

The fundamentally disordered structure of an organic semiconductor is modelled by field-dependent carrier mobilities, which are also used in the calculation of a Langevin optical recombination rate. The modelling software is a development of code previously produced by the group [19] [20]. The model itself has similarities to others in the literature e.g. [21] [22]. Much of the work described within [19] [20] was concerned with the vital tasks of validating the device model and testing its performance with various OLED structures.

Since the electrical model has been validated, the direction of research was extended to investigating the primary property of an OLED - light emission. The main goals of this work were to develop a coupled electro-optical model, capable of directly calculating the light output of a specified device. The model was used to determine material properties that were difficult or impossible to characterise experimentally. Additionally improvements were made to the numerical solver used by the simulation.

Chapter 2 contains the drift-diffusion theory used in the electrical model. Additionally there is discussion of how charge is injected into a semiconductor through a metal/semiconductor contact. Chapter 3 discusses how the simulation's numerical stability was improved by matrix preconditioning. Chapter 4 contains results obtained with the electrical model.

Chapter 5 discusses the emission of an oscillating dipole antenna within a thin-

film structure, which is the basis of the optical model, and how this relates to discrete dipole transitions. The out-coupling efficiency of a decaying exciton is determined, which in conjunction with the electrical model allows calculation of a device's photon output. Chapter 6 contains results generated with both the optical and electro-optical models.

Chapter 7 recaps the conclusions reached within the thesis, and also suggests possible avenues of future research.

References

[1] C. W. Tang and S. A. VanSlyke, "Organic electroluminescent diodes", *Appl. Phys. Lett.*, **51**, 913 (1987).

[2] C. W. Tang, S. A. VanSlyke and C. H. Chen, "Electroluminescence of doped organic thin-films", *J. Appl. Phys.*, **65**, 3610 (1989).

[3] M. Pope, H. P. Kallman and P. Magnante, "Electroluminescence in organic crystals", *J. Chem. Phys.*, **38**, 2042 (1963).

[4] J. H. Burroughes, D. D. C. Bradley, A. R. Brown, R. N. Marks, K. MacKay, R. H. Friend, P. L. Burns and A. B. Holmes, "Light-emitting diodes based on conjugated polymers", *Nature*, **347**, 539 (1990).

[5] R. Troutman, "Will OLED displays challenge liquid crystal displays in notebook computer applications", *Synth. Met.*, **91**, 31 (1997).

[6] G. G. Malliaras, J. R. Salem, P. J. Brock, and J. C. Scott, "Photovoltaic measurement of the built-in potential in organic light emitting diodes and photodiodes", *J. Appl. Phys.*, **84**, 1583 (1989).

[7] N. Tessler, "Lasers based on semiconducting organic materials", *Adv. Mater.*, **11**, 363 (1999).

[8] I. H. Campbell and D. L. Smith, "Physics of organic electronic devices", *Sol. Stat. Phys.: Adv. in Res. and Appl.*, **55**, 1 (2001).

[9] A. Shoustikov, Y. You and M.E. Thompson, "Electroluminescence color tuning by dye doping in organic light-emitting diodes", *I.E.E.E. J. Spec. Top. Quantum. Electr.*, **4**, 3 (1998).

[10] R. Friend, J. Burroughes and T. Shimoda, "Polymer diodes", *Physics World*, June, 35 (1999)

[11] K. C. Kao and W. Hwang, *Electrical Transport In Solids: with particular reference to organic semiconductors*, Pergamon Press, Oxford (1981).

[12] J. R. Hook and H. E. Hall, *Solid State Physics*, 2nd. ed., John Wiley and Sons, ew York (1991).

[13] G. Hadziioannou and P. F. van Hutten (eds.), *Semiconducting Polymers: Chemistry, Physics and Engineering*, 445, Wiley-VCH, Weinheim (2000).

[14] S. M. Sze, *Physics of Semiconductor Devices*, 2nd. ed., John Wiley and Sons, New York (1981).

[15] M. T. Bernius, M. Inbasekaran, J. O'Brien and W. Wu, "Progress with light-emitting polymers", *Adv. Mat.*, **12**, 1737 (2000).

[16] P. W. M. Blom, H. C. F. Martens, and J. N. Huiberts, "Frequency dependent carrier mobility in polymer LED's", *Synth. Met.*, **121**, 1621 (2001).

[17] W. Brütting, S. Berleb, and A. G. Mückl, "Device physics of organic light-emitting diodes based on molecular materials", *Org. Electron.*, **2**, 1 (2001).

[18] H. Bässler, "Charge transport in disordered organic photoconductors - a Monte-Carlo simulation study", *Phys. Stat. Solidi B*, **175**, 15, (1993).

[19] C. D. J. Blades, *Ph.D. Thesis*, University of Bath (2000).

[20] S. J. Martin *PhD Thesis*, University of Bath, (2002)

[21] P. S. Davids, I. H. Campbell, and D. L. Smith, "Device model for single carrier organic diodes", *J. Appl. Phys.*, **82**, 6319 (1997).

[22] G. G. Malliaras and J. C. Scott, "The roles of injection and mobility in organic light emitting diodes", *J. Appl. Phys.*, **83**, 5399 (1998).

Chapter 2

The Band Model of Charge Transport and Injection

In this section the theory behind the drift-diffusion model is discussed. There are two fundamental processes that occur in the electrical operation of an OLED: injection of carriers into an organic layer from a metal contact and transport of carriers through a semiconductor layer. For crystalline inorganic semiconductors these processes are described by the energy band model [1]. Since this model is well understood and detailed in many sources (e.g.[1]) only the key concepts/modifications pertaining to the simulation of organic semiconductors will be covered in this section.

The energy band model has been successfully applied to organic semiconductors by numerous groups (e.g [2],[3],[4],[5],[6]) and has shown itself to be a useful tool in understanding OLED behaviour. A number of modifications, most notably the inclusion of field-dependent mobilities, have been made to more accurately model organic devices.

The first part of this chapter is concerned with metal-semiconductor contacts and the derivation of analytical expressions for the device current. The second part discusses charge transport within a semiconductor and between semiconductor layers.

2.1 Metal-Semiconductor contacts

When a metal comes into contact with a semiconductor, several conditions must be met to produce thermal equilibrium. In particular, the vacuum and Fermi levels must be continuous across the contact which is achieved by the transfer of charge between the two materials. This process results in the formation of an energy barrier between the metal and the semiconductor, the size of which is typically equal to the difference between the band edge and the metal's workfunction [1]. Metal/semiconductor contacts of this type are termed Schottky contacts and the energy barrier is likewise labelled a Schottky barrier.

The magnitude of the Schottky barriers to electron and hole injection, ϕ_{Bn} and ϕ_{Bp}, are given by

$$\phi_{Bn} = (\phi_m - \chi) \tag{2.1}$$

$$\phi_{Bp} = E_g - (\phi_m - \chi) \tag{2.2}$$

where ϕ_m is the metal's workfunction, χ is the semiconductor's electron affinity (the energy of the LUMO level) and E_g is the semiconductor's band gap. By substituting Equation 2.1 into Equation 2.2 it is possible to relate ϕ_{Bn} to ϕ_{Bp}:

$$\phi_{Bn} = E_g - \phi_{Bp} \tag{2.3}$$

Inorganic metal semiconductor contacts are commonly labelled n- or p-type, according to the semiconductor's doping characteristics, and display significant band bending at equilibrium, due to the magnitude of the charge-densities involved. An organic semiconductor typically has little or no doping, which in conjunction with a band gap in excess of 2.5eV results in the material containing virtually no intrinsic carriers (and so is said to be fully depleted). Due to this lack of intrinsic carriers, metal/organic semiconductor contacts can be classified as neutral/intrinsic contacts and display no band-bending at equilibrium. This

"rigid" band structure is shown for a metal/semiconductor/metal structure in Figure 2.1.

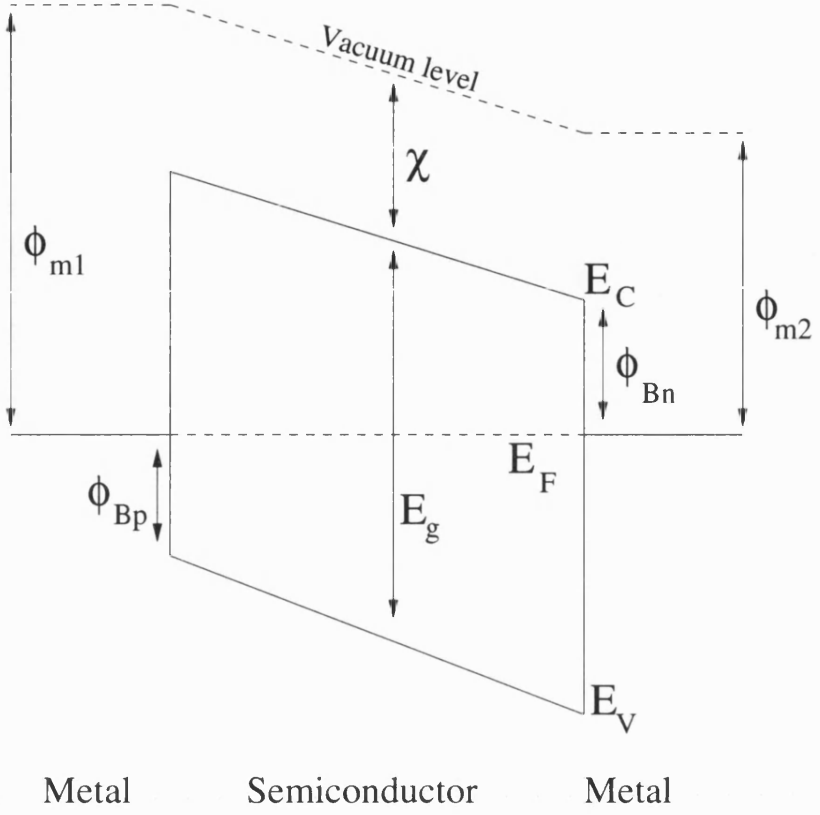

Figure 2.1: Band structure for a metal/semiconductor/metal contact

An important quantity for an OLED is the built-in voltage, caused by a potential difference between the metal-semiconductor contacts. Referring to Figure 2.1 the built-voltage and corresponding built-in field , denoted as V_{bi} and E_{bi}, are given by:

$$V_{bi} = \frac{1}{q}(\phi_{m2} - \phi_{m1}) \tag{2.4}$$

$$\mathrm{E}_{bi} = -\frac{V_{bi}}{d} \tag{2.5}$$

where d is the semiconductor's thickness.

V_{bi} and E_{bi} can deviate from the above definition due to interfacial effects (dipole

layers etc.) [7]. However experimental measurements of V_{bi} generally agree with Equation 2.4 (e.g. [8, 9]).

Figures 2.2 and 2.3 illustrate how a device's band structure varies with applied bias. At a small forward bias the device's negative built-in electric field opposes transport of injected carriers, resulting in a small current. As the bias increases so does the absolute magnitude of the electric field until ,for an applied bias equal to the built-in voltage, the electric field reaches zero. For forward bias' in excess of the built-in voltage, a high current ensues due to the device's positive electric field and reduced potential barriers. For reverse bias the device's negative electric field increases with the applied bias, which now assists carrier transport (since the direction of carrier flow is reversed). However the increased Schottky barriers (due to the rectifying nature of a Schottky contact) mean that few carriers are injected into the device, and hence the device current is small.

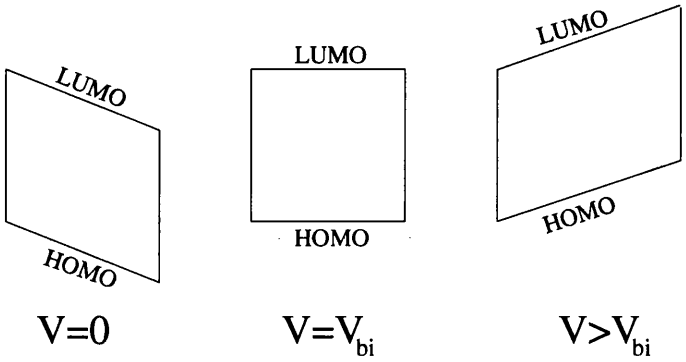

Figure 2.2: Band structure schematic for forward bias operation

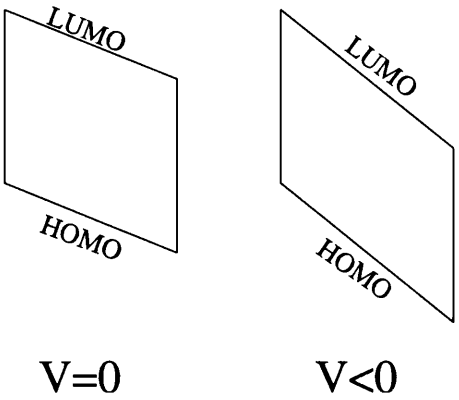

Figure 2.3: Band structure schematic for reverse bias operation

2.2 Carrier transport across a metal/semiconductor contact

There are several processes by which carriers can be transported across a metal semiconductor contact:

1) Thermionic emission of carriers over a Schottky barrier

2) Interface generation and recombination

3) Tunnelling emission of carriers through a Schottky barrier

4) Tunnelling emission of carriers into interface states

Only the first 3 mechanisms are discussed in this section

2.2.1 Thermionic emission

If a carrier's kinetic energy is sufficiently large it can cross over the potential barrier at a Schottky contact. The simplest version of the thermionic emission theory assumes that electrons and holes within a semiconductor propagate freely in their respective bands and have a thermal distribution of kinetic energies. The resultant current is the difference between two opposing carrier flows - one from the metal to the semiconductor and one from the semiconductor to the metal. For zero applied bias these two currents are equal and opposite, resulting in no net charge transport.

For a n-type contact the current flowing from the semiconductor to the metal is given by

$$J_{s\rightarrow m} = A_n^* T^2 \exp\left(\frac{qV_{app} - \phi_{Bn}}{k_B T}\right) \tag{2.6}$$

where A_n^* is the Richardson constant for electrons (equal to $(4\pi q m_n^* k_B^2)/(h^3)$), T is the absolute temperature, k_B is Boltzmann's constant, q is the electronic charge, m_n^* is the effective electron mass, h is Planck's constant and V_{app} is the

applied bias.

Similarly, the electron current flowing from the metal to the semiconductor is given by:

$$J_{m\to s} = -A_n^* T^2 \exp\left(\frac{-\phi_{Bn}}{k_B T}\right) \tag{2.7}$$

The resultant electron current, J_n, is given by the difference between Equations 2.7 and 2.6:

$$J_n = A_n^* T^2 \exp\left(\frac{-\phi_{Bn}}{k_B T}\right)\left[\exp\left[\frac{qV_{app}}{k_B T}\right] - 1\right] \tag{2.8}$$

For a p-type contact the resultant hole current, J_p is calculated in a similar fashion.

2.2.2 Thermionic emission-diffusion

In the case of low carrier mobilities (such as in organic semiconductors) the assumption of freely propagating carriers does not hold, due to the build up of carriers at the contact. The thermionic emission-diffusion theory [1] combines the thermionic emission model with transport of carriers in the depletion region. The current is now due to both thermionic emission across the Schottky barrier and drift-diffusion (discussed in Section 2.3) within the drift depletion region. This model uses the concept of electron and hole surface recombination velocities ,v_{rn} and v_{rp}, defined at the location of the Schottky barrier potential maximum, x_m.

For an n-type device the drift-diffusion current, J_{dd}, in the depletion region is given by:

$$J_{dd} = -q\mu_n n(x)\frac{\mathrm{d}\phi_n(x)}{\mathrm{d}x} \tag{2.9}$$

where μ_n is the electron mobility, ϕ_n is the electron quasi-Fermi level, and n is the electron density, given by:

$$n = N_C \exp\left(\frac{-\left[q\psi\left(x\right) - \phi_n\left(x\right)\right]}{k_B T}\right) \tag{2.10}$$

where N_C is the density of states in the conduction band, and ψ is the electrostatic potential.

The region between the metal-semiconductor contact and the potential energy maximum is assumed to be a perfect sink of electrons, such that the current flow in this region, J_{br}, is given by:

$$J_{br} = q v_{rn}\left(n_{eq} - n_m\right) \tag{2.11}$$

where n_{eq} is the quasi-equilibrium electron density at x_m:

$$n_{eq} = N_C \exp\left(\frac{-\phi_{Bn}}{k_B T}\right) \tag{2.12}$$

and n_m is the electron density at the point x_m for an applied bias:

$$n_m = N_C \exp\left(-\left[\frac{\phi_{Bn} - \phi_n\left(x_m\right)}{k_B T}\right]\right) \tag{2.13}$$

and v_{rn} is given by

$$\frac{A_n^* T^2}{q N_C} \tag{2.14}$$

Equations 2.9 and 2.13 can be combined (by assuming continuity of current) to give the thermionic emission-diffusion current [10][11]:

$$J = \frac{qN_c v_{rn}}{1 + (v_{rn}/v_D)} \exp\left[-\frac{\phi_{Bn}}{k_B T}\right]\left[\exp\left(\frac{-qV_{app}}{k_B T}\right) - 1\right] \tag{2.15}$$

where v_D is the effective diffusion velocity for electrons in the depletion region given by:

$$v_D = \left[\int_0^\infty \frac{q}{\mu_n k_B T} \exp\left[-\frac{(\phi_{Bn} + q\psi)}{k_B T}\right] dx\right]^{-1} \tag{2.16}$$

For the case where $v_{rn} \gg v_D$, the contact is drift-diffusion limited and so equation 2.15 tends to [1]:

$$J \approx qN_c \mu_n \mathrm{E}_{contact} \exp\left(\frac{-\phi_{Bn}}{k_B T}\right)\left[\exp\left(\frac{-qV_{app}}{k_B T}\right) - 1\right] \tag{2.17}$$

where $\mathrm{E}_{contact}$ is the electric field at the contact.

For the case where $v_D \gg v_{rn}$, drift can be neglected and equation 2.15 reduces to the thermionic emission current:

$$J \approx qN_c v_{Rn} \exp\left(\frac{-\phi_{Bn}}{k_B T}\right)\left[\exp\left(\frac{-qV_{app}}{k_B T}\right) - 1\right] \tag{2.18}$$

$$\approx A_n^* T^2 \exp\left(\frac{-\phi_{Bn}}{k_B T}\right)\left[\exp\left(\frac{-qV_{app}}{k_B T}\right) - 1\right] \tag{2.19}$$

2.2.3 Tunnelling

The quantum mechanical probability of a carrier tunnelling through the barrier (as opposed to being thermionically emitted over it) increases as the barrier becomes thinner. The thickness of the barrier decreases with increasing doping, and for a highly doped metal-semiconductor contact it is possible that tunnelling can become the dominant injection mechanism.

If the majority of carriers tunnel at energies roughly equal to the Fermi level, the tunnelling mechanism is labelled field emission. Alternatively, if the majority of carriers tunnel at energies between the top of the barrier and the Fermi level, the mechanism is labelled thermionic field emission [11]. For organic semiconductors, which are essentially undoped, tunnelling current becomes dominant for low temperature, low barrier height contacts at high electric field. This means that field emission will be the dominant tunnelling mechanism and device currents can be calculated using the Fowler-Nordheim formalism [12].

The Fowler Nordheim current density due to carriers tunnelling through a potential barrier of height C can be expressed as [12]:

$$J = \frac{16\pi m_n q}{Ch^3} \int_0^{\mu} W^{1/2}(C-W)^{1/2}(\mu - W) \exp\left(-\frac{4\kappa(C-W)^{3/2}}{3\mathrm{E}}\right) \mathrm{d}W \quad (2.20)$$

where μ is the chemical potential, W is the electron kinetic energy normal to the barrier, $\kappa = 8\pi^2 m/h^2$, and E is the electric field.

Equation 2.20 can be re-arranged and integrated [13] [14] to give:

$$J = \frac{q^3}{8\pi h \phi_{Bn}} \mathrm{E}^2 \exp\left[-\frac{8\pi\sqrt{2m^*}\phi_{Bn}^{3/2}}{3\mathrm{E}qh}\right] \quad (2.21)$$

where E is the electric field at the contact.

2.2.4 Ohmic Contacts

An Ohmic contact is defined as a metal-semiconductor contact that has a negligible resistance relative to the bulk resistance of the semiconductor [1]. Ohmic contacts are commonly characterised by their specific contact resistance, R_C, which is calculated by taking the reciprocal of the current-voltage derivative at zero bias:

$$R_C = \left(\frac{\partial J}{\partial V}\right)^{-1}_{V=0} \tag{2.22}$$

For the case where thermionic emission is the dominant current transport mechanism, such as for a negligibly doped metal/semiconductor contact, R_C is obtained by substituting Equation 2.8 into Equation 2.22.

$$R_C = \frac{k_B}{qA^*T} \exp\left(\frac{\phi_{Bn}}{k_B T}\right) \tag{2.23}$$

For the case where tunnelling is the dominant transport mechanism (such as a highly doped metal/semiconductor contact), R_C is obtained by substituting Equation 2.21 into Equation 2.22.

$$R_C = \exp\left[\frac{2\sqrt{\epsilon m^*}}{\hbar}\left(\frac{\phi_{Bn}}{\sqrt{N_D}}\right)\right] \tag{2.24}$$

where ϵ is the relative permittivity of the semiconductor.

The above equations show that the contact resistance increases with Schottky barrier height and decreases with doping. Thus for a contact to behave as an Ohmic contact it must be either highly doped or have a small difference between the metal-semiconductor workfunctions (or both). For the majority of organic semiconductors it is difficult to achieve stable and consistent electronic doping, which means that the anode and cathode metals are chosen such that their workfunctions are as close to the semiconductor's HOMO and LUMO energies as possible. Generally a barrier height of less than 0.3eV will produce an Ohmic contact.

Another technique used to create an Ohmic contact in organic devices is to introduce a heavily doped surface layer between the metal and the semiconductor, forming metal-n^+-n-type or metal-p^+-p-type structures. This technique is also applicable to organic semiconductors, in particular by doping PEDOT with a high concentration of PSS, and placing it as a surface layer between an anode (usually ITO) and a semiconductor, has been shown to produce an Ohmic contact

[e.g [15]].

2.2.5 Analytical modelling

A device can be seen as being injection- or space-charge limited, that is the limiting factor on the current at a particular bias is either due to the transport characteristics of the metal-semiconductor contact or the bulk semiconductor.

In general the equations governing charge transport of a device are highly non-linear making exact analytic solutions impossible. However it is possible to derive analytic solutions if simplifying assumptions are made about a device's electrical properties.

If a device's electron and hole Schottky barrier heights, ϕ_{Bn} and ϕ_{Bp}, are greater than roughly 0.3eV then the system can be described as injection-limited. In this case the total current flowing through the device at a sufficiently large applied bias is the sum of the electron and hole reverse-bias saturation currents.

$$J_{tot} = A_n^* T^2 \exp\left(\frac{-\phi_{Bn}}{k_B T}\right) + A_p^* T^2 \exp\left(\frac{-\phi_{Bp}}{k_B T}\right) \tag{2.25}$$

where A_p^* is the Richardson constant for holes (equal to $(4\pi q m_p^* k_B^2)/(h^3)$) and m_p^* is the effective hole mass.

If at least one of the contacts can be classified as Ohmic (see Section) then the device can be described as space-charge limited. Space-charge limited current (SCLC) occurs when a metal-semiconductor contact can inject an essentially unlimited amount of carriers, causing a build-up of space charge within semiconductor, which acts to oppose further carrier injection. For a unipolar (i.e. electron- or hole-dominated) system the total current flowing at an applied bias for a space-charge limited system is given by [16]:

$$J_{tot} = \frac{9}{8}\epsilon\mu_{n/p}\frac{V_{app}^2}{d^3} \tag{2.26}$$

which is known as the Mott and Gurney equation.

Equation 2.26 is based on a number of assumptions. The semiconductor's intrinsic carrier density is assumed to be negligible. One contact is assumed to be perfectly Ohmic, while the other is a perfect sink for injected carriers. Additionally the electric field is assumed to be sufficiently high that the current within the semiconductor is drift dominated (the diffusion component is taken to be negligible - see Section 2.2.2). The electric field at the Ohmic contact is taken to be zero, implying flat bands at the contact.

Since organic carrier mobilities are field-dependent Equation 2.26 can be restated in terms of the zero-field mobility [17]:

$$J_{tot} = \frac{9}{8}\epsilon\mu_{n0/p0}\frac{V^2}{d^3}\exp\left(0.89\sqrt{\frac{V}{d\mathrm{E_{n0/p0}}}}\right) \tag{2.27}$$

where $\mu_{n0/p0}$ is the zero-field electron/hole mobility and $\mathrm{E_{n0.p0}}$ gives the field-dependence of the electron/hole mobility.

Equation 2.26 can also be extended for the case of bipolar space-charge limited current by using an effective carrier mobility μ_{eff} [18]:

$$J = \frac{9}{8}\epsilon\mu_{eff}\frac{V^2}{d^3} \tag{2.28}$$

where μ_{eff} is equal to

$$\mu_{eff} = \frac{2}{3}\left[\frac{4\pi q\mu_n\mu_p\left(\mu_n+\mu_p\right)}{\epsilon < v\sigma_R >}\right]^{\frac{1}{2}} \tag{2.29}$$

where v is the drift velocity of the carriers, and σ_R is the recombination cross-sectional area.

The above expressions can be very useful in determining OLED parameters, such as barrier height or carrier mobility, from current-voltage measurements. Some

groups have assumed space-charge limited behaviour to fit experimental data [19][20], while other groups, assuming injection-limited behaviour, have fitted data using thermionic emission (e.g. [21] [22] [23]) or Fowler-Nordheim tunnelling (e.g. [24]). The devices studied were typically unipolar single-layer systems.

While these analytical techniques can assist in characterising certain parameters, they suffer from certain disadvantages and limitations. Contacts must be classified as injection- or space-charge limited before analysis and fitting can begin; in practice this is an over-simplification. Erroneous classification of a contact will lead to errors in determining parameter values. Analytic expressions also tend to be limited in the ranges of voltage or temperature that they can accurately fit, and have difficulties with multi-layer and/or bipolar systems. Perhaps the key limitation of analytical techniques is that they cannot easily provide spatially dependent quantities such as recombination profiles. For a fully predictive simulation that can determine luminescent output, detailed information is required about a device's internal properties, for which computational methods must be used.

2.3 The drift-diffusion model

The drift-diffusion model describes the non-equilibrium behaviour of injected charge carriers within a semiconductor, under the influence of an external electric field[25]. For simplicity the one-dimensional time-independent version of the model is used in the simulation. Since a typical device cross-section a few mm^2, while the semiconductor layers are usually under 100 nanometers thick, this is a reasonable assumption. The time-independent version is used since this work is concerned with steady-state OLED operation.

The model essentially consists of six first-order differential equations; the drift-diffusion equations themselves, representing charge transport, the continuity equations which relate spatial variations in current density to recombinative processes and Poisson's equation, relating the charge density to electric field and potential.

The effect of the metal-semiconductor contacts (discussed in the previous section)

are included as boundary conditions to the equations. A computational method by which these equations are solved is detailed in the next chapter.

2.3.1 Poisson's equation

Poisson's equation relates the electrostatic potential, ψ, with the charge density ρ and the electric field, E;

$$\frac{\mathrm{d}E}{\mathrm{d}x} = -\frac{\mathrm{d}^2\psi}{\mathrm{d}x^2} = \frac{\rho}{\epsilon} \tag{2.30}$$

where ϵ is the permittivity (equal to $\epsilon_0\epsilon_s$), ϵ_0 is the vacuum permittivity, ϵ_s is the semiconductor's dielectric constant. The charge density is given by

$$\rho = q(p - n + N_{dop} + N_{trap}) \tag{2.31}$$

where q is the electronic charge, n and p are the electron and hole concentrations, where N_{dop} is the net charge contribution due to ionised acceptor and donor impurities. N_{trap} is the net charge contribution due to traps (discussed in Section 2.3.4).

The equations relating electron and hole densities to the electrostatic potential are obtained from Maxwell-Boltzmann statistics [1];

$$n = N_C \exp\left[\frac{1}{k_B T}(q\psi - \phi_n + \chi)\right] \tag{2.32}$$

$$p = N_V \exp\left[-\frac{1}{k_B T}(q\psi - \phi_p + E_g + \chi)\right] \tag{2.33}$$

where N_C and N_V are the conduction band and valence band density of states,ϕ_n and ϕ_p are the electron and hole quasi-Fermi levels respectively, χ is the electron affinity, E_g the energy gap, k_B is the Boltzmann constant and T the absolute temperature.

The simulation uses the electric displacement, D, which is continuous between material interfaces [26][27], rather than the electric field, where:

$$\mathbf{D} = \epsilon \mathrm{E} \tag{2.34}$$

2.3.2 Drift-diffusion equations

Within a semiconductor the electron and hole current densities J_n and J_p can be expressed as the sum of two current densities; drift (the movement of carriers due to an electric field) and diffusion (the movement of carriers due to a concentration gradient).

$$J_n = q\mu_n n\mathrm{E} + qD_n \frac{\mathrm{d}n}{\mathrm{d}x} \tag{2.35}$$

$$J_p = q\mu_p p\mathrm{E} - qD_p \frac{\mathrm{d}p}{\mathrm{d}x} \tag{2.36}$$

where μ_n and μ_p are the electron and hole mobilities and D_n and D_p are the electron and hole diffusion coefficients. For a non-degenerate semiconductor the diffusion coefficients can be related to the mobilities by the Einstein relationship:

$$D_n = \left(\frac{k_B T}{q}\right) \mu_n \tag{2.37}$$

$$D_p = \left(\frac{k_B T}{q}\right) \mu_p \tag{2.38}$$

By substituting equations 2.37 and 2.38 into 2.35 and 2.36 respectively yields:

$$J_n = q\mu_n \left(n\mathrm{E} + \frac{k_B T}{q} \frac{\mathrm{d}n}{\mathrm{d}x}\right) \tag{2.39}$$

$$J_p = q\mu_p \left(p\mathrm{E} - \frac{k_B T}{q} \frac{\mathrm{d}p}{\mathrm{d}x}\right) \tag{2.40}$$

If equations 2.32 and 2.33 are substituted into equations 2.39 and 2.40 respectively, a more compact form for the drift-diffusion equations can be obtained, which are more stable for numerical simulations [26]:

$$J_n = -qn\mu_n \frac{\mathrm{d}\phi_n}{\mathrm{d}x} \tag{2.41}$$

$$J_p = -qp\mu_p \frac{\mathrm{d}\phi_p}{\mathrm{d}x} \tag{2.42}$$

note that ϕ_n and ϕ_p are expressed in eV in the above equations.

The field-dependence of the electron and hole mobilities must be taken into account. (assuming constant temperature)

$$\mu_n(\mathrm{E}) = \mu_{n0} \exp\left(\sqrt{\frac{\mathrm{E}}{\mathrm{E_{n0}}}}\right) \tag{2.43}$$

where μ_{n0} and μ_{p0} are the zero-field electron and hole mobilities and $\mathrm{E_{n0}}$ and $\mathrm{E_{p0}}$ give the field-dependence of the electron and hole mobilities.

2.3.3 Continuity equations

The electron and hole current-densities flowing through a device can change due to recombination and generation:

$$\frac{\mathrm{d}J_n}{\mathrm{d}x} = -q(G - R) \tag{2.44}$$

$$\frac{\mathrm{d}J_p}{\mathrm{d}x} = q(G - R) \tag{2.45}$$

where G is the electron-hole pair generation rate and R is the recombination rate. Assuming that no generation processes occur, the above equations can be simplified:

$$\frac{\mathrm{d}J_n}{\mathrm{d}x} = qR \tag{2.46}$$

$$\frac{\mathrm{d}J_p}{\mathrm{d}x} = -qR \tag{2.47}$$

R has contributions from trapping and optical processes. The optical recombination rate, R_{opt}, has a bimolecular form with a Langevin recombination coefficient, γ:

$$R_{opt} = \gamma(np - n_{int}^2) \tag{2.48}$$

$$\gamma = \frac{4\pi q \mu_R}{\epsilon} \tag{2.49}$$

where n_{int} is the intrinsic carrier density, μ_R is an effective recombination mobility, taken to be the larger of the electron and hole mobilities in the material, and ϵ is the dielectric constant of the material [28]. Since departures from equilibrium are large over most of the device, Equation 2.48 is often written as:

$$R_{opt} = \gamma\,(np) \tag{2.50}$$

Although the Langevin optical recombination process is frequently cited and used in all device models e.g. [29], an alternative electron-hole capture mechanism has been suggested recently [30] which is more accurate at high fields.

For an organic semiconductor, the electrons and holes form tightly bound excitons which can diffuse a significant distance before radiative emission. Thus the Langevin recombination rate is treated as the exciton formation rate. More will be said about excitons in the efficiency section of this chapter, and the optical modelling chapters.

2.3.4 Traps

A trap level (an energy level within the bandgap) can behave as a recombination centre, electron trap, or hole trap. As their names suggest electron and hole traps act to remove carriers from the conduction and valence bands. A recombination centre can trap electrons and holes with roughly equal probability and so acts to remove electron-hole pairs from the system [16].

The key to a trap level's behaviour is its energy level [31]. Energy levels close to the LUMO level act as electron traps and energy levels close to the HOMO level act as hole traps. Energy levels at the mid-gap act as recombination centres.

The presence of traps requires extra terms in Poisson's equation and the continuity equations. In Poisson's equation the effect of trapped charge must be included, while in the continuity equations the trap-assisted recombination rate must be accounted for.

Similarly to the electron and hole densities, the trapped electron and hole densities are derived from the Maxwell-Boltzmann distribution;

$$n_{trap} = \frac{N_T}{1 + \exp\left[-\left(q\psi - \phi_n + \chi + E_T\right)/(k_B T)\right]} \tag{2.51}$$

$$p_{trap} = \frac{N_T}{1 + \exp\left[\left(q\psi - \phi_p + \chi_c + E_T\right)/(k_B T)\right]} \tag{2.52}$$

where N_T is the density of trap states and E_T is the energy of the trap level relative to the conduction band.

$$R_{trap} = \frac{np - n_i^2}{\tau_n\left(p + p_1\right) + \tau_p\left(n + n_1\right)} \tag{2.53}$$

where n_1 and p_1 are the equilibrium carrier densities that would result when the Fermi level lies at E_t, and τ_n and τ_p are the electron and hole lifetimes.

2.3.5 Electrode boundary conditions

Carrier injection, through the metal-semiconductor contacts is included in the drift-diffusion model as 6 boundary conditions (3 per electrode) at the edges of the semiconductor (x=0 and x=d).

At each Schottky contact, the electrostatic potential ,ψ_b, is determined from the magnitude of the Schottky barrier. From Figure 2.1;

$$\psi_b(x=0) = -(E_g - \phi_{Bp}) \tag{2.54}$$

$$\psi_b(x=d) = -\phi_{Bn} \tag{2.55}$$

The model also incorporates image force lowering of the barrier at the contacts [31];

$$\psi_{eff} = \psi_b - \Delta\psi_b = \psi_b - \sqrt{\frac{qE}{4\pi\epsilon}} \tag{2.56}$$

provided that the field at the contact has the correct sign for barrier lowering.

There are also 2 current-based boundary conditions at each contact, one for each carrier. The electron and hole current-densities each have two components, the resultant thermionic-emission diffusion currents (see section) and the Fowler-Nordheim tunnelling current (see section)

$$J_n = J_{tedn} + J_{tunn} \tag{2.57}$$

$$J_p = J_{tedp} + J_{tunp} \tag{2.58}$$

The thermionic emission-diffusion currents, J_{tedn} and J_{tedp}, are given by:

$$J_{tedn} = qv_{rn}\left(n - n_{eq}\right) \tag{2.59}$$

$$J_{tedp} = -qv_{rp}\left(p - p_{eq}\right) \tag{2.60}$$

Instead of using the inorganic expression for recombination velocity given in Equation 2.14, v_{rn} and v_{rp} were calculated using the method in [32] which used the assumption that charge recombination at a metal/organic interface is analogous to the Langevin bimolecular recombination rate used in section 2.3.3.

$$v_{rn} = \frac{16\pi\epsilon \left(k_B T\right)^2 \mu_n(\mathrm{E})}{q^3} \tag{2.61}$$

$$v_{rp} = \frac{16\pi\epsilon \left(k_B T\right)^2 \mu_p(\mathrm{E})}{q^3} \tag{2.62}$$

The electron and hole tunnelling currents, J_{tunn} and J_{tunp}, are given by:

$$J_{tn} = \alpha_1 \left(\frac{B}{\phi_{Bn}}\right) \mathrm{E}^2 \exp\left[-\alpha_2 C \left(\frac{(\phi_{Bn})^{3/2}}{\mathrm{E}}\right)\right] \tag{2.63}$$

$$J_{tp} = \alpha_1 \left(\frac{B}{\phi_{Bp}}\right) \mathrm{E}^2 \exp\left[-\alpha_2 C \left(\frac{(\phi_{Bp})^{3/2}}{\mathrm{E}}\right)\right] \tag{2.64}$$

where B and C are given by:

$$B = \frac{q^3}{8\pi h} \tag{2.65}$$

$$C = \frac{8\pi\sqrt{2m}}{3hq} \tag{2.66}$$

α_1 and α_2 are fitting parameters added to the Fowler-Nordheim equations to allow for inaccuracies in their field and temperature dependence (e.g. [24]).

2.3.6 Organic heterojunctions

A common way to improve device efficiency is to use multiple layers of organic semiconductor. The mechanisms involved when a semiconductor comes

into contact with another semiconductor have many similarities to those of metal/semiconductor contact discussed in Section 2.1.

If no interfacial chemical reactions occur then the energy barrier formed at the heterojunction (the interface between two semiconductors with differing HOMO/LUMO energies) is equal to the difference between the material's separate band edge energies. While inorganic semiconductor heterojunctions can display significant band-bending, the rigid band condition applies to organic heterojunctions (for the reasons of low doping/intrinsic carriers discussed above). Figure 2.4 shows the band structure for a bilayer device with offsets at both the HOMO and LUMO levels.

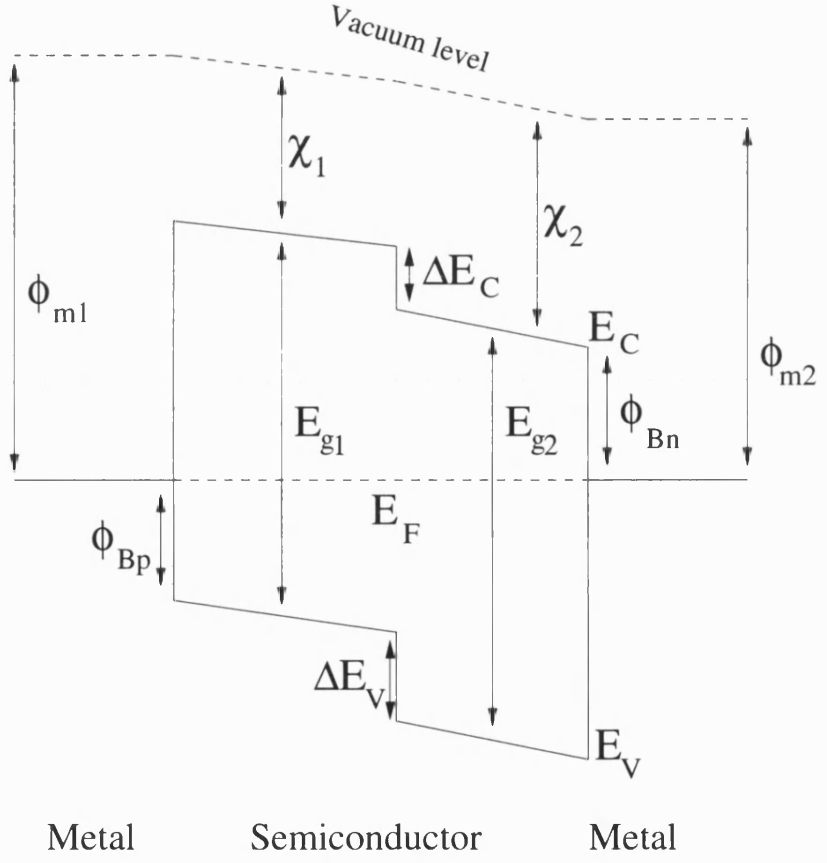

Figure 2.4: Injection/transport via trap energy levels

There are a number of approaches in modelling a heterojunction. of which the simplest is to assume the drift-diffusion equations are continuous across the interface (this is equivalent to stating that the quasi-fermi levels are continuous across interface). The effect of the heterojunction manifests in a discontinuity of carrier densities (see Equations 2.35 and 2.36).

A second approach is to consider the interface as being similar to a Schottky barrier, where the net current across the interface is taken as the difference between two opposing electron or hole currents. For the Schottky contact the resultant current is equal to the difference between $J_{s\rightarrow m}$ and $J_{m\rightarrow s}$ (see Equation 2.8), one of which is fixed and one of which is dependent on the applied bias. For a heterojunction the resultant current is the difference between $J_{s_1\rightarrow s_2}$ and $J_{s_2\rightarrow s_1}$ both of which can vary with the applied bias.

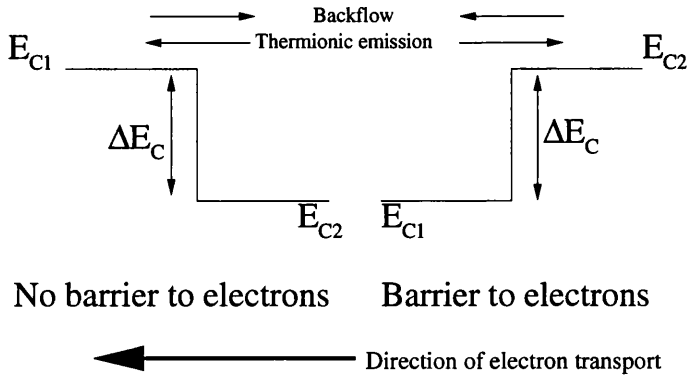

Figure 2.5: Electron transport across a heterojunction

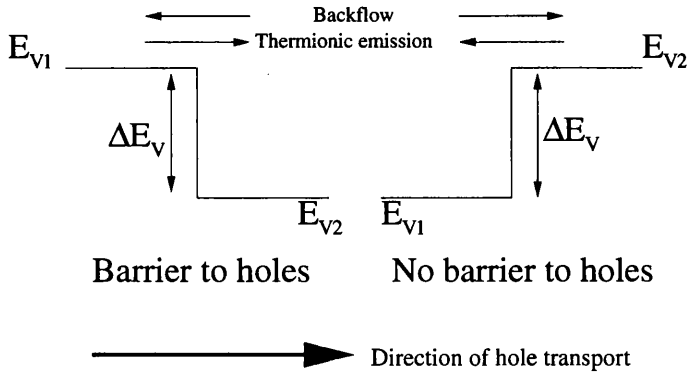

Figure 2.6: Hole transport across a heterojunction

Figures 2.5 and 2.6 shows various band configurations and their effect on a flow of carriers. The equations governing the current through an energy barrier at a heterojunction are given by:

$$J_n = qn_2v_{rn2} - qn_1v_{rn1}\exp\left(\frac{-\Delta E_C}{k_BT}\right) \tag{2.67}$$

$$J_p = qp_1 v_{rp1} - qp_2 v_{rp2} \exp\left(\frac{-\Delta E_V}{k_B T}\right) \tag{2.68}$$

Subscripts of 1 or 2 refer to different semiconductor layers and follow the conventions in Figures 2.5 and 2.6. Electron and hole densities are calculated just to the left or right of the heterojunction, depending on the subscript. The recombination velocities, v_{rn} and v_{rp}, are the same as those given in Equations 2.61 and 2.62. Note that this definition of v_{rn} and v_{rp} comes from the consideration of metal-semiconductor interfaces where image-charge forces are present. These forces are not present at organic-organic interfaces, which means that the actual recombination velocities would be substantially smaller than those used in the simulation.

These equations imply that the quasi-fermi levels can be discontinuous across the heterojunction (unlike the drift-diffusion model). The model assumes an absence of dipoles,sheets of charge and recombination at the interface, which implies continuity of D, ψ, J_n and J_p. In addition tunnelling of carrier across the heterojunction is assumed to be negligible.

2.3.7 Electrical efficiency

Perhaps the key parameter in characterising an OLED is its external quantum efficiency (externally emitted photons per input carrier). While a purely electrical model cannot calculate this quantity, which requires using the optical model discussed in Chapter 5, it can provide a rough estimate (in the fact the upper limit) of a device's efficiency.

The recombination current-density, J_R, which measures the amount of recombination (and hence exciton formation) in the device is given by [5]:

$$J_R = \int_0^d qR(x)\mathrm{dx} = J_n(0) - J_n(L) = J_p(0) - J_p(L) \tag{2.69}$$

Electrons (or holes) injected into the semiconductor at x=0 must either recombine within the layer or leave through the opposite contact. The recombinative

efficiency, η_R is the ratio of the recombination current-density to the total current-density:

$$\eta_R = \frac{J_R}{J_{tot}} \tag{2.70}$$

where $J_{tot} = J_n + J_p$.

Excitons are formed in one of two states; singlet or triplet. According to spin statistics, these are formed in a 1:3 ratio. Ignoring mechanism such as phosphorescence [33], only singlet excitons are capable of radiative decay. Thus the maximum possible external quantum efficiency, η_{eqe} of a device is given by:

$$\eta_{eqe} = \eta_{st}\eta_R \tag{2.71}$$

where η_{st} is the fraction of excitons formed as singlets, which from the above paragraph is equal to 1/4.

2.4 Conclusions

A number of methods of modelling charge injection and transport in a metal/semiconductor/metal structure were presented in this section. The analytic expressions in Section 2.2.5 can be useful in certain situations, however there are limitations in the level of detail they can supply. Additionally they require a number of assumptions to be made about a device, which if untrue may invalidate the results.

The drift-diffusion model with Schottky boundary conditions allows a detailed spatial study of device characteristics, and does not require classification of the device as injection- or space-charge limited before analysis and fitting can begin. Due to the complex, non-linear nature of the drift-diffusion equations, numerical solution techniques, discussed in the next chapter, must be used.

References

[1] S. M. Sze, *Physics of Semiconductor Devices*, 2^{nd} ed., J. Wiley and Sons, New York (1981).

[2] G. G. Malliaras and J. C. Scott, "Numerical simulations of the electrical characteristics and the efficiencies of single-layer organic light emitting diodes", *J. Appl. Phys.*, **85**, 7426 (1999).

[3] J. M. Lupton and I. D. W. Samuel, "Temperature-dependent single carrier device model for polymeric light emitting diodes", *J. Phys. D.:Appl. Phys.*, **32**, 2973 (1999).

[4] D. J. Pinner, R. H. Friend, and N. Tessler, "Transient electroluminescence of polymer light emitting diodes using electrical pulses", *J. Appl. Phys.*, **86**, 5116 (1999).

[5] B. K. Crone, P. S. Davids, I. H. Campbell, and D. L. Smith, "Device model investigation of bilayer organic light emitting diodes", *J. Appl. Phys.* , **87**, 1974 (2000).

[6] B. Ruhstaller, S. A. Carter, S. Barth, H. Riel, W. Riess and J. C. Scott, "Transient and steady-state behavior of space charges in multilayer organic light-emitting diodes", *J. Appl. Phys.*, **89**, 4575 (2001).

[7] J. C. Scott, P. J. Brock, J. R. Salem, S. Ramos, G. G. Malliaras, S. A. Carter, and L. Bozano, "Charge transport processes in organic light-emitting devices", *Synth. Met.*, **111-112**, 289 (2000).

[8] T. M. Brown, J. S. Kim, R. H. Friend, F. Cacialli, R. Daik, and W. J. Feast, "Built-in field electroabsorption spectroscopy of polymer light-emitting diodes incorporating a doped poly(3,4-ethylene dioxythiophene) hole injection layer", *Appl. Phys. Lett.*, **75**, 1679 (1999).

[9] R. U. A. Khan, *Private Communication* (2002-2003).

[10] H. K. Hensich, *Semiconductor Contacts*, Clarendon Press, Oxford (1989).

[11] K. C. Kao, and W.Hwang, *Electrical Transport In Solids: with particular reference to organic semiconductors*, Pergamon Press, Oxford (1981).

[12] R. H. Fowler and L. Nordheim, "Electron emission in intense electric fields", *Proc. Roy. Soc. London A*, **119**, 173 (1928).

[13] C. D. J. Blades, *Ph.D. Thesis*, University of Bath (2000).

[14] J. G. Simmons, "Richardson-Schottky Effect in Solids", *Phys. Rev. Lett.*, **15**, 967 (1965).

[15] R. U. A. Khan, T. Kreouzis, D. Poplavskyy and D. D. C. Bradley, "Hole injection and transport in a fluorene-containing copolymer" *Preprint* (2003).

[16] M. A. Lampert and P. Mark, *Current Injection In Solids*, Academic Press, London (1970).

[17] P. N. Murgatroyd, " Dimensional considerations for space-charge conduction in solids", *J. Phys. D: Appl. Phys.*, **3**, 151 (1970).

[18] R. H. Parmenter and W. Ruppel, *J. Appl. Phys.*, **30**, 1548 (1959).

[19] P. W. M. Blom, H. C. F. Martens, and J. N. Huiberts, "Charge transport in polymer light-emitting diodes", *Synthetic Metals*, **121**, 1621 (2001).

[20] L. Bozano, S. A. Carter, J. C. Scott, G. G. Malliaras, and P. J. Brock, "Temperature- and field-dependent electron and hole mobilities in polymer light-emitting diodes", *Appl. Phys. Lett.*, **74**, 1132 (1999).

[21] W. Brütting, S. Berleb, and A. G. Mückl, "Device physics of organic light-emitting diodes based on molecular materials", *Organic Electronics*, **2**, 1 (2001).

[22] A. J. Campbell, D. D. C. Bradley, J. Laubender, and M. Sokolowski, "Thermally activated injection limited conduction in single layer N,N '-diphenyl-N,N '-bis(3-methylphenyl)1-1 '-biphenyl-4,4 '-diamine light emitting diodes", *J. Appl. Phys.*, **86**, 5004 (1999).

[23] T. Aernouts, W. Geens, J. Poortmans, J. Nijs, and R. Mertens, "Analysis and simulation of the IV-characteristics of PPV-oligomer based Schottky diodes", *Synthetic Metals*, **122**, 153 (2001).

[24] A. J. Campbell, D. D. C. Bradley, and D. G. Lidzey, "Space-charge limited conduction with traps in poly(phenylene vinylene) light emitting diodes", *J. Appl. Phys.*, **82**, 6326 (1997).

[25] D. Schroeder, *Modelling of Interface Carrier Transport for Device Simulation*, Springer-Verlag, Vienna (1994).

[26] C. M. Snowden, *Semiconductor Device Modelling*, Peregrinus, London (1988).

[27] M. N. O. Sadiku, *Elements of Electromagnetics*, second edition, Oxford University Press, Oxford (1995).

[28] M. Pope and C. E. Swenburg *Electronic Processes in Organic Crystals* (Oxford University Press, Oxford, 1982).

[29] P. S. Davids, I. H. Campbell, and D. L. Smith, "Device model for single carrier organic diodes", *J. Appl. Phys.*, **82**, 6319 (1997).

[30] J. A. Barker, C. L. Foden, and N. C. Greenham, *European Conf. On Molecular Electronics*, Presented paper available from www.cdtltd.co.uk (2002).

[31] M. S. Tyagi, *Introduction to Semiconductor Materials and Devices*, J. Wiley and Sons, New York (1991).

[32] J. C. Scott and G. G. Malliaras, "Charge injection and recombination at the metal-organic interface", *Chem. Phys. Lett.*, **299**, 115 (1999).

[33] R. H. Friend, R. W. Gymer, A. B. Holmes, J. H. Burroughes, R. N. Marks, C. Taliani, D. D. C. Bradley, D. A. Dos Santos, J. L Brédas, M. Löglund, and W. R. Salaneck, "Electroluminescence in conjugated polymers", *Nature*, **397**, 121 (1999).

Chapter 3

Numerical solution of differential equations

The equations governing the behaviour of an OLED were detailed in the previous section. This chapter details how differential equations are solved via numerical techniques and how a technique can be modified to improve its performance.

The simulation uses a modified version of the Solvde functions from [1]. Solvde belongs to the class of relaxation methods, which in brief are methods that use approximate solutions to a problem to calculate a more accurate solution. This process can be repeated an arbitrary number of times, producing successively more accurate solutions, although machine precision places an upper limit on the accuracy that can be achieved. Figure 3.1 shows a qualitative representation of the relaxation method.

The following describes the key operations used by Solvde [1] to solve a set of differential equations. Beginning with N dependent variables $\mathbf{Y}$, and their corresponding differential equations $\mathbf{F}$, defined between two boundary values of a dependent variable x:

$$\frac{dy_i}{dx} = f_i(x, \mathbf{Y}) \qquad\qquad i = 1...N \qquad\qquad (3.1)$$

where y_i is the ith member of $\mathbf{Y}$, and f_i is the ith member of $\mathbf{F}$.

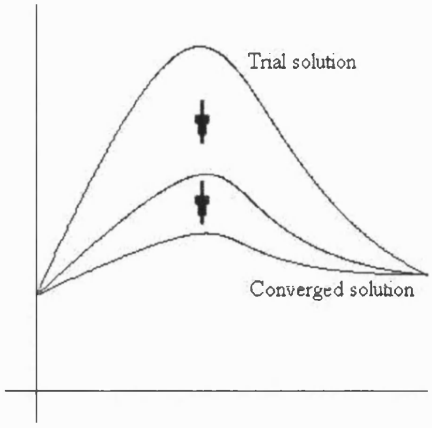

Figure 3.1: Outline of the relaxation method

The above differential equations are converted into finite-difference equations by being discretised on a mesh with M points. At mesh-point k, x and $\mathbf{Y}$ have values x_k and $\mathbf{Y_k}$. Using a simple two-point discretisation, Equation 3.1 becomes

$$\frac{y_{k,i} - y_{k-1,i}}{x_k - x_{k-1}} = f_i\left(\frac{1}{2}(x_k - x_{k-1}), \frac{1}{2}(y_{k,i} + y_{k-1,i})\right) \tag{3.2}$$

or

$$(y_{k,i} - y_{k-1,i}) - (x_k - x_{k-1}) f_i\left(\frac{1}{2}(x_k - x_{k-1}), \frac{1}{2}(y_{k,i} + y_{k-1,i})\right) = 0 \tag{3.3}$$

where $y_{k,i}$ is the ith member of $\mathbf{Y}_k$.

The initial and final boundaries are located at x_1 and x_M respectively. The initial boundary has n_1 boundary conditions relating to it, while n_2 boundary conditions relate to the final boundary. For the system to have a unique solution the sum of n_1 and n_2 must be greater than or equal to N. The boundary conditions are defined by two sets of functions $\mathbf{B}_{initial}$ and $\mathbf{B}_{final}$. The above information allows the definition of a set of M+1 difference equations, expressed as a function of $\mathbf{Y}$, $\mathbf{E(Y)}$:

At the initial boundary

$$e_{1,i}(\mathbf{Y}_1) = b_{initial,i}(x_1, \mathbf{Y}_1) \tag{3.4}$$

where i=1...n_1

At the final boundary

$$e_{M+1,i}(\mathbf{Y}_M) = b_{final,i}(x_M, \mathbf{Y}_M) \tag{3.5}$$

where i=n_2...N

At points k=2...M

$$e_{k,i}(\mathbf{Y}_k) = (y_{k,i} - y_{k-1,i}) - (x_k - x_{k-1}) f_i \left(\frac{1}{2}(x_k - x_{k-1}), \frac{1}{2}(y_{k,i} + y_{k-1,i}) \right) \tag{3.6}$$

where i=1...N

$e_{k,i}$ is the ith member of $\mathbf{E}$ at mesh point k. Similarly $b_{initial,i}$ and $b_{final,i}$ are the ith members of $\mathbf{B}_{initial}$ and $\mathbf{B}_{final}$.

Taking a trial solution for $\mathbf{Y}$, it is possible to calculate a set of corrections $\Delta\mathbf{Y}$ by expanding Equations 3.4-3.6 by means of a first-order Taylor expansion:

$$e_{1,i}(\mathbf{Y}_1 + \Delta\mathbf{Y}_1) \approx e_{1,i}(\mathbf{Y}_1) + \sum_{n=1}^{N} \frac{\partial e_{1,i}}{\partial y_{1,n}} \Delta y_{1,n} \tag{3.7}$$

where i=1...n_1

$$e_{M+1,i}(\mathbf{Y}_M + \Delta\mathbf{Y}_M) \approx e_{M+1,i}(\mathbf{Y}_M) + \sum_{n=1}^{N} \frac{\partial e_{M+1,i}}{\partial y_{M,n}} \Delta y_{M,n} \tag{3.8}$$

where i=n_2...N

$$e_{k,i}(\mathbf{Y}_k + \Delta\mathbf{Y}_k, \mathbf{Y}_{k-1} + \Delta\mathbf{Y}_{k-1}) \approx e_{k,i}(\mathbf{Y}_k, \mathbf{Y}_{k-1}) + \sum_{n=1}^{N} \frac{\partial e_{k,i}}{\partial y_{k,n}} \Delta y_{k,n} + \sum_{n=1}^{N} \frac{\partial e_{k,i}}{\partial y_{k-1,n}} \Delta y_{k-1,n} \tag{3.9}$$

where i=1...N

A solution to Equations 3.4-3.6 has been found when $\mathbf{E}(\mathbf{Y}+\Delta\mathbf{Y})$ is equal to zero. This allows Equations 3.7-3.9 to be rewritten as:

$$\sum_{n=1}^{N} s_{i,n}\Delta y_{1,n} = -e_{1,i} \tag{3.10}$$

where i=1...n_1

$$\sum_{n=1}^{N} s_{i,n}\Delta y_{M,n} = -e_{M+1,i} \tag{3.11}$$

where i=n_2...N

$$\sum_{n=1}^{N} s_{i,n}\Delta y_{k-1,n} + \sum_{n=N+1}^{2N} s_{i,n}\Delta Y_{k,n} = -e_{k,i} \tag{3.12}$$

where i=1...N

Where $\mathbf{S}$ is a matrix of partial derivatives at a mesh point k:

$$s_{i,n} = \frac{\partial E_{k,i}}{\partial y_{k-1,n}} \tag{3.13}$$

where i=1...N

$$s_{i,n} = \frac{\partial E_{k,i}}{\partial y_{k-1,n-N}} \tag{3.14}$$

where i=N+1..2.N

Sets of linear equations (such as Equations 3.7-3.9) are commonly solved via matrix techniques. The equations are converted into a matrix equation of the form $\mathbf{A}.\mathbf{x}=\mathbf{b}$. Where $\mathbf{A}$ and $\mathbf{b}$ are defined by the set of equations, $\mathbf{x}$ is an unknown solution vector. In the notation from [1] this is written as $\mathbf{S}.\mathbf{Y}=\mathbf{E}$. Table 3.1 shows the matrix structure formed from Equations 3.10-3.12 for a system with 6 dependent variables, 3 mesh points and 3 boundary conditions at each boundary (this is equivalent to the system formed by discretising the drift-diffusion equations).

SSSSSS			ΔY	E
SSSSSS			ΔY	E
SSSSSS			ΔY	E
SSSSSS	SSSSSS		ΔY	E
SSSSSS	SSSSSS		ΔY	E
SSSSSS	SSSSSS		ΔY	E
SSSSSS	SSSSSS		ΔY	E
SSSSSS	SSSSSS		ΔY	E
SSSSSS	SSSSSS		ΔY	E
	SSSSSS	SSSSSS	ΔY	E
	SSSSSS	SSSSSS	ΔY	E
	SSSSSS	SSSSSS	ΔY	E
	SSSSSS	SSSSSS	ΔY	E
	SSSSSS	SSSSSS	ΔY	E
	SSSSSS	SSSSSS	ΔY	E
		SSSSSS	ΔY	E
		SSSSSS	ΔY	E
		SSSSSS	ΔY	E

Table 3.1: Matrix structure formed by $\mathbf{S}$ $\Delta\mathbf{Y}$ and $\mathbf{E}$ [1]
S Element of $\mathbf{S}$
ΔY Element of $\Delta\mathbf{Y}$
E Element of $\mathbf{E}$

Perhaps the most obvious way of solving for $\Delta\mathbf{Y}$ is to multiply both sides by $\mathbf{S}^{-1}$, which then gives $\Delta\mathbf{Y}$ as $\mathbf{S}^{-1}.\mathbf{E}$. However matrix inversion is a computationally inefficient process and when dealing with large matrices it is preferable to use more sophisticated techniques. Solvde uses Gaussian elimination [1] to reduce the matrix to an upper triangular form (see Table 3.2). The components of $\Delta\mathbf{Y}$ can then be calculated via backsubstitution.

It is worth noting that the updated solution $\mathbf{Y}+\Delta\mathbf{Y}$ is not necessarily the precise solution to Equations 3.4-3.6. The above process can be iterated using the updated solution to produce an updated $\mathbf{S}$ and $\mathbf{E}$ and so calculate another $\Delta\mathbf{Y}$.

$\Delta\mathbf{Y}$ can be used as an error estimate for the solution. It is assumed that the magnitude of $\Delta Y_{k,i}$ is roughly equal to the absolute error in $Y_{k,i}$. An error average can be calculated over the whole of the mesh as

$$E = \frac{1}{MN} \sum_{k=1}^{M} \sum_{i=1}^{N} \frac{\Delta Y_{k,i}}{Y_{typical,i}} \tag{3.15}$$

1			S	S																	ΔY	E
	1		S	S																	ΔY	E
		1	S	S																	ΔY	E
			1						S	S											ΔY	E
				1					S	S											ΔY	E
					1				S	S											ΔY	E
						1			S	S											ΔY	E
							1		S	S											ΔY	E
								1	S	S											ΔY	E
									1								S	S			ΔY	E
										1							S	S			ΔY	E
											1						S	S			ΔY	E
												1					S	S			ΔY	E
													1				S	S			ΔY	E
														1			S	S			ΔY	E
															1		S	S			ΔY	E
																	1				ΔY	E
																		1			ΔY	E
																			1		ΔY	E

Table 3.2: Matrix structure formed after Solvdes Gaussian elimination step [1]

where $Y_{typical,i}$ is a typical value of the variable $Y_{k,i}$.

3.1 Internal Boundary Conditions

It is possible to modify Solvde to include internal boundary conditions - mesh points where some (or all) of the elements of Equation 3.1 are replaced. With reference to the drift-diffusion theory in the previous chapter, the thermionic-emission heterojunction model acts as an internal boundary condition.

In this case the heterojunction is implemented by replacing the drift-diffusion equations (at either side of the heterojunction) with the thermionic emission equations. Poisson's equation and the continuity equation are continuous across the heterojunction. The relevant blocks of the S and Y matrices are calculated consistently with these changes. The system is then solved as normal via Gaussian elimination - although the S matrix has been calculated in a slightly different fashion it makes no difference to the matrix solver.

3.2 Numerical Instability

During the initial phases of programming the drift-diffusion simulation, the performance of various numerical differential-equation solvers were investigated [2]. For simulating relatively simple single-layer, uni- and bi-polar devices it was found that the Solvde package from [1] was the optimum solution method for the following reasons:

1) Data storage requirements were reasonably modest

2) Simulation runtime scaled efficiently with increasing mesh-size

3) The code was both platform-independent and public domain.

However as more physical effects (such as trapping) were included in the model and as more complex multilayered devices were simulated, problems began to occur with the program. For specific, apparently unrelated, parameter sets the program would only be able to produce convergent solutions up to a certain bias. Attempts to increase the bias further caused a rapidly divergent solution, which would eventually result in a fatal program error. This seriously hindered the investigation of virtually all multi-layered devices, and a high priority was given to improving the simulations stability.

An initial diagnosis was that the numerical instabilities were due to a failure of the Solvde matrix-solution algorithms. To test this, Solvde's Gaussian elimination solver was replaced with a number of alternative matrix solvers (among them routines from the NAG software library [3] and simulations carried out on systems known to be problematic. Disappointingly none of the replacement solvers greatly increased the program's stability. Additionally, virtually all the replacement functions substantially decreased the simulation's speed, sometimes by as much as an order of magnitude. Since none of the replacement algorithms offered significant advantages over Solvde's own algorithm, it was concluded that the numerical instabilities were not due to the Gaussian elimination solver.

For systems known to exhibit instability, the F04arf NAG routine would often report an error message that **S** was approximately singular. This suggested that it might be the matrices themselves that were the problem. After analysis of the

structure of **S** and the output of the various solvers, it was concluded that the numerical instabilities were caused by the data-matrix being ill-conditioned. A matrix **S** is said to be ill-conditioned if a relatively small change in one (or more) of the matrix co-efficients results in a relatively large change in the solution [4]. Since a computer can only represent a number to a finite precision, the calculation of a mathematical operation may be subject to error. In the simulation there are two main stages where error can arise

1) The calculation of the matrix co-efficients

2) Reduction of the matrix to a solvable form

For an ill-conditioned matrix, small numerical errors arising from these operations can cause significant error in the solution.

As an example consider

$$\begin{bmatrix} 1 & -1.9999 \\ 1 & -1.9998 \end{bmatrix} \begin{pmatrix} A \\ B \end{pmatrix} = \begin{pmatrix} 0 \\ 1 \end{pmatrix} \tag{3.16}$$

which has the solution A=19999,B=10^4.

if a small perturbation is applied to a single element of the above matrix

$$\begin{bmatrix} 1 & -1.9999 \\ 1 & -1.9997 \end{bmatrix} \begin{pmatrix} A \\ B \end{pmatrix} = \begin{pmatrix} 0 \\ 1 \end{pmatrix} \tag{3.17}$$

it can cause a considerable change in the solution (A=9999.5,B=5^3).

The origin of this behaviour is due to magnitude of the matrix determinant. Because its magnitude is relatively small (0.0001) compared to the matrix elements, a small change in one of the elements can can significantly alter the solution. This is analogous to

$$y = \frac{b}{a} \tag{3.18}$$

where a is equivalent to a small determinant. A small change in a can cause a disproportionately large change in y.

As mentioned above substitution of the NAG functions for Solvde did not greatly decrease the simulation's numerical instability. However enabling the preconditioning options in the F11def NAG routine produced slight improvements in program performance. This raised the question: could preconditioning the data-

matrix solve the problem of simulation instability?

3.3 Preconditioning

Fundamentally the drift-diffusion simulation is a matrix solver, solving the problem

$$\mathbf{S}.\mathbf{Y} = \mathbf{E} \tag{3.19}$$

for known $\mathbf{S}$ and $\mathbf{E}$. Unfortunately, in our case $\mathbf{S}$ is what is known as ill-conditioned and can cause numerical instability in the matrix solver. A preconditioner is a matrix $\mathbf{P}$ designed to improve the numerical properties of problems like Equation 3.19

$$\mathbf{P}^{-1}.\mathbf{S}.\mathbf{Y} = \mathbf{P}^{-1}.\mathbf{E} \tag{3.20}$$

or

$$(\mathbf{A}.\mathbf{P}^{-1}).(\mathbf{P}.\mathbf{x}) = \mathbf{b} \tag{3.21}$$

The technique of matrix preconditioning is used in many scientific fields (e.g. [5, 6, 7, 8] and has been used in other electrical transport models [e.g. [9, 10]]). The choice of $\mathbf{P}$ is crucial: a poor preconditioner might actually make the system harder to solve. Some preconditioners are constructed by taking an approximation to $\mathbf{S}$. For example in the case of a diagonally-dominant matrix, applying the preconditioner

$$\mathbf{P}_{j,k} = \mathbf{S}_{j,k}\delta_{j,k} \tag{3.22}$$

can be extremely effective [11] since

$$(\mathbf{S}.\mathbf{P}^{-1}) \approx \mathbf{I} \tag{3.23}$$

and so Equation 3.25 becomes

$$\mathbf{I}.\mathbf{Y} = \mathbf{P}^{-1}.\mathbf{E} \tag{3.24}$$

making the calculation of $\mathbf{Y}$ trivial.

The simulation currently uses what is essentially a two-stage preconditioner, set-

up as follows:

$$\mathbf{P}_{scl}^{-1}.\mathbf{P}_{str}^{-1}.\mathbf{A}.\mathbf{x} = \mathbf{P}_{scl}^{-1}.\mathbf{P}_{str}^{-1}.\mathbf{b} \tag{3.25}$$

where $\mathbf{P}_{str}$ is designed to optimize the structure of $\mathbf{S}$ for Gaussian-elimination and $\mathbf{P}_{scl}$ optimizes the numerical properties of $\mathbf{S}$. Because of $\mathbf{S}$'s block structure it is not necessary to explicitly construct $\mathbf{P}_{str}$ or $\mathbf{P}_{scl}$, instead the pertinent elements of $\mathbf{P}_{str}$ or $\mathbf{P}_{scl}$ needed to precondition a block of $\mathbf{S}$ can be calculated from that block alone. $\mathbf{P}_{str}$ and $\mathbf{P}_{scl}$ were selected by empirically testing the simulation with different preconditioners.

All this means that it is possible to precondition $\mathbf{S}$ with minimal computational demands. The run-time increase of the simulation is negligible, especially when compared with the stability improvement.

As a brief example of how scaling can improve a mathematical calculation, consider Equation 3.18. For the purposes of demonstration the error in b and A, introduced when calculating y, is taken as 1% of b. So for b=1,a=0.02 Equation 3.18 becomes

$$y = \frac{1 \pm 0.01}{0.02 \pm 0.01} \tag{3.26}$$

which gives a range of y values from 33 to 101.

If a is now preconditioned with a multiplication by 10, Equation 3.26 becomes

$$y = 10\frac{1 \pm 0.01}{(0.2) \pm 0.01} \tag{3.27}$$

which gives a range of y values of 4.93 to 5.07

The effect of scaling on the drift-diffusion simulation is shown in Figure 3.2. Benchmarks of Solvde's error estimate against iteration count are shown for no preconditioner, and for $\mathbf{P}_{scl}$ and one of the other scaling matrices used in the testing process. The results are for solution of the 0V case for a bilayer device similar to the one in Section 6.2, with a convergent solution defined as one with an error of less than $1x10^{-6}$. The only difference between the three simulations is the preconditioning of the data matrix. The unconditioned simulation took the longest to converge to a solution, with the preconditioners noticeably reducing the iteration count. While $\mathbf{P}_{scl}$'s rate of convergence is initially slower than the

other scaling matrix, increases in the rate result in a converged solution roughly 50 iterations sooner.

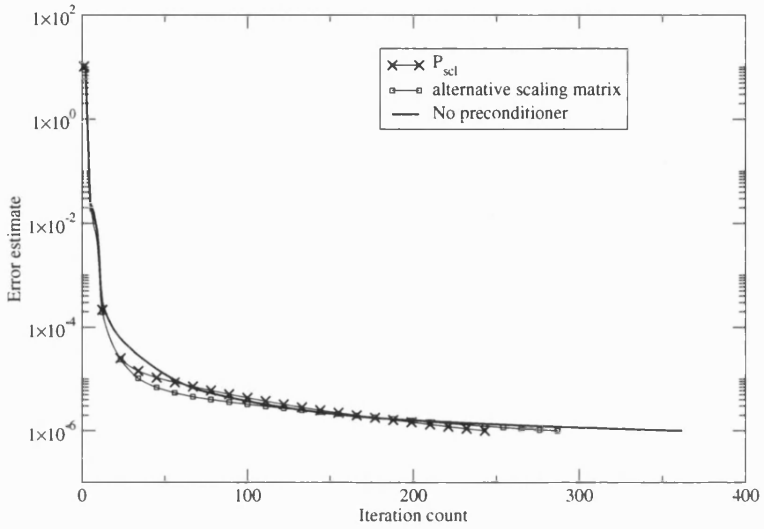

Figure 3.2: Error estimate against interation count for using the simulation with and without preconditioning

While a speed improvement is beneficial, the primary advantage of preconditioning is shown in Figure 3.3. The simulation is trying to solve the same system as in 3.2, but this time for an applied bias of 2.34V. At this applied bias the unconditioned system is unable to produce a converged system, which eventually causes the simulation to crash. A convergent solution is produced by using the preconditioners, and the system could be simulated for applied biases of a least 10V.

3.4 Conclusion

The differential equations from section 2.3 are solved via an iterative relaxation method, based on a finite-difference approximation. This method is fast, and has relatively low resource requirements. However the inherent ill-conditioning of matrices formed from the differential equations makes the simulation prone to numerical instability. Changing the method used to solve these matrices does not

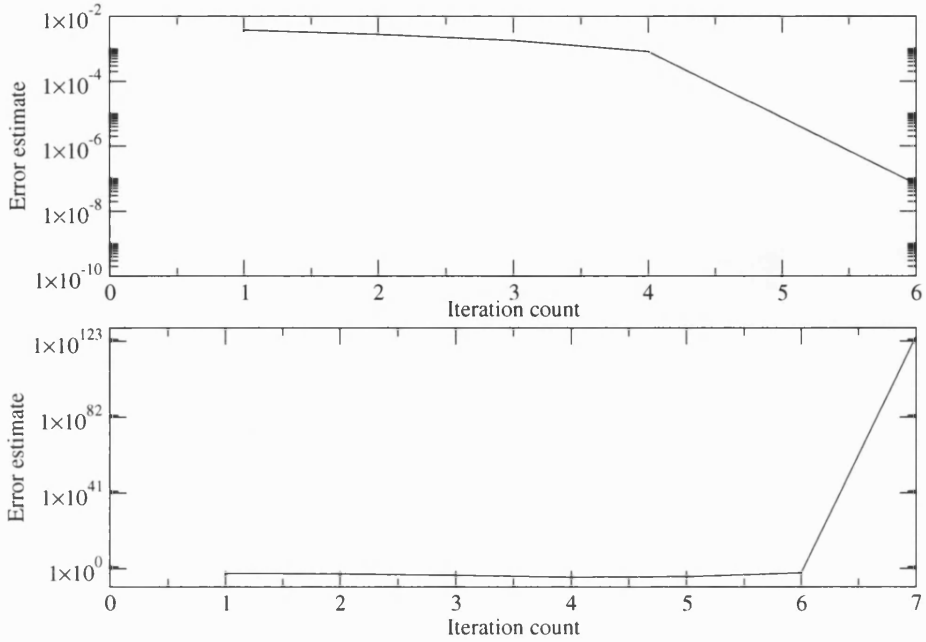

Figure 3.3: Error estimate against interation count for using the simulation with (top) and without (bottom) preconditioning

remove this problem, however it was found that the technique of matrix preconditioning could produce noticeable improvements to the simulation's stability.

References

[1] W. H. Press, S. A Teukolsky, W. T. Vetterling and B. P Flannery, *Numerical recipes in C second edition*, Cambridge University Press, Cambridge (1992)

[2] C. D. J. Blades, *Ph.D. Thesis*, University of Bath (2000).

[3] NAG Fortran Library,*http://www.nag.co.uk/*, (2003)

[4] I. S. Duff, *Matrix methods*, Plenum publishing corporation (1998)

[5] H. Deng and H. Ling, "An efficient wavelet preconditioner for iterative solution of three-dimensional electromagnetic integral equations", *IEEE Trans. on. Ant. and Prop.* **51** , 654-660 (2003)

[6] I. Stranden, S. Tsuruta and I. Misztal, "Simple preconditioners for the conjugate gradient method: experience with test day models " , *J. of Ani. Breed. and Gen.* **119** , 166-174 (2002)

[7] L. Chen , W. Eberly, E. Kaltofen, B. D. Saunders, W. J. Turner and G. Villard , "Efficient matrix preconditioners for black box linear algebra", *Lin. Alg. and it's Appl.*, **343** , 119-146 (2002)

[8] Y. Saad, "Finding exact and approximate block structures for ILU preconditioning " , *Siam J. on Sci. Comp.* , **24** , 1107-1123 (2003)

[9] T. Simlinger, H. Brech, T. Grave and S. Selberherr, "Simulation of submicron double-heterojunction high electron mobility transistors with MINIMOS-NT" ,*IEEE Trans. on. Elec. Dev.*, **44**, 700-707 (1997)

[10] G. Speyer, D. Vasileska and S. M. Goodnick, "Efficient Poisson Equation Solvers for Large Scale 3D Simulations" , *Model. and Sim. of Micro. 2001*, 22-26 (2001)

[11] R. Barrett, M. Berry, T. F. Chan, J. Demmel, J. M. Donato, J. Dongarra, V. Eijkhout, R. Pozo, C. Romine and H. Van der Vorst, *Templates for the Solution of Linear Systems: Building Blocks for Iterative Methods 1*, SIAM, Internet publication (1994).

Chapter 4

Electrical Device Simulation

4.1 Electrical Modelling

In order to extend the electrical model, previously validated by [1] and [2], the focus of work has shifted away from single-layer devices constructed from conventional materials (such as PPV) and bi-layer devices to more novel or complex devices and materials.

The work contained within this chapter details work on single-layer devices constructed of a novel blue-emitting copolymer and emissive shift in a tri-layer OLED. Additionally the differences between two different heterojunction models are studied in a theoretical bi-layer device.

4.2 Modelling heterojunctions in an OLED

There are two main factors that limit the photometric efficiency of an OLED; Mismatches between electron and hole transport can result in recombination at metal contacts or other optically inefficient regions within the device (see chapters 5 and 6). Additionally, charge imbalance due to unbalanced carrier injection limits the recombinative efficiency since the majority carriers can be transported straight through the device instead of recombining.

One method of increasing device efficiency is to construct the diode from multiple layers of organic semiconductor. In many multi-layered OLEDs layers can be characterised as electron-transporting layers (ETL), hole-transporting layers (HTL) or emitting layers (EL). Often a transporting layer will also act as an emitting layer. The choice of materials is based on a number of factors. Differences in HOMO and LUMO energies between layers can increase charge injection (by reducing the Schottky barrier height) and additionally can increase recombinative efficiency (by confining carriers to specific regions in the device). Differences in electron and hole mobilities also contribute to improvements in injection/recombination.

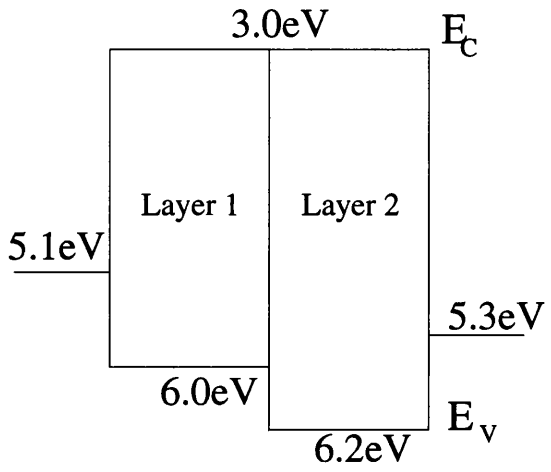

Figure 4.1: Band structure for the first device

The previous chapter (Section 2.3.6) presented two methods to model an organic heterojunction (the interface between two organic semiconductors with different HOMO or LUMO energies). In this section two artificial hole-dominated bilayer OLEDs, inspired by the similar devices in [3], are studied. The devices both have a discontinuity in the valence band (the conduction band is continuous between the layers). Each device was simulated using both methods of heterojunction modelling-firstly by assuming continuity of drift diffusion across the interface and secondly by explicitly including thermionic emission effects.

The first device (shown in Figure 4.1) has a relatively small discontinuity between the HOMO levels (0.2 eV). The direction of forward bias is taken with the anode as the left contact and the cathode as the right. Reverse bias swaps these roles, with the left contact acting as the cathode and the right as the anode. Unless stated otherwise, all other device band diagrams in this thesis conform to this

classification.

Parameter	Layer 1	Layer 2
χ_c (eV)	3.0	3.0
E_g (eV)	3.0	3.2
ϵ_s	3.0	3.0
N_C (m^{-3})	1×10^{27}	1×10^{27}
N_V (m^{-3})	1×10^{27}	1×10^{27}
N_{dop} (m^{-3})	-1×10^{15}	-1×10^{15}
μ_n (m^2/Vs)	5×10^{-8}	5×10^{-8}
μ_p (m^2/Vs)	5×10^{-8}	5×10^{-8}
E_0 (Vm^{-1})	2.0×10^{4}	2.0×10^{4}
Thickness (m)	1.0×10^{-6}	1.0×10^{-6}

Table 4.1: Material parameters

Figure 4.2 shows the forward bias J-V curves for the first device, simulated using the parameters listed in Table 4.1. When the thermionic emission heterojunction boundary conditions are included in the simulation, the current-density is slightly reduced in magnitude, compared to the "plain" drift-diffusion simulation. This is expected as by including the effect of the 0.2eV energy barrier, hole transport through the heterojunction is reduced.

Looking at Figure 4.1, for reverse bias there is no energetic barrier to hole transport across the heterojunction. This means that including thermionic emission effects in the simulation should not noticeably alter the device's transport properties, and this is verified in Figure 4.3 (the absolute magnitude of the current-density is shown) as there is no discernable difference between the J-V curves.

To study the effect of a much larger offset between HOMO levels, the energy gap of the right layer in Figure 4.1 was increased by 2.0eV, resulting in a 2.2eV barrier to hole injection (Figure 4.4). The other device parameters retained the values given in Table 4.1.

Figure 4.5 shows the forward bias J-V curves for the second device. Even though the hole injection barrier is unchanged (ϕ_{Bp} is 0.9 eV) the large discontinuity between the organic HOMO levels causes the current-density to be drastically reduced. As before, including the effect of thermionic-emission at the heterojunction causes a decrease in the simulated current.

Figure 4.5 shows the electric field and hole density profiles through the device.

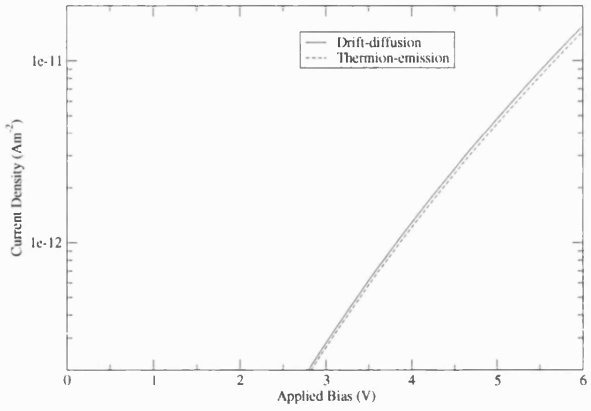

Figure 4.2: Forward bias J-V curves for the first device

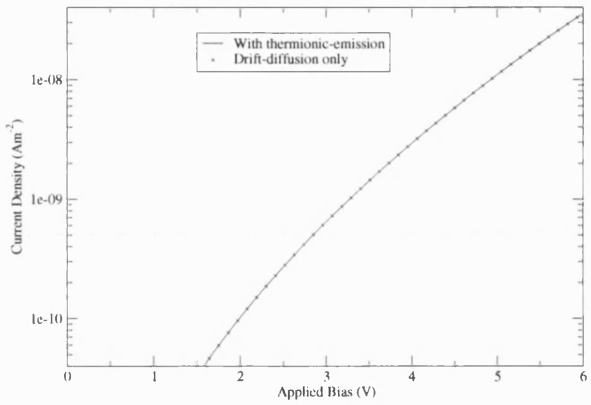

Figure 4.3: Reverse bias J-V curves for the first device

Note that the hole profile has a linearly scaled vertical axis to highlight the peak density, which is the significant quantity for these results.The simulated field in the right layer is increased when thermionic effects are included. This is due to the thermionic-emission boundary conditions causing an increase in the hole density at the heterojunction.

In general, including the thermionic-emission heterojunction boundary conditions in the device model will (compared to the "plain" drift-diffusion model) cause a drop in the current-density due to an increased build up of carriers at the interface. This build up of holes (or electrons) can also result in an increased

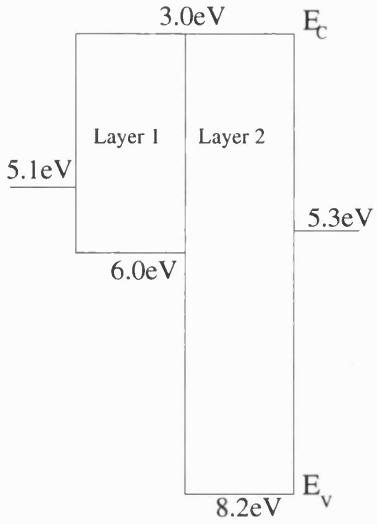

Figure 4.4: Band structure for the second device

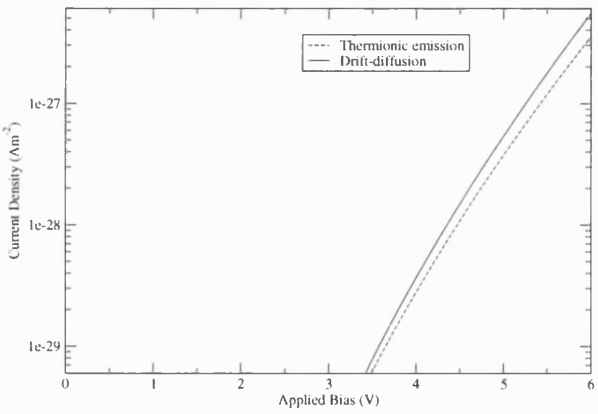

Figure 4.5: Forward bias J-V curves for the second device

(or decreased) electric field within a layer. Although this difference in current-density/electric field does increase with the magnitude of the HOMO discontinuity, it increases far less than might be expected from the exponential nature of the heterojunction boundary conditions (see Section 2.3.6). This is presumably due to the fact that the magnitude of the thermionic emission current increases as the system deviates from its equilibrium state [3]. For the second device, although the HOMO offset is 2.0eV larger, the magnitude of the currents are much smaller.

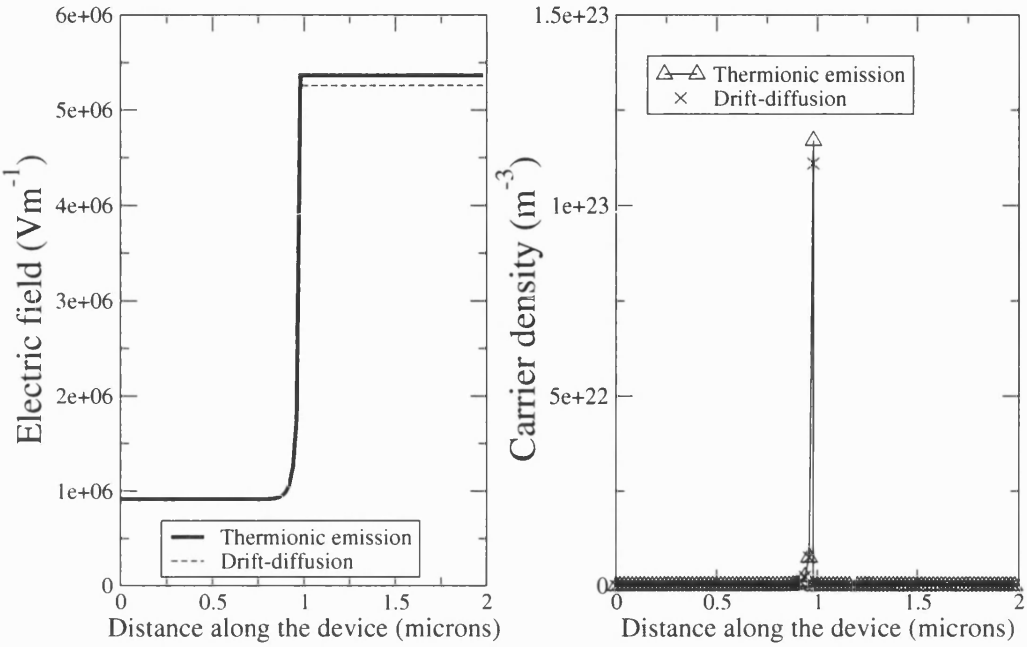

Figure 4.6: Electric field profile (left) and hole density profile (right) for the second device at an applied bias of 6V

4.3 Emissive shift in a tri-layer OLED

This section continues the theme of multi-layered devices with a look at a tri-layer N,N-diphenyl-N,N-bis(3-methylphenyl)1-1-biphenyl-4,4-diamine (TPD)/2-(4-tert-butylphenyl)-5-(4-biphenyl)-1,3,4-oxadiazole (PBD)/ tris-(8- hydroxyquinoline) aluminium (Alq) device, created by [4]. Considerations of the band structure energetics (see Figure 4.7) by [4] led to these materials being nominally classified with TPD as an electron transporter, PBD as an emitting material and Alq as a hole transporter. However, as this section shows, this is an incorrect description of roles the materials play during device operation.

Reference [4] reported measurements of the device's luminescent output at various voltages - Figure 4.8 shows the experimentally measured emission profiles at 8V and 14V. At an applied bias of 8V the emission peaked at just below the center of the Alq emission band (520nm [5]). This implies that the majority of the

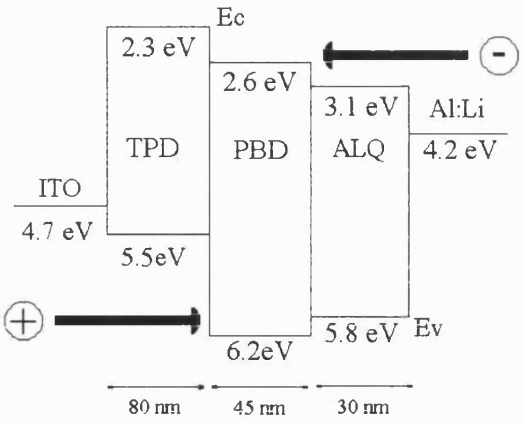

Figure 4.7: Band structure and direction of charge injection

emission is occurring within the Alq layer, with the emission from the TPD or PBD layers being a small fraction of this value.

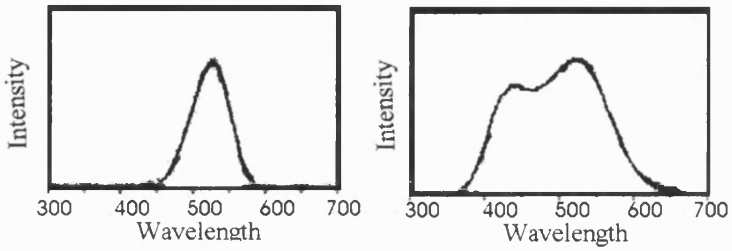

Figure 4.8: Emission spectra (from [4]) for applied biases of 8V (left) and 14V (right)

As the applied bias increased from 8V to 14V there was a broadening [4] of the lower-wavelength region of the emission profile, eventually resulting in a secondary emission peak located at the center of TPD's emission band (420nm [6]). No peak was observed at the PBD emission band center (370nm [7, 8]); emission at this wavelength is most likely due to TPD (as the emission at 370nm increases proportionally with emission at 420 nm).

The low intensities at 370nm combined with the peaks at 420nm and 520nm, implies that the initial description of successive layers from the left as Hole Transporter/Emitter/Electron Transporter was incorrect. From the experimental findings it is reasonable to suggest the materials perform as Hole Transporter/Hole transporter/Emitter at 8V and as Emitter/ Hole Blocker (or Electron Transporter)/Emitter at higher biases. This is in agreement with studies of similar devices - e.g. [9]

Parameter	TPD	PBD	ALQ
χ_c (eV)	2.3	2.6	3.1
E_g (eV)	3.2	3.6	2.7
ϵ_s	3.0	3.0	3.0
N_C (m^{-3})	1×10^{27}	1×10^{27}	1×10^{27}
N_V (m^{-3})	1×10^{27}	1×10^{27}	1×10^{27}
N_{dop} (m^{-3})	-1×10^{15}	-1×10^{15}	1×10^{15}
μ_n (m^2/Vs)	1×10^{-11}	1×10^{-12}	1×10^{-10}
μ_p (m^2/Vs)	1×10^{-9}	1×10^{-10}	1×10^{-12}
E_0 (Vm^{-1})	1.45×10^{8}	2.5×10^{7}	6.5×10^{5}

Table 4.2: Material parameters

To enable study of device emission with an electrical model (which calculates recombination rates rather than emission rates) the assumption was made that the emission from a layer is proportional to the total recombination occuring within that layer, and that all layers share the same constant of proportionality. It was further assumed that for an emission spectrum with 2 peaks, where each peak is centered on a particular layer's emission band, that the ratio of the peak intensities is equal to the ratio of the recombination rates in each layer.

So for the 8V emission spectrum, where only one peak was observed (near the centre of the Alq emission band) the recombination rates in the TPD and PBD layers would be expected to be a small percentage of the rate in the ALQ layer. At 14V the expected TPD recombination rate would be around 80 per cent of the ALQ rate

The device was simulated using the parameters in Table 4.2. The electron and hole barriers, ϕ_{Bn} and ϕ_{Bp}, were taken from the band diagram as 1.1eV and 0.6eV respectively. At each voltage step the total recombination rate within each layer was calculated. Table 4.3 shows the simulated ratio of TPD recombination to Alq recombination from 8 to 14V, along with the experimentally measured ratio of the TPD/Alq emission peaks. Information for the PBD recombination rates are not shown, as they are negligible in both simulation and experiment. At 8V since there is no discernable peak at the TPD emission band, a nominal TPD/Alq emission ratio of 0.05 was assigned.

The results show good qualitative agreement: The ratio of TPD to ALQ increases from being low at 8V to high at 14V. Quantitatively the ratio may be slightly too high at 8V and slightly too low at 14V, but considering the simplicity of our

Voltage	Recombination ratio	Emission peak ratio
8 V	0.16	0.05 (nominal)
10 V	0.27	0.30
12 V	0.43	0.50
14 V	0.68	0.80

Table 4.3: Ratios of TPD/ALQ recombination and emission

assumed relationship between recombination and emission, it is a satisfactory match.

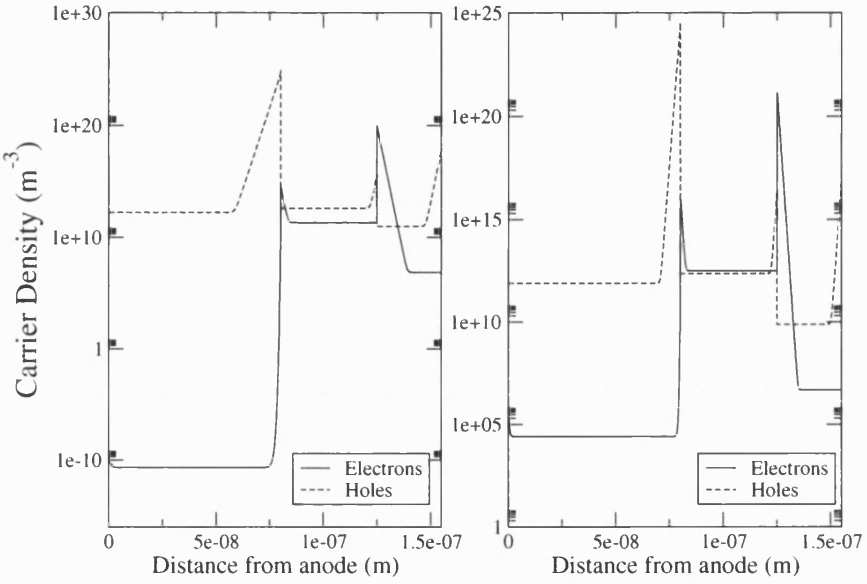

Figure 4.9: Carrier profiles through the device at 8V (left) and 14V (right)

Figures 4.9 and 4.10 show the carrier and recombination profiles through the device at 8V and 14V. As might be expected from Table 4.3, the bulk of the recombination occurs within the TPD and Alq layers. In each layer the peak recombination magnitudes occur at the heterojunction between layers. The relative shapes of the TPD and Alq recombination zones remain roughly the same between 8V and 14V, with the Alq zone being noticeably broader than the narrow TPD zone. However the peak TPD recombination rate shows greater variation with voltage than the Alq peak, resulting in the increasing TPD:Alq peak height ratio.

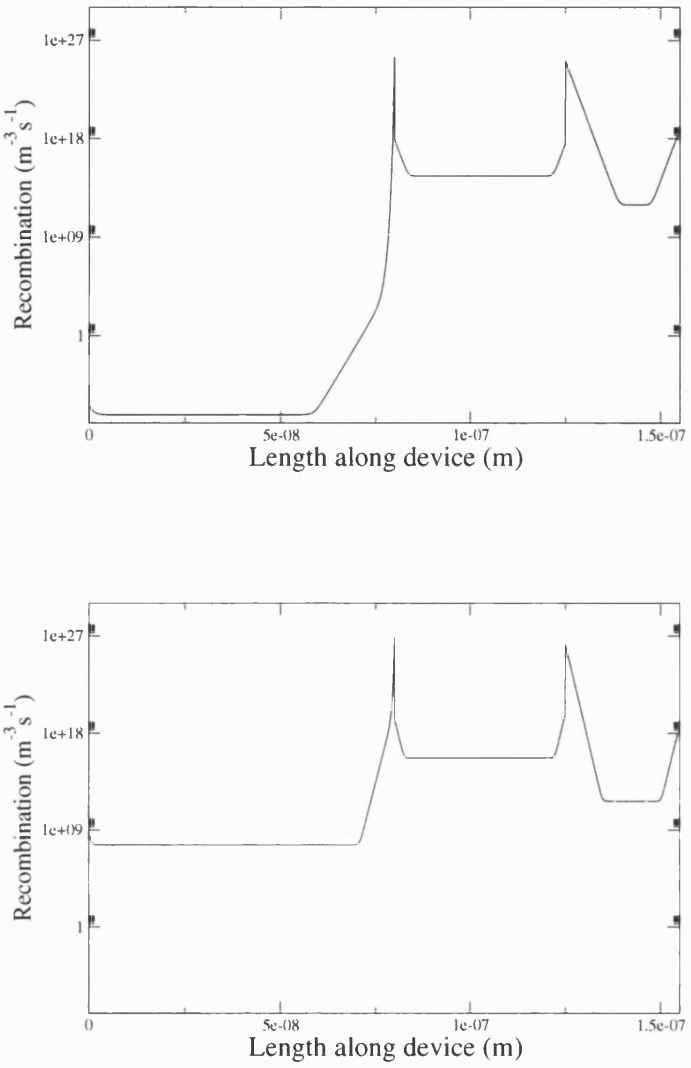

Figure 4.10: Recombination profiles through the device at 8V (top) and 14V (bottom)

Considering this, it would seem that rather than the broadening of recombination region with voltage suggested by [4], the device can be seen as having two separate recombination regions with different voltage responses. For example the recombination within in the TPD layer increases by approximately an order of magnitude between 10 and 14V, while the amount of ALQ recombination only doubles.

These results shows the importance of a detailed and accurate device simulation

in predicting device behaviour for a complex, multi-layered device. A simple analysis of the band structure could lead to the conclusion that the majority of recombination would occur in the PBD layer, and hence that the device would produce light at 390nm. However the simulation predicts that Alq will be the primary emitter, with the TPD emission increasing with the applied bias, which is in agreement with experimental observations. Rather than acting as an emitting layer, PBD is shown to act as a transport/blocking layer.

4.4 Variation in the internal field of SCB11 due to degradation

The device presented in the previous section illustrates one of the methods used to increase device efficiency - the use of multiple layers of small-molecule semiconductors to selectively transport and block carriers to maximise light output. An alternative approach is to use statistical copolymers - that is a polymer constructed of different functional moieties. The composition and ratio of moieties is chosen for specific purposes such as improving electron and hole transport/balance or adjusting HOMO and LUMO levels to reduce the barriers to charge injection.

SCB11 is a statistical copolymer produced by Dow Chemicals Ltd, supplied to Riz Khan et al [10] by Cambridge Display Technology Ltd. The three functional moieties were 9,9-dioctylfluorene , N-(4-butylphenyl)diphenylamine and *bis*-N,N-(4-butylphenyl)-*bis*-N,N-phenyl-1,4-phenylenediamine , respectively the nominal electron transporting, hole transporting and emitting groups.

Electroabsorption (EA) spectroscopy [11] uses an electric field to modulate the transmission of light through an organic thin film semiconductor by perturbing molecular energy levels. EA spectroscopy has been previously been used to measure the electric fields in both mono- and multi-layered OLEDs [12][13] [14][15]
.

EA spectroscopy measurements were made of a series of devices with an Indium Tin oxide (ITO): polyethylenedioxythiophene /polystyrenesulphonate (PEDOT:PSS):SCB11: Au structure [16]. The devices were subjected to a constant

electrical stressing at 120V D.C. for 16.75 hours. Before stressing the electroabsorption ($\frac{\Delta I}{I}$) response was linear between -5V and +5V. After stressing the electroabsorption response had two main differences, firstly the curve was shifted upwards by a constant factor, and secondly the curve sharply changed gradient at around 0.5V.

The electroabsorption response of a semiconductor layer is proportional to the average electric-field within that layer. Thus, for the un-degraded results, there is a constant linear relationship between the electric field in the polymer layer and the applied bias. It was assumed for the un-degraded device that the entire applied bias was across the polymer - i.e. there were no other significant potential drops in the circuit. Using this assumption it was possible to calculate the constant of proportionality between electroabsorption response and electric field.

Looking at the zero applied bias results for the un-degraded and degraded devices in Figure 4.12, the vertical shift in the curves indicates a change in the built-in voltage, which was taken to be due a change in the PEDOT workfunction of 0.8eV. This drop in the workfunction was qualitatively confirmed by analysis of PEDOT from the degraded device with a Kelvin probe (the small size of the PEDOT sample compared to the probe prevented a precise measurement).

Additionally the fact that the degraded $\frac{\Delta I}{I}$ curve has a shallower (and variable) gradient to the un-degraded curve means that the field in the degraded polymer increases less rapidly with voltage. This implies that the potential difference across the degraded polymer, at a particular applied bias, is less than in the un-degraded case. Or , in terms of an electrical circuit, the degraded device is behaving in a similar fashion to a potential divider circuit, with a significant proportion of the applied bias dropped over a region other than the polymer.

It was suggested [17] that the electrical stressing caused the PEDOT/polymer interface to degrade, introducing a non-negligible interfacial resistance and a drop in the effective PEDOT workfunction. To model the resistive properties of the interfacial layer, the simulation was modified to include the effect of a series resistor. The degraded device is treated as being equivalent to the circuit diagram shown in Figure 4.11. The diode in Figure 4.11 is simulated by the drift-diffusion model, while the resistor is modelled by Ohm's law. The voltage across the diode (which, due to the resistor, is less than the applied bias) is re-calculated for each

Parameter	Value
ϵ_s	3.0
μ_{n0} ($m^2V^{-1}s^{-1}$)	1.0×10^{-12}
μ_{p0} ($m^2V^{-1}s^{-1}$)	5.6×10^{-11}
E_{0n} (Vm^{-1})	1.3×10^{6}
E_{0p} (Vm^{-1})	1.3×10^{6}
N_C (m^{-3})	1×10^{27}
N_V (m^{-3})	1×10^{27}
N_{dop} (m^{-3})	-1×10^{10}
E_g (eV)	3.1
χ_c (eV)	2.1
T (K)	290

Table 4.4: Material parameters for SCB11.

iteration of Solvde, as the current changes, to ensure a self-consistent solution.

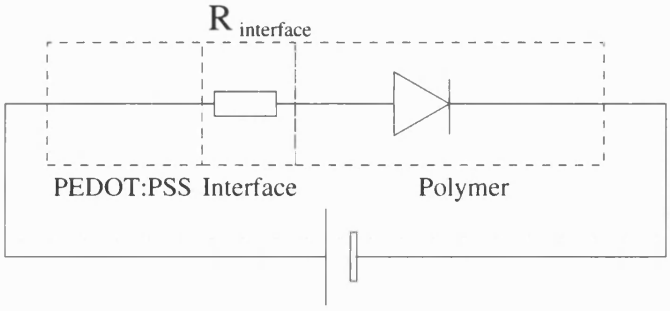

Figure 4.11: Equivalent circuit for the degraded device

The degraded and undegraded devices were simulated with the parameters from table 4.4. The carrier mobilities and HOMO/LUMO energies were measured experimentally [17], all the other parameters were assigned typical values from the literature . The barriers to injection for the un-degraded device were taken as 0.1 eV for ϕ_{Bp} and 1.8 eV for ϕ_{Bn}. The value of ϕ_{Bp} was dropped to 0.9 eV for the degraded device, while ϕ_{Bn} was assumed to remain constant. A set of simulations were carried out treating PEDOT as first a metal-type contact and secondly as a heavily doped semiconductor layer. However it was found that the polymer's simulated Ea curves were the same in both cases, so PEDOT is treated as a metal-type contact hereafter, for the sake of simplicity.

The reverse bias curve has a different gradient in the degraded and undegraded cases. At approximately -5V applied bias, the potential difference across the

degraded polymer is around 1V lower in magnitude than for the undegraded polymer. Considering the reverse bias J-V characteristics this gave an interfacial resistance of $4\times10^{19}\Omega$. Using this value it was also necessary to drop the value of the hole recombination velocity, v_{rp}, at the PEDOT/polymer interface by 4 orders of magnitude to reproduce the kink at 0.5V. Figure 4.12 shows these results.

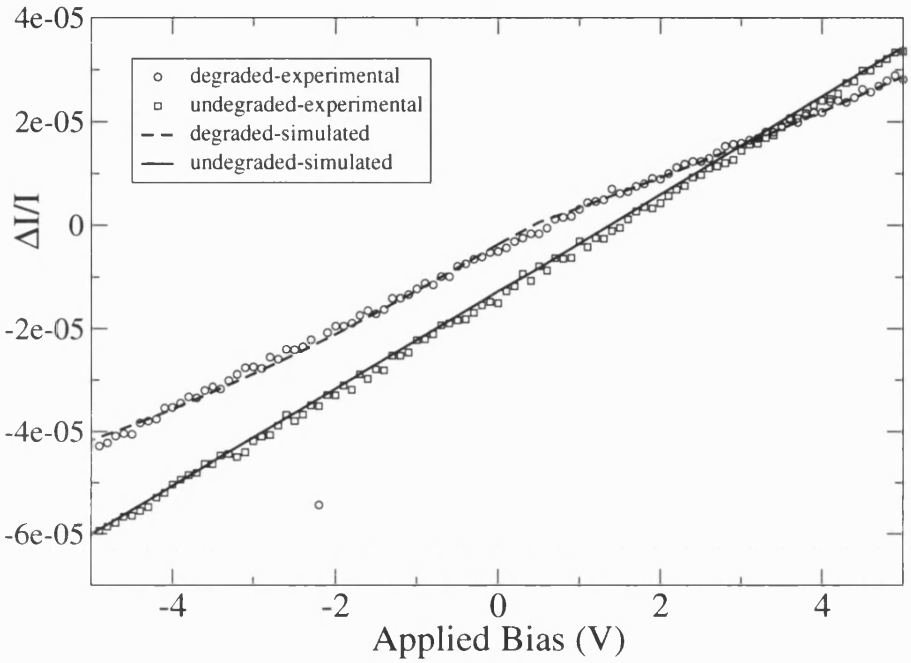

Figure 4.12: Simulated and Experimental EA curves

The simulated results for the un-degraded device are in close agreement with the experimental measurements, however in the case of the degraded device there are fundamental discrepancies between the simulated and experimental data. The simulated reverse bias results for the degraded device are noticeably non-linear, while the corresponding experimental results were observed to be approximately linear. Assuming a constant interfacial resistance, this implied the effective reverse-bias resistance of the polymer should also be constant. However the drift-diffusion theory predicts that the polymer's effective reverse-bias resistance is not constant.

The effective resistance of two resistors in parallel is given by

$$\frac{1}{R_{eff}} = \frac{1}{R_1} + \frac{1}{R_2} \tag{4.1}$$

If $R_2 \rangle\rangle R_1$ then Equation 4.1 will tend to

$$\frac{1}{R_{eff}} \approx \frac{1}{R_1} \tag{4.2}$$

or

$$R_{eff} \approx R_1 \tag{4.3}$$

Thus R_{eff} will remain approximately constant with respect to a varying value of R_2, providing the above inequality holds true.

Figure 4.13: Equivalent circuit for the polymer

With this in mind it was proposed that if the polymer's electrical characteristics were treated as being equivalent to a simple parallel circuit, consisting of a diode and resistor (see Figure 4.13), then the polymer could demonstrate an approximately constant reverse-bias resistance. Relating this to Equations 4.1-4.3, the diode (here considered analogous to a voltage-dependent variable resistor) is R_2, the parallel resistor is R_1 and R_{eff} is the effective resistance of the polymer layer.

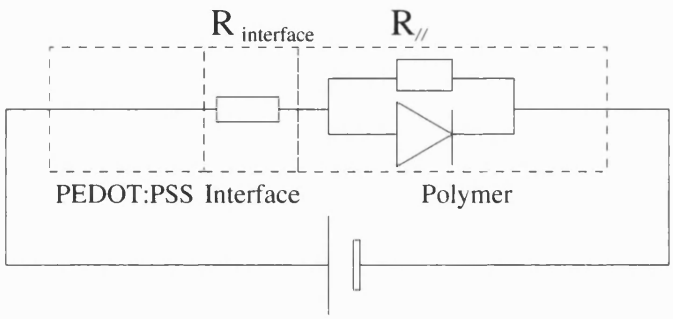

Figure 4.14: Updated circuit diagram for the degraded device

The simulation was further modified to account for the effect of a parallel resistor. The degraded device is now treated as being equivalent to the circuit diagram shown in Figure 4.14. As before, the drift-diffusion model was used to simulate the diode, while the parallel resistor was simulated in a similar fashion to the interfacial resistance (using Ohm's law). In the next section, further evidence is presented to justify the inclusion (and physical origin), of this parallel resistance, $R_{//}$.

The un-degraded and degraded devices were again simulated using the parameters from Table 4.4. The approximate values of $R_{//}$ and $R_{interface}$ were deduced from analysis of the experimental ea results and simulated J-V curves. It was found that setting $R_{//}$ to $2.5\times10^{9}\Omega$ and $R_{interface}$ to $5.0\times10^{8}\Omega$ gave the best fit to the experimental data. The results obtained with these values are shown in Figure 4.15.

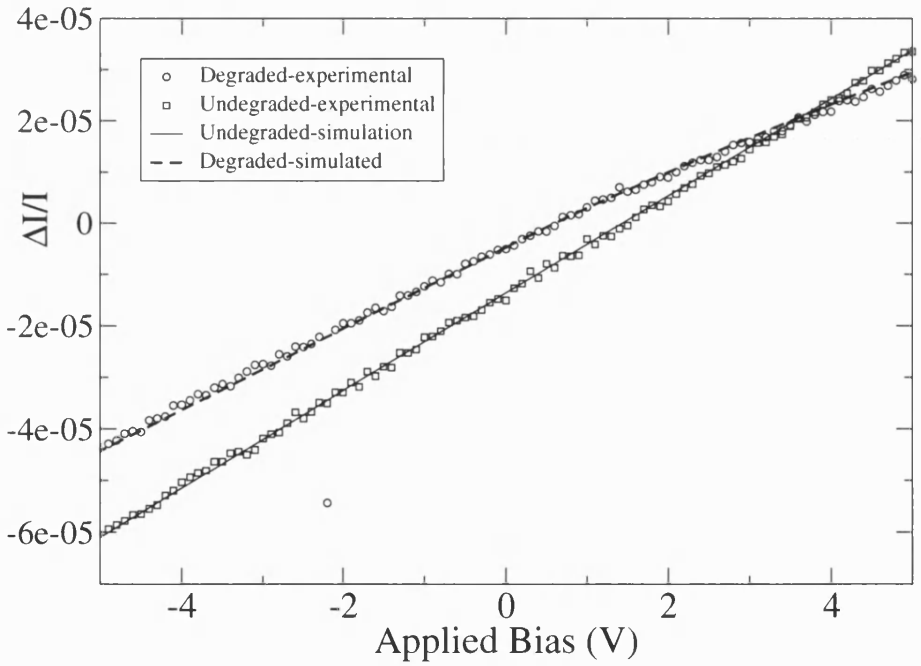

Figure 4.15: Simulated and Experimental EA curves

The experimental and simulated results are in exceptionally close agreement, for both the un-degraded and degraded devices. The simulated reverse-bias results for the degraded device are now perfectly linear, while at forward bias the kink

Device	Structure
1	ITO/PEDOT(200nm)/SCB11(80nm)/LiF(1nm)/Ca (5nm)/Al
2	ITO/PEDOT(200nm)/SCB11(80nm)/LiF(2nm)/Ca (5nm)/Al
3	ITO/PEDOT(200nm)/SCB11(80nm)/LiF(3nm)/Ca (5nm)/Al
4	ITO/PEDOT(200nm)/SCB11(80nm)/LiF(3nm)/Ca (5nm)/Al
5	ITO/PEDOT(200nm)/SCB11(80nm)/LiF(4nm)/Ca (5nm)/Al
6	ITO/PEDOT(200nm)/SCB11(80nm)/LiF(4nm)/Ba (5nm)/Al

Table 4.5: Device composition (from [17])

is also reproduced accurately.

4.5 Modelling the I-V characteristics of SCB11

The I-V measurements of a set of 6 SCB11-based devices, identical except for cathode material and thickness, displayed approximately linear behaviour at applied biases below that of the built-in voltage. In this range of biases the I-V curves closely resembled that of an Ohmic conductor (other groups have also observed this kind of behaviour e.g. [18]). This leakage current was not noticeable at biases above the built-in voltage as once the applied bias overcomes the devices built-in field, the magnitude of the exponentially increasing thermionic-emission current far outweighed the linearly increasing magnitude of the leakage current.

These effects were initially attributed to material defects causing an electrical "short" across the polymer layer. It is difficult, if not impossible, to model these effects with a purely drift-diffusion based simulation as they are due to physical effects outside the scope of the model.

As mentioned above, the devices were identical except for the cathode thickness and composition. Table 4.5 lists the structure for each device. Increasing the thickness of the LiF cathode was observed to increase the device's built-in voltage over a rough range of 2.4V to 2.55V.

Initial attempts to replicate the J-V curve focused on biases above the built-in voltage. It was found that simulating a device using Time-Of-Flight (TOF) measured values produced current-densities approximately two orders of mag-

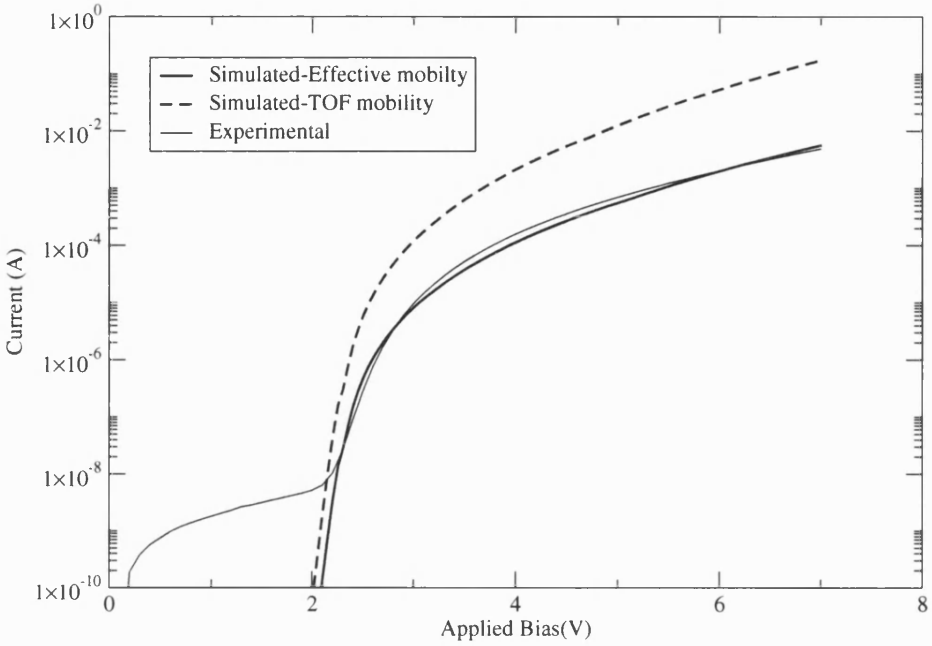

Figure 4.16: Simulated and Experimental I-V curves

nitude too high. Reference [17] obtained similar results using a simple Space-Charge-Limited (SCL) electrical model. It was possible to reproduce the upper bias I-V data by assigning an effective (calculated by curve fitting) mobility to SCB11. Figure 4.16 shows the experimental and simulated J-V curves for an ITO/PEDOT(200nm)/SCB11(80)/LiF(4nm)/Ca/Al device (device 5 from Table 4.5) using both the TOF (measured) and effective mobilities. Table 4.6 lists the simulation parameters.

The results from the drift-diffusion simulation show good agreement with experiment at biases beyond the built-in voltage; similarly good fits were obtained for the other devices in table 4.5. Below the built-in voltage the simulated current is many orders of magnitude too small, additionally an explanation is required as to why the effective steady-state mobility varies from the measured TOF values.

In the previous section a parallel resistance was introduced into the simulation to ensure the polymer's effective resistance was roughly constant at low- and reverse-bias. The above I-V curve implies that the polymer has a fixed resistance

Parameter	SCB11 (Effective mobility)	SCB11 (TOF mobility)
ϵ_s	3.0	3.0
μ_{n0} ($m^2V^{-1}s^{-1}$)	1.0×10^{-12}	1.0×10^{-12}
μ_{p0} ($m^2V^{-1}s^{-1}$)	5.6×10^{-11}	5.6×10^{-12}
E_{0n} (Vm^{-1})	2.0×10^{6}	1.3×10^{6}
E_{0p} (Vm^{-1})	2.0×10^{6}	1.3×10^{6}
N_C (m^{-3})	1×10^{27}	1×10^{27}
N_V (m^{-3})	1×10^{27}	1×10^{27}
N_{dop} (m^{-3})	-1×10^{10}	-1×10^{10}
E_g (eV)	3.1	3.1
χ_c (eV)	2.1	2.1
ϕ_{Bp} (eV)	3.0	3.0
ϕ_{Bn} (eV)	0.5	0.5
T (K)	290	290
Device area (m^2)	9×10^{-6}	9×10^{-6}

Table 4.6: Material parameters for SCB11.

at low bias, so we have again visualised the electrical properties of the polymer as being equivalent to a simple parallel circuit, consisting of a diode and resistor (see Figure 4.17). For a particular bias we can state the total current flowing through the device is equal to the current flowing through diode, plus the current through the resistor. The diode current is calculated, as normal, by the drift-diffusion simulation. The current through the resistor is calculated via Ohm's law.

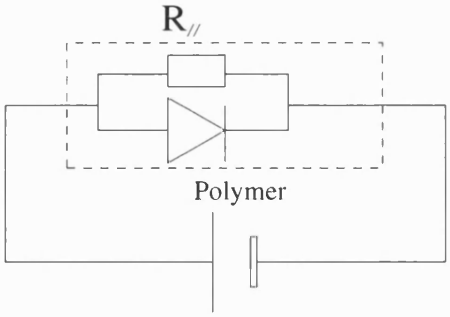

Figure 4.17: Equivalent circuit for the devices from Table 4.5

It was proposed that the discrepancy between the simulated steady-state (effective) and experimentally measured transient (TOF) mobilities was caused by the presence of deep trap sites within the polymer, that would reduce the magnitude of the steady state current without noticeably affecting the mobility measurements from TOF experiments. This would mean that the above-v_{bi} experimental I-V measurements could be fitted with the TOF mobilities, provided an appro-

priate trap distribution was used.

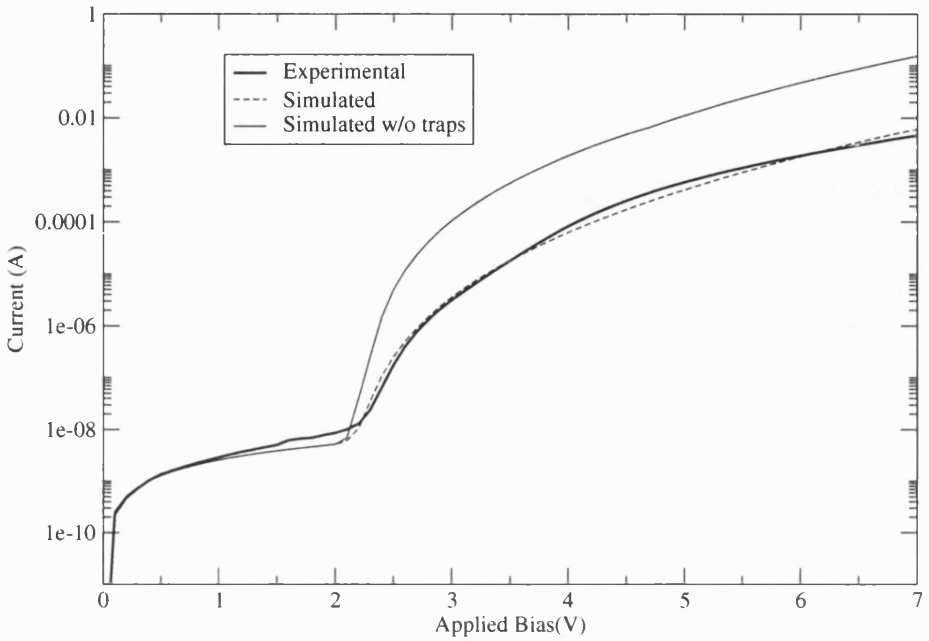

Figure 4.18: Simulated and Experimental I-V curves for device 1

The resistance of the resistor was derived from the experimental results. It is reasonable to say that the thermionic-emission current is negligible at low bias (at 0.5V the drift-diffusion model predicts currents at least 5 orders of magnitude smaller than measured) and so the current through the resistor will be equal to the measured current. Resistance values were calculated by dividing the applied bias by experimental current for biases from 0.1V to 1.0V and then averaging.

For device 1, a level of traps at 2.8eV (0.3 eV above the HOMO) with a density of 4×10^{23} m^{-3} was found to give the best fit between the simulated and experimental I-V curves. Figure 4.18 shows the results obtained in this manner, alongside the experimental data. The results obtained by excluding traps from the simulation (no changes were made to $R_{//}$) are shown for comparison.

The results for device 1 are discussed along with results for devices 2-6, on the next page. However it is worth noting that the difference between the untrapped and trapped I-V curves in Figure 4.18 is similar to the difference between the

Parameter	Value
ϵ_s	3.0
μ_{n0} ($m^2V^{-1}s^{-1}$)	1.0×10^{-12}
μ_{p0} ($m^2V^{-1}s^{-1}$)	5.6×10^{-11}
E_{0n} (Vm^{-1})	1.3×10^{6}
E_{0p} (Vm^{-1})	1.3×10^{6}
N_C (m^{-3})	1×10^{27}
N_V (m^{-3})	1×10^{27}
N_{dop} (m^{-3})	-1×10^{10}
E_g (eV)	3.1
χ_c (eV)	2.1
E_T (eV)	2.8
N_T (m^{-3})	4×10^{23}
$R_{//}$ (Ωm^2)	2.5×10^{3}
ϕ_{Bp} (eV)	3.0
ϕ_{Bn} (eV)	0.5
T (K)	290
Device area (m^2)	9×10^{-6}

Table 4.7: Material parameters for SCB11.

TOF and effective mobility curves in Figure 4.16. This demonstrates that the effect of including traps (at least when simulating I-V curves) can appear similar to an alteration in carrier mobility.

The remaining devices from Table 4.5 were simulated using the parameters from Table 4.7. For each device the electron injection barrier, parallel resistance and trap density were adjusted for an optimum fit. Table 4.8 lists the values of ϕ_{Bn}, $R_{//}$ and N_T used in each simulation (note that the parameters for Device 1 are the same as those in Table 4.7. Each device was also simulated without traps or a parallel resistance for comparison. Figure 4.19 shows the results obtained using these parameters.

The inclusion of traps and a parallel resistance in the simulation allows a fairly good agreement with experiment to be reached. However, at higher bias the slope of the simulated I-V curves are steeper than those of the experimental curves. This could be (referring back to the results in Figure 4.16) because the field-dependence factor , E_0, used in the simulation is too high. Alternatively the problem may lie in the choice of trap parameters used in the simulation. Trap-filling can reduce the I-V gradient, due to injected carriers being removed from the

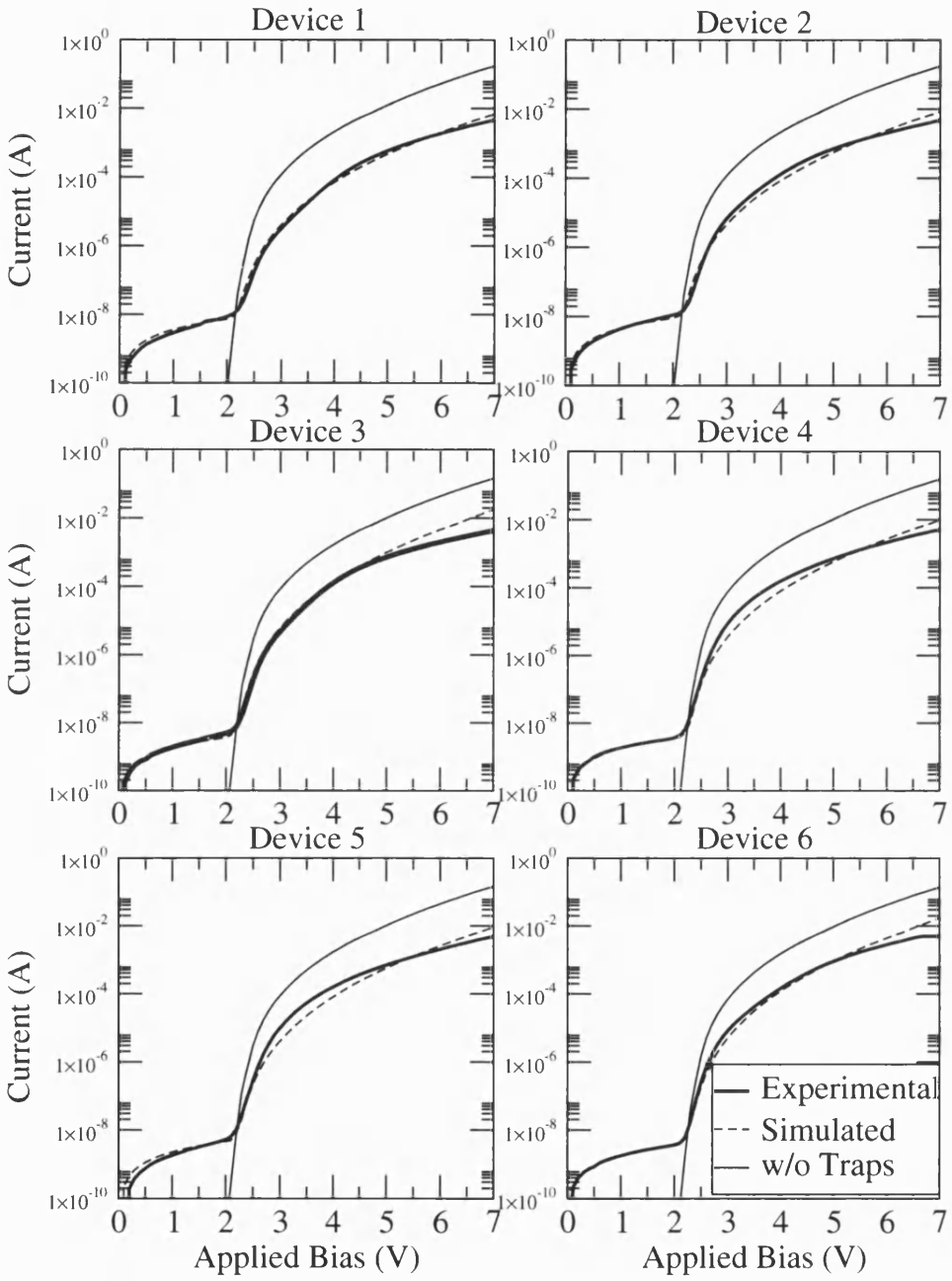

Figure 4.19: Simulated and Experimental I-V curves for devices 1-6

Device	ϕ_{Bn} (eV)	N_T (m^{-3})	$R_{//}$ (Ωm^2)
1	0.5	4.0e23	2.5e3
2	0.5	3.5e23	2.0e3
3	0.45	2.0e23	5.0e3
4	0.4	3.0e23	5.0e3
5	0.45	3.0e23	4.0e3
6	3.0	2.0e23	5.0e3

Table 4.8: Material parameters for SCB11.

HOMO and LUMO bands by the traps. Since with the current trap parameters the majority of the traps fill below 6V, there are not enough free traps at higher voltages to reduce the I-V gradient. This problem cannot be solved by merely increasing the trap density as this would also reduce the magnitude of the mid to low bias currents. The parallel resistance produces an excellent fit to the sub-v_{bi} for devices 2,3,4 and 6, however for devices 1 and 5 there is a slight discrepancy between experiment and simulation, which is attributed to experimental error.

The trap energy used in the simulation may have been too low ([17] suggested that the presence of the f8t group could introduce a trap level at 0.5 eV above the valence band with a density that could be a significant percentage of the polymer's density of states - perhaps even as high as 1×10^{26} m^{-3}). It is possible that a larger trap density at a higher energy might result in trap-filling over a wider range of biases , while still using the experimentally measured field-dependence values. If significant trap-filling was to occur up to 7V then the I-V gradient at 7V could be reduced by an appropriate amount, to fit the experimental results.

This section has attempted to model two experimentally observed effects separately - an unexpectedly high current at low bias, and an unexpectedly low current at high bias. These were explained by the introduction of a parallel resistance and deep traps respectively. To investigate whether these parameters were connected - perhaps by being produced the same physical property of the polymer, a scatter-diagram, Figure 4.20, of trap density vs parallel resistance (from Table 4.8) was plotted.

A linear relationship between trap density and parallel resistance, with a negative constant of proportionality, was extrapolated using a least-squares method from Figure 4.20. This shows the low bias parallel resistance decreasing with

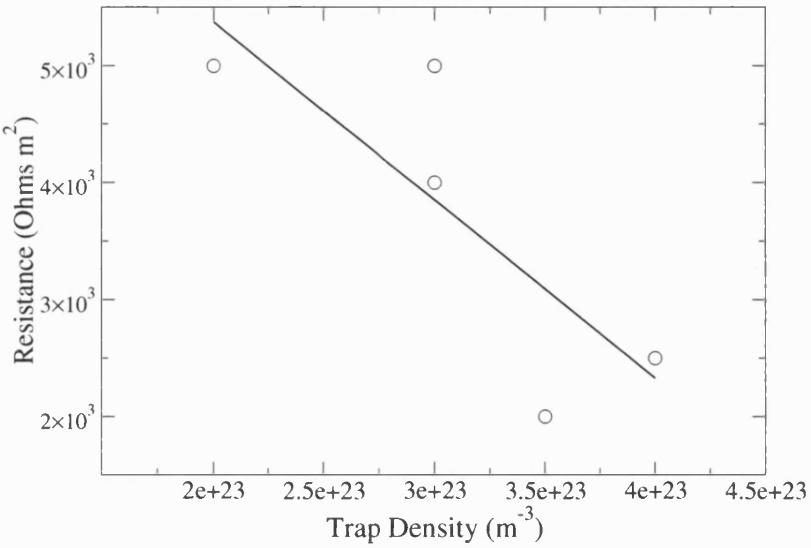

Figure 4.20: Trap density vs parallel resistance for devices 1-6

increasing trap density. For each device values of trap density and parallel resistance were obtained from separate regions of the I-V curve by separate fitting methods. Thus any link between the two variables must be due to a real physical relationship, as opposed to an artifact of the fitting process. An inverse relationship between resistance and density is consistent with analytic expressions for impurity transport in inorganic semiconductors [19].

This apparent link between trap density and low-bias conductivity could be interpreted as implying that the leakage current is due to carrier injection/transport via trap states (illustrated in Figure 4.21). Although the trap energy levels are non-continuous in the band model, carriers could jump between trap states (depending on the spatial separation of the states [19]) just as band conduction in an organic semiconductor is due to carriers hopping between the states that form the HOMO and LUMO levels. Transport mechanisms involving trap/impurity states have previously been used to explain a number of experimental observations, including low bias currents [20] and degradation of internal field [21].

Note that the above explanation is based on the comparison of fitted parameters for a small number of devices. Ideally a functional relationship between traps and resistance would be identified by expanding Figure 4.20 with data from a

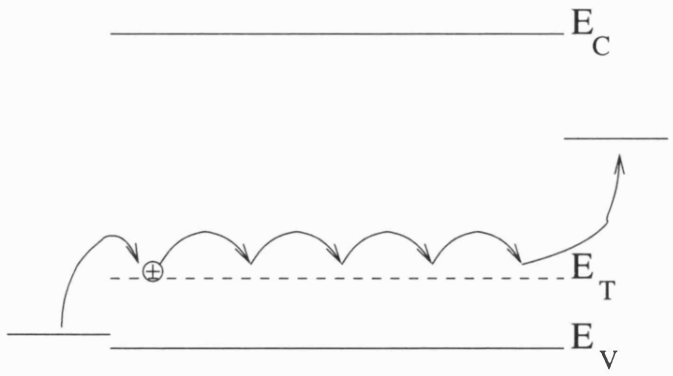

Figure 4.21: Injection/transport via trap energy levels

larger set of devices.

4.6 Conclusions

The devices studied in this section represent two approaches used in OLED design to (hopefully) increase device efficiency - multiple layers and statistical copolymers. The above results are from the first attempts to use the model to simulate statistical copolymer and tri-layer small molecule devices.

By using a crude approximation between recombination and photon emission it was possible to qualitatively reproduce the observed emissive shifts for a tri-layer device. In the next section the appropriateness of this basic emission model is discussed along with the introduction of a full optical model (based on microcavity effects) to the simulation. Additionally by using an electrical model, it is possible to obtain a far more detailed view of device operation and material behaviour than by only considering band structure energetics or analytic expressions. In the case of the tri-layer device PBD, which [4] classified as an emitter, was shown to act as a transport/blocking material.

When simulating the electrical properties of SCB11 the drift-diffusion simulation initially proved to be inadequate to reproduce experimentally observed device characteristics. Resistive effects, attributed to material defects within the polymer and PEDOT:PSS/polymer interface, were introduced into the model to explain device behaviour. Simulations of the I-V and E-V characteristics were

generally in good agreement with the experimental results. The EA results were particularly well reproduced for both the degraded and undegraded devices.

The fact that a parallel resistance was required for both the EA and I-V simulations, offers justification for its inclusion in the device model. Furthermore when traps are introduced to explain higher bias I-V behaviour, there appears to be a relation between trap density and the magnitude of the parallel resistance. With this in mind the explanation is proposed that the leakage current observed at low bias is due to injection and transport of carriers via trap energy levels.

References

[1] S. J. Martin *PhD Thesis*, University of Bath, (2002)

[2] C. D. J. Blades, *Ph.D. Thesis*, University of Bath (2000).

[3] B. K. Crone, P. S. Davids, I. H. Campbell and D. L. Smith, "Device model investigation of bilayer organic light emitting diodes" , *J. Appl. Phys.*, **87**, 1974 (2000).

[4] J.-H. Lee, S.-W. Kim, S.-H. Ju, W.-G. Lee, J.-S. Choi, Y.-K. Kim, W.-Y. Kim, "Emission shift by recombination effect in a three-layered OLED" ,*Synth. Met.*, **111-112**, 63 (2000)

[5] C. Qiu, H. Chen, M. Wong, and H. S. Kwok, "Device Emission Mechanism and the Effects of Host Materials on the Behvaiour of Doped Organic Light-Emitting Diodes" , *IEEE. Trans. Elec. Dev.*, **49**, 1340 (2002)

[6] C. F. Qiu, L. D. Wang, H. Y. Chen, M. Wong, and H. S. Kwok, "Room-temperature ultraviolet emission from an organic light-emitting diode" , *Appl. Phys. Lett*, **79**, 2276 (2001)

[7] T. D. de Morais, F. C., K. Lahlil, and J.-P. Boilot, "Hybrid Organic-Inorganic Light-Emitting Diodes" , *Adv. Mater.*, **11**, 107 (1999)

[8] M. A. Diaz-Garcia, S. F. de Avila and M. Hernandez, "Dye-doped polymers for blue organic diode lasers" , *Appl. Phys. Lett.*, **80**, 4486 (2002)

[9] K. Okumoto and Y. Shirota, "Development of high-performance blue-violet-emitting organic electroluminescent devices" *Appl. Phys. Lett.*, **79**, 1231 (2001)

[10] R. U. A. Khan, T. Kreouzis, Dmytro Poplavskyy and D. D. C Bradley, "Hole injection and transport in a fluorene-containing copolymer" *Preprint* (2003)

[11] F. Rohlfing and D. D. C. Bradley, "Optical non-linearity in beta-carotene: new insight from electroabsorption spectroscopy", *Chemical Physics*, **227**, 133 (1998).

[12] T. M. Brown, R. H. Friend, I. S. Millard, D. J. Lacey, J. H. Burroughes, and F. Cacialli, *Appl. Phys. Lett.*, "LiF/Al cathodes and the effect of LiF thickness on the device characteristics and built-in potential of polymer light-emitting diodes", **77**, 3096 (2000).

[13] F. Rohlfing, T. Yamada, and T. Tsutsui, "Electroabsorption spectroscopy on tris-(8-hydroxyquinoline) aluminum-based light emitting diodes", *J. Appl. Phys.*, **86**, 4978 (1999).

[14] S. J. Martin, G. L. B. Verschoor, M. A. Webster, and A. B. Walker, "The internal electric field distribution in bilayer organic light emitting diodes", *Org. Electron.*, **3-4**, 129 (2002).

[15] I. H. Campbell, M. D. Joswick, and I. D. Parker, "Direct measurement of the internal electric-field distribution in a multilayer organic light-emitting diode", *Appl. Phys. Lett.*, **67**, 3171 (1995).

[16] R. U. A. Khan, D. D. C Bradley, M. A. Webster, J. L. Auld and A. B. Walker, "Performance degradation in blue light-emitting conjugated polymer diodes due to a loss of ohmic hole injection" , *Preprint* (2003)

[17] R. U. A Khan, *Private Communication* (2002-2003)

[18] D. J. Pinner, R. H. Friend, and N. Tessler, "Transient electroluminescence of polymer light emitting diodes using electrical pulses", *J. Appl. Phys.*, **86**, 5116 (1999).

[19] N. F. Mott and E. A. Davis, *Electronic Processes in Non-Crystalline Materials*, Clarendon Press, Oxford (1971)

[20] J. M. Lupton and I. D. W. Samuel, "Temperature-dependent single carrier device model for polymeric light emitting diodes", *J. Phys. D.:Appl. Phys.*, **32**, 2973 (1999).

[21] F. Feller, D. Geschke and A. P. Monkman, "Spatial Distribution and Dynamics of Space-Charges in poly(2,5-pyrinediyl)" , *J. Phys.:Cond. Matt.*, **14**, 8455 (2002)

Chapter 5

Light emission in a thin-film microcavity

There are a number of methods by which the light emitted by a singlet recombining can be modelled (e.g. [1, 2, 3, 4]. The method described in this thesis is from [5], which uses the theory from [6, 7, 8, 9] and is based on the equivalence between an oscillating dipole antenna and the probabilities of a recombinative dipole transition. This theory allows the calculation of the power radiated by a dipole antenna within a microcavity, which in turn provides the change in radiative decay rate for dipole transitions.

5.1 The propagation of light in a microcavity

Figure 5.1 shows a thin-film structure, consisting of a stack of dielectric layers,orthogonal to the x-axis, terminated by two half-infinite media. Each layer is referred to by a parameter i, so the refractive index and layer thickness for a particular layer are referred to as n_i and d_i respectively. Of special note are the emitting layer (the layer in which photons are generated) and the half-infinite boundaries, which are labelled as e, $+$ and $-$ respectively.

In a layer with a refractive index of n_i, light with a wavelength λ has the corresponding wavevector k_i.

Figure 5.1: Thin film structure, terminated by two half-infinite media

$$k_i = \frac{2\pi n_i}{\lambda} \tag{5.1}$$

The component of the wavevector in the x direction, k_x, i, is given by:

$$k_x, i = (k_i^2 - \kappa^2)^{1/2} \tag{5.2}$$

where k_x, i is taken as the complex square root in the first quadrant of the complex plane and κ is defined as:

$$\kappa = (k_{y,i}^2 - k_{z,i}^2)^{1/2} \tag{5.3}$$

If both k_i and κ are real, and k_i is greater in magnitude than κ then Equation 5.3 can be rewritten as:

$$\kappa = (k_i sin\alpha_i) \tag{5.4}$$

where α_i is the angle between k_i and the x-axis (see Figure 5.2).

Figure 5.2: orthogonal component of the wavevector

For a wave propagating through a layer i, the complex Fresnel coefficients for reflection and transmission, $r_{i,i\pm1}$ and $t_{i,i\pm1}$, between adjacent layers,i$\pm$1, are given by:

$$r_{i,i\pm1}^{TM} = \frac{k_{x,i}/n_i^2 - k_{x,i\pm1}/n_{i\pm1}^2}{k_{x,i}/n_i^2 + k_{x,i\pm1}/n_{i\pm1}^2} \tag{5.5}$$

$$r_{i,j}^{TE} = \frac{k_{x,i} - k_{x,i\pm1}}{k_{x,i} + k_{x,i\pm1}} \tag{5.6}$$

$$t_{i,i\pm1}^{TM} = 1 + r_{i,i\pm1}^{TM} \tag{5.7}$$

$$t_{i,i\pm1}^{TE} = 1 + r_{i,i\pm1}^{TE} \tag{5.8}$$

a 'TM' superscript indicates the Fresnel coefficient for TM polarised waves while a 'TE' superscript likewise refers to waves with TE polarisation. Figure 5.3 illustrates the labelling convention used in the above equations.

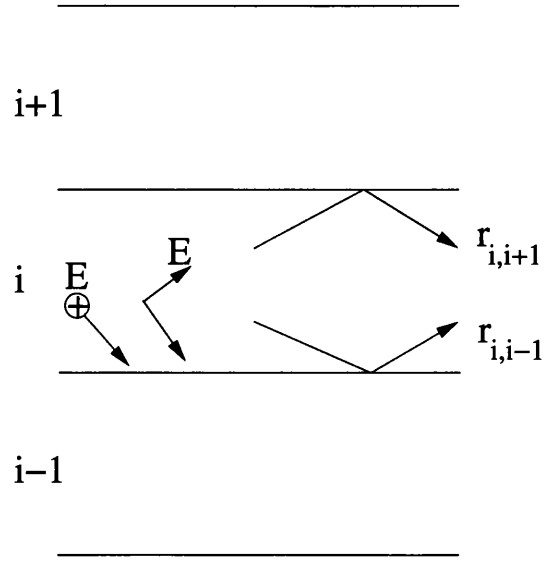

Figure 5.3: sign conventions for Fresnel coefficients

For two layers, labelled i and j, separated by an arbitrary number of intermediary layers, the total reflection and transmission coefficients can be determined by a recursive algorithm:

$$r_{i,j} = \frac{r_{i,i\pm1} + r_{i\pm1,j}\exp(2jk_{x,i\pm1}d_{i\pm1})}{1 + r_{i,i\pm1}r_{i\pm1,j}\exp(2jk_{x,i\pm1}d_{i\pm1})} \tag{5.9}$$

$$t_{i,j} = \frac{t_{i,i\pm1}t_{i\pm1,j}\exp(2jk_{x,i\pm1}d_{i\pm1})}{1 + r_{i,i\pm1}r_{i\pm1,j}\exp(2jk_{x,i\pm1}d_{i\pm1})} \tag{5.10}$$

where $d_{i\pm1}$ is the layer length.

In practice Equations 5.9 and 5.10 are used to determine the total reflection\transmission coefficients between the emitting layer and free space, $r_{e,\pm}$ and $t_{e,\pm}$. The energy reflection and transmission coefficients, $R_{e,\pm}$ and $T_{e,\pm}$, are derived from the amplitude coefficients:

$$R_{e,\pm}^{TM,TE} = |r_{e,\pm}^{TM,TE}|^2 \tag{5.11}$$

$$T_{e,\pm}^{TM} = |t_{e,\pm}^{TM}|^2 \frac{n_e^2}{n_\pm^2} \frac{k_{x,\pm}}{|k_{x,e}|} \tag{5.12}$$

$$T_{e,\pm}^{TE} = |t_{e,\pm}^{TE}|^2 \frac{k_{x,\pm}}{|k_{x,e}|} \tag{5.13}$$

note that $T_{e,\pm}^{TM}$ and $T_{e,\pm}^{TE}$ are taken to be zero when $k_{x,\pm}$ has a nonzero imaginary component, since there is no transmission, due to medium's absorbing nature.

5.2 An Emitting Dipole Antenna in a Microcavity

The total power (ignoring time-based behaviour) emitted by an elementary dipole antenna with dipole moment p_0 and frequency v in an infinite medium of refractive index n_e is given by:

$$L_e = \frac{v k_e^3}{6 n_e^2 \epsilon_0} p_0^2 \tag{5.14}$$

The ratio of the actual power emitted by a dipole to Equation 5.14, here denoted as F, is used to simplify studying microcavity effects. For the case of a dipole in a infinite medium, F is equal to one. The total power output of a dipole antenna (including losses due to absorbing media and output into free space) can then be expressed as:

$$F = \int_0^\infty K(\kappa) \mathrm{d}\kappa^2 \tag{5.15}$$

where K is the power density per $\mathrm{d}\kappa^2$. For a dipole antenna at an angle of θ to the x axis, the TM and TE components of the power density can be expressed as a function of the TM and TE power densities of a dipole parallel or perpendicular to the x axis:

$$K_\theta^{TM} = K_\perp^{TM} \cos^2\theta + K_\parallel^{TM} \sin^2\theta \tag{5.16}$$

with a similar expression for K_θ^{TE}. For dipoles with a random orientation, integrating over θ gives:

$$K_{Random}^{TM} = \frac{1}{3} K_\perp^{TM} + \frac{2}{3} K_\parallel^{TE} \tag{5.17}$$

$$K_{Random}^{TE} = \frac{1}{3} K_\perp^{TE} + \frac{2}{3} K_\parallel^{TE} \tag{5.18}$$

where $K_\perp^{TM}, K_\parallel^{TM}, K_\perp^{TE}, K_\parallel^{TE}$ are defined as:

$$K_\perp^{TM} = \frac{3}{4} Re\left[\frac{\kappa^2}{k_e^2 k_{x.e}} \frac{(1+\alpha_+^{TM})(1+\alpha_-^{TM})}{1-\alpha^{TM}}\right] \tag{5.19}$$

$$K_\parallel^{TM} = \frac{3}{8} Re\left[\frac{k_{x,e}}{k_e^3} \frac{(1-\alpha_+^{TM})(1-\alpha_-^{TM})}{1-\alpha^{TM}}\right] \tag{5.20}$$

$$K_\perp^{TE} = 0 \tag{5.21}$$

$$K_\parallel^{TE} = \frac{3}{8} Re\left[\frac{1}{k_e k_{x.e}} \frac{(1+\alpha_+^{TE})(1+\alpha_-^{TE})}{1-\alpha^{TE}}\right] \tag{5.22}$$

where the α coefficients are defined as

$$\alpha_+^{TM,TE} = r_{e,+}^{TM.TE} \exp(2jk_{x,e}x_+) \tag{5.23}$$

$$\alpha_-^{TM,TE} = r_{e,-}^{TM.TE} \exp(2jk_{x,e}x_-) \tag{5.24}$$

$$\alpha^{TM,TE} = \alpha_{+}^{TM,TE}\alpha_{-}^{TM,TE} \tag{5.25}$$

The α coefficients represent the majority of the microcavity effects; The numerator in Equations 5.19-5.22 which is of the form $(1 \pm \alpha_{+})(1 \pm \alpha_{-})$ represents wide-angle interference effects (interference between directly emitted and reflected radiation). The denominator which is of the form $(1 - \alpha)$ represents multiple-beam interference effects (interference between repeatedly reflected radiation). Figures 5.4 and 5.5 illustrate these interference types.

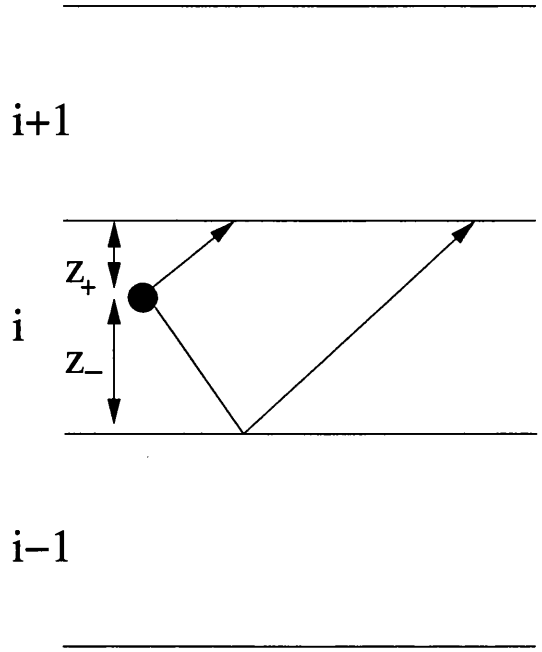

Figure 5.4: Wide-angle interference

5.3 Radiative and Non-radiative Dipole Transitions in a microcavity

So far the optical model has been concerned with a dipole antenna, which emits continuous radiation. However, the dipoles (the excitons) in an organic semiconductor emit discrete radiation, during transitions from an excited state to a ground state.

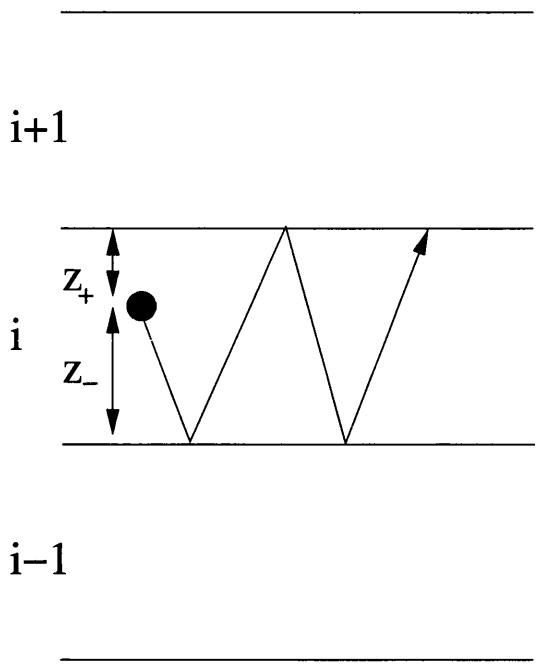

Figure 5.5: Multiple-beam interference

When a dipole antenna's power output is altered due to microcavity effects, the probability of a discrete radiative transition is altered by the same amount. For a dipole at a position x inside the dielectric stack, with free-space radiative and non-radiative decay rates of τ_r and τ_{nr} respectively, the probability of a radiative transition resulting in emission into free space, relative to the free-space probability is:

$$p_{decay} = \frac{\tau_{nr} + \tau_r}{\tau_{nr} + F(x)\tau_r} E_{coupling}(x) \tag{5.26}$$

where $E_{coupling}$ is the transmission (out-coupling) probability of a photon with a real wave-vector.

$$E_{coupling} = \int_0^{k_+^2} K(\kappa) \mathrm{d}\kappa^2 \tag{5.27}$$

The radiative and non-radiative decay rates,τ_r and τ_{nr}, are related to the total decay rate, τ_s, by the photoluminescent (PL) efficiency

$$\eta_{PL} = \frac{\tau_r}{\tau_s} = 1 - \frac{\tau_{nr}}{\tau_s} \tag{5.28}$$

and τ_s is defined as

$$\tau_s = \tau_{nr} + \tau_r \tag{5.29}$$

note that τ_r is the free-space radiative decay rate, in a microcavity the radiative decay rate is given by $F\tau_r$ and Equation 5.29 becomes:

$$\tau_s = \tau_{nr} + F\tau_r \tag{5.30}$$

5.4 Electro-Optical Model

To calculate the light output the density of singlet (radiatively decaying) excitons is required. The continuity equation for excitons is

$$\frac{\partial S(x,t)}{\partial t} = r_{st}R_{opt} + D_S\frac{\partial^2 S(x,t)}{\partial x^2} - \tau_s(x)S(x,t) \tag{5.31}$$

or for the steady-state case:

$$\tau_s(x)S(x) = r_{st}R_{opt} + D_S\frac{\partial^2 S(x)}{\partial x^2} \tag{5.32}$$

where $S(x,t)$ and $S(x)$ are the singlet densities, D_S is the exciton diffusion rate, taken here as $L_D^2\tau_s$ where L_D is the exciton diffusion length and τ_s the singlet decay rate, r_{st} is the singlet to triplet ratio, R_{opt} is the Langevin recombination rate and $\tau_s(x)$ is the position-dependent singlet decay rate. Note that Equations 5.31 and 5.32 use quantities calculated from the drift-diffusion and optical models, and so can be seen as the link between the two models.

Once the singlet profile is known (by solving Equation 5.32) the rate of externally emitted photons can be calculated:

$$P = \int_0^x E_{appl}(x)F(x)\tau_r S(x)\mathrm{d}x \tag{5.33}$$

the external quantum efficiency (externally detected photons per input carrier) is given by:

$$\eta_q = P/(J_n + J_p) \tag{5.34}$$

or in terms of the individual efficiency components:

$$\eta_q = r_{st}\eta_R\eta_{PL}p_{decay} \tag{5.35}$$

where η_R is the recombinative efficiency (also known as the charge efficiency) defined in Chapter 2.

5.5 Analytical solutions

In general it is not possible to solve Equation 5.31 analytically, due to factors such as non-analytic singlet generation rates. However by assuming exciton diffusion is negligible the singlet density at a point can be taken as directly proportional to the singlet generation rate:

$$\tau_s.S = r_{st}R_{opt} \tag{5.36}$$

substituting Equation 5.30 into Equation 5.36 gives:

$$S = \frac{r_{st} R_{opt}}{\tau_{nr} + F\tau_r} \tag{5.37}$$

the total number of radiative events per second, P_{tot}, is given by multiplying the singlet density by the radiative decay rate:

$$P_{tot} = \frac{r_{st} R_{opt}}{\tau_{nr} + F\tau_r} F\tau_r \tag{5.38}$$

the number of radiative events emitted into free-space (out-coupled) can then be expressed as:

$$P = \frac{\tau_{nr} + \tau_r}{\tau_{nr} + F\tau_r} \frac{r_{st} R_{opt}}{\tau_{nr} + F\tau_r} F\tau_r \int_0^{k_+^2} K(\kappa) \mathrm{d}\kappa^2 \tag{5.39}$$

for dipole transitions dominated by radiative decay ($\tau_r >> \tau_{nr}$) Equation 5.39 becomes:

$$P = \frac{r_{st} R_{opt}}{F} \int_0^{k_+^2} K(\kappa) \mathrm{d}\kappa^2 \tag{5.40}$$

for dipole transitions dominated by non-radiative decay ($\tau_{nr} >> \tau_r$) Equation 5.39 becomes:

$$P = \frac{r_{st} R_{opt} F\tau_r}{\tau_{nr}} \int_0^{k_+^2} K(\kappa) \mathrm{d}\kappa^2 \tag{5.41}$$

Equations 5.40 and 5.41 highlight the dual nature of the parameter F; For dominant radiative decay the photometric efficiency is inversely proportional to F, while for dominant non-radiative decay the efficiency is directly proportional to F. This relationship is due to F being related to both the extent of decay into evanescent modes and alterations in the radiative decay rate. Thus for a system with both radiative and non-radiative decay channels, the effect of increasing F is a trade-off between decreased efficiency due to evanescent modes and increased efficiency due to a greater proportion of singlets which emit photons. If radiative

decay dominates (i.e. nearly all singlets emit photons) increasing F must decrease the efficiency since the number of singlets emitting photons is already at a maximum. If non radiative decay dominates (virtually no singlets emit photons) then the increased probability of an evanescent mode being emitted is more than out-weighed by the increase in singlets decaying radiatively.

5.6 Conclusions

This chapter describes alteration in a dipoles emission due to microcavity effects. The key parameters obtained from the optical model are the increase in radiative decay rate and the photon outcoupling, F and $E_{coupling}$, from which the photoluminescent efficiency can be calculated. The drift-diffusion and optical models are linked via the singlet diffusion equation, which is solved by the same numerical techniques discussed in Chapter 3.

References

[1] D. M. Whittaker and I. S. Culshaw, "Scattering-matrix treatment of patterned multilayer photonic structures", *Phys. Rev. B*, **60**, 2610 (1999).

[2] V. Bulovic, V. B. Khalfin, G. Gu, P. E. Burrows, D. Z. Garbuzov and S. R. Forrest, "Weak microcavity effects in organic light-emitting devices", *Phys. Rev. B*, **58**, 3730 (1998).

[3] S. Saito, T Tsutsui, M. Erra, N. Takada, C. Adachi, Y. Hamada and T. Wakimoto, "Progress in organic multilayer electroluminescent devices", *S.P.I.E. Proc.*, **1910**, 212 (1993).

[4] J. Grüner, F. Cacialli and R. H. Friend, "Emission enhancement in single-layer conjugated polymer microcavities", *J. Appl. Phys.*, **80**, 207 (1996).

[5] K. A. Neyts , "Simulation of light emission from thin-film microcavities", *J. Opt. Soc. Am. A* **15**, 962 (1998).

[6] W. Lukosz and R. E. Kunz, "Light emission by magnetic and electric dipoles close to a plane surface", *J. Opt. Soc. Am.* **67**, 1607 (1977).

[7] W. Lukosz and R.E. Kunz,"Changes in fluorescence life-times induced by variation of the radiating molecules' optical environment", *Opt. Comm.* **31**, 42 (1979).

[8] W. Lukosz, "Theory of optical-environment-dependent spontaneous-emission rates for emitters in thin layers", *Phys. Rev. B* **22**, 3030 (1980).

[9] W. Lukosz, "Light emission by multipole sources in thin layers", *J. Opt. Soc. Am.* **74**, 744 (1981).

Chapter 6

Optical and Electro-optical Device Simulation

The results in this chapter were obtained using both the stand-alone optical model and the full electro-optical simulation. When looking for OLED's to study electro-optically, it was preferable to look for devices configurations that the drift-diffusion model had previously simulated successfully (such as bilayer TPD:Alq devices) since this would make it easier to isolate any problems or irregularities arising from combining the separate electrical and optical models.

6.1 Reflection and absorbtion at a metal-semiconductor interface

Perhaps the simplest optical system is that of the interface between two half-infinite media. Figure 6.1 illustrates a system of this type: A dipole (assumed to be of random orientation) is located within an organic semiconductor at a distance x from the metal-semiconductor interface. Light emitted by the dipole can either be directly emitted into the organic, reflected into the organic at the interface or absorbed by the metal.

The dipole's emission was simulated for with two different metal-semiconductor

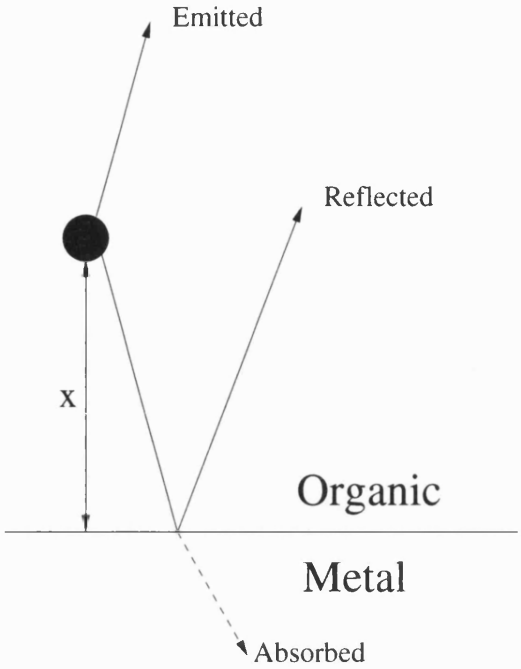

Figure 6.1: Dipole emission near a metal-semiconductor interface

interfaces: The metal was modelled firstly as calcium and then as aluminium. Table 6.1 lists the refractive indices used in the simulation. The dipole was taken to be a monochromatic emitter at a wavelength of 460nm.

Material	n
Organic	1.77
Ca	0.3+1.86i
Al	0.56+6.5i

Table 6.1: Refractive index values used in the optical simulation.

Figure 6.2 shows the increase in the dipole's radiative decay for both systems. As the dipole approaches the metal the total radiative power,F, begins to increase in a exponential fashion, indicating a strong coupling into evanescent modes. For the calcium-organic interface, F begins to increase rapidly once the dipole is within ~50nm of the interface, while this distance is reduced to ~10nm for the aluminium-organic interface. Since a dipole's emissive efficiency generally has a reciprocal relationship to F and bearing in mind the typical layer thicknesses in an OLED (<100nm) the above results imply that, from an optical perspective, an aluminium electrode is preferable to a calcium electrode. This conclusion is agreement with other comparisons made between Ca/Al layers [1].

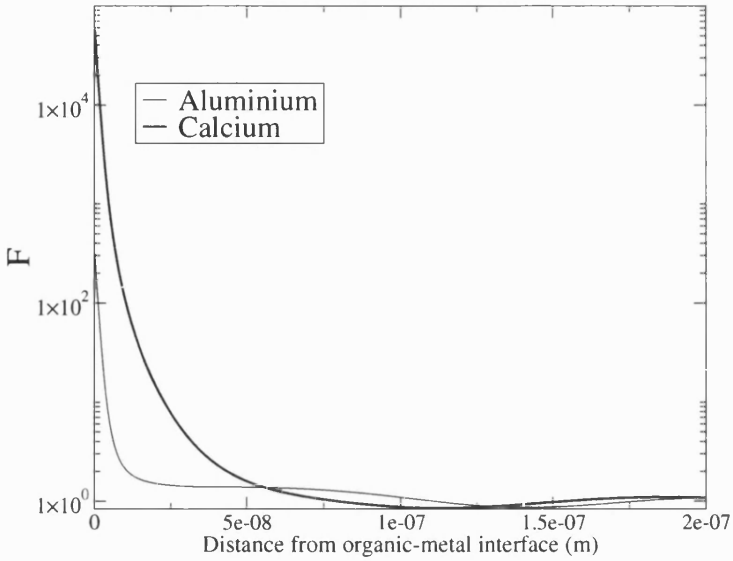

Figure 6.2: Increases in radiative decay near an organic-metal interface.

Figure 6.3 shows the out-coupling efficiencies (the percentage of dipole transitions that result in photons being emitted into upper half space) for calcium and aluminium layers. The photo-luminescent (PL) efficiency was varied from 100% (all dipoles decay radiatively) to 50% (half the dipoles decay radiatively in free space) down to ~0% (dipole transitions are dominated by non-radiative processes). For the ~0% PL results, the out-coupling efficiency is determined by interference effects, which produces a sinusoidal curve that tends to unity (complete reflection) as the dipole moves away from the interface.

For both metals, as the PL efficiency of the dipole increases the out-coupling efficiency is increasingly dependent on F, causing the curves to become less sinusoidal due to comparatively reduced interference effects. For the 50% and 100% PL curves the out-coupling efficiency decreases as the dipole approaches the interface, due to the increased emission into evanescent modes.

As suggested by Figure 6.2 dipoles within ~50nm of the calcium interface have lower out-coupling efficiencies compared to the aluminium interface (for the 50% and 100% PL cases). This again supports the conclusion that, optically speaking, it is preferable to use aluminium electrodes in a thin-film device.

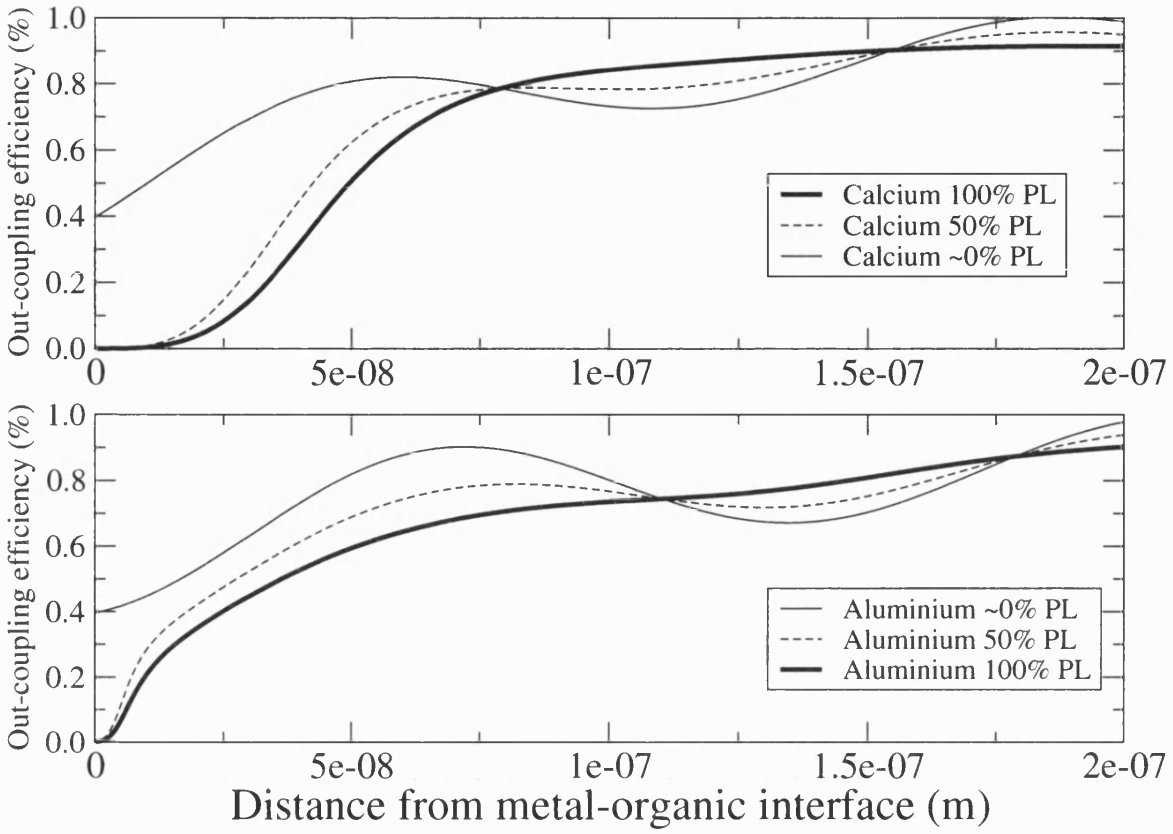

Figure 6.3: Variation in out-coupling efficiency for different organic-metal interfaces.

6.2 The external quantum efficiency of TPD/Alq Bilayer OLEDs

A variation in the external quantum efficiency with layer thickness for bilayer devices constructed of N,N'-diphenyl-N,N'-(3- methylphenyl)-[1,1'biphenyl]-4,4'-diamine (TPD) and tris-(8-hydroxyquinoline) aluminium (Alq) layers has been noted by a number of groups [2, 3]. They each independently concluded that there was an optimum thickness for the Alq layer for which maximum external quantum efficiency was observed.

These devices had previously been studied with the group's electrical model [4].

However the simulation predicted an invariant recombinative efficiency (which is proportional to external quantum efficiency) with respect to Alq thickness. It was concluded that optical effects were responsible for the experimentally observed variations, which made these devices ideal candidates for testing the full electro-optical simulation.

The first set of devices to be simulated were based on those produced by Yahiro et al [5]. The devices studied were fabricated from a 50nm layer of TPD and an Alq layer of variable length, with an Indium-Tin Oxide (ITO) anode and a Mg:Ag cathode [5]. Measurements of external quantum efficiency were carried out at a constant current of 10mAm^{-2}. Figures 6.4 and 6.5 show a schematic energy level diagram and microcavity structure for these devices using parameters from [3, 6, 7, 12, 13, 14, 15, 16]. Tables 6.2 and 6.3 contain the material parameters used in the electrical and optical simulations.

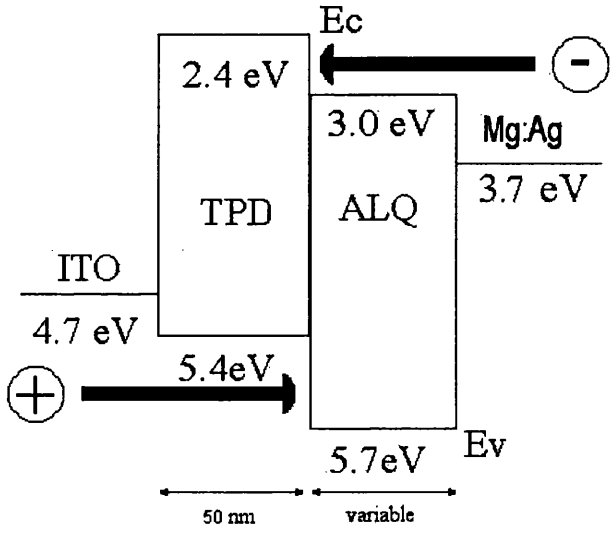

Figure 6.4: Band diagram and direction of charge injection.

The thicknesses of the glass substrate and ITO layers were not stated in [5]. As an initial approximation, the glass layer was assumed to be the same thickness as the largest Alq layer (200nm), while the ITO layer was taken as having half this value. There is some uncertainty about Alq's exciton diffusion length with estimates ranging from 5nm to 50nm [8, 9]. A typical exciton diffusion length in an organic semiconductor is 10nm [10] and this was the value used for the first set of results.

Alq was assumed to be a monochromatic emitter with a wavelength of 550nm [11]. Exciton formation and light emission in the TPD layer were found to be

Parameter	TPD	Alq_3
ϵ_s	3.0 [12]	3.0 [12]
μ_{n0} ($m^2V^{-1}s^{-1}$)	6.1×10^{-10} [12]	1.9×10^{-10} [12]
μ_{p0} ($m^2V^{-1}s^{-1}$)	6.1×10^{-8} [12]	1.9×10^{-12} [12]
E_0 (Vm^{-1})	4.44×10^{7} [12]	7.1×10^{6} [12]
N_C (m^{-3})	1×10^{27} [12]	1×10^{27} [13]
N_V (m^{-3})	1×10^{27} [12]	1×10^{27} [13]
N_{dop} (m^{-3})	-1×10^{15}	1×10^{15}
E_g (eV)	3.0 [6]	2.7 [6]
χ_c (eV)	2.4 [6]	3.0 [6]
L_D (nm)	10	10
η_{PL}	0.33	0.33 [14]
r_{st}	0.25	0.25 [9]
τ_s (s^{-1})	7.7×10^{7}	7.7×10^{7} [15]
E_t (eV)	-	0.15 [16]
N_t (m^{-3})	-	1.3×10^{23} [16]
ϕ_{Bp} (eV)	0.70	-
ϕ_{Bn} (eV)	-	0.66

Table 6.2: Material parameters used in the electric transport simulation.

Material	n	layer width (nm)
Air	1.0	
Glass	1.5 [9]	200
ITO	1.9 [9]	100
TPD	1.9 [9]	50
Alq	1.7 [9]	25-200
Mg:Ag	0.25+4.3i [9]	

Table 6.3: Refractive index values and layer widths used in the optical simulation.

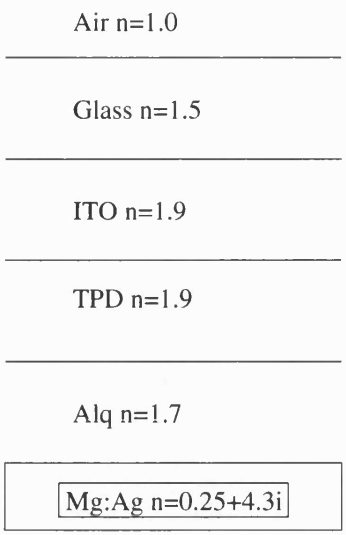

Figure 6.5: Schematic of the device's microcavity structure.

at most 1% of that in the Alq layer. Because of this the following results only consider emission arising from the Alq layer, to simplify the data analysis.

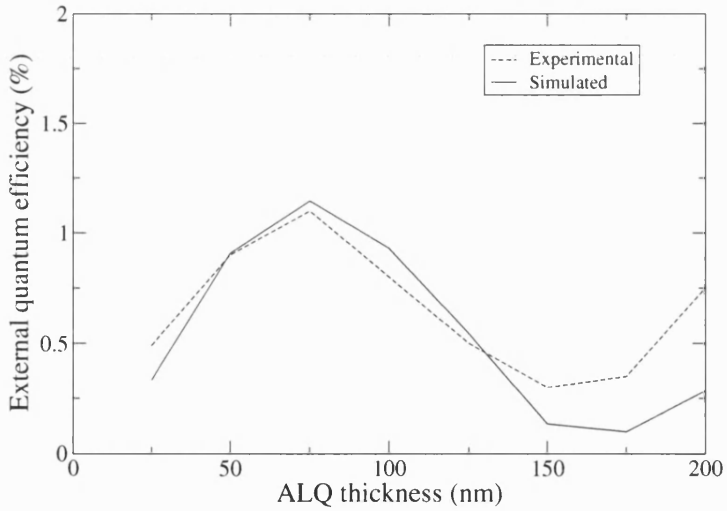

Figure 6.6: The external quantum efficiency versus Alq thickness for a series of ITO\TPD\Alq\Mg devices.

Figure 6.6 shows the simulated and experimentally measured external quantum efficiencies for the devices described above. Overall there is a good agreement be-

tween the simulated and experimental curves. The simulated quantum efficiencies are the same order of magnitude as the experimental measurements, additionally a clear variation in efficiency, from a maximum to a minimum, between Alq layer thickness of about 75nm and 175nm, is present in both cases.

The efficiency peak at an Alq thickness of 75nm is due to an interaction between the twin optical effects of constructive interference and alterations to the exciton radiative decay rate. This means that exciton decay is more likely to result in externally detected photons at the 75nm than at other thicknesses. Relating this to the optical model Eq 5.26 reaches a maximum value at an Alq thickness of 75nm. The efficiency minimum at $\sim$ 175nm has a similar explanation, except now destructive interference and the balance between non-radiative and radiative decay act to reduce the number of emitted photons and hence reduce the efficiency.

The closest match is for Alq layer widths in the region 25nm to 125 nm. For thicker layers, although the variation is similar, the simulated magnitudes are lower than in the experimental data. A possible explanation for this discrepancy is as follows; As the Alq layer width increases, the distance between the emission zone and the Mg:Ag interface also increases, so that the variation in emission due to altered exciton lifetime (which is mainly due to the close proximity of the Mg:Ag surface) is reduced. Because of this, the wave-guiding effects (which are dependent on each layer between the emissive layer and free space) become relatively more significant. Since the lengths of the glass and ITO layers were not known and the assumed values could be inaccurate, this is likely to lead to discrepancies between theory and experiment for the devices with thicker Alq layers. Equally, for the shorter Alq thickness devices, the device's emission rate, and hence quantum efficiency, is relatively less dependent on lengths of the glass/ITO layers, allowing a more accurate calculation of the quantum efficiency.

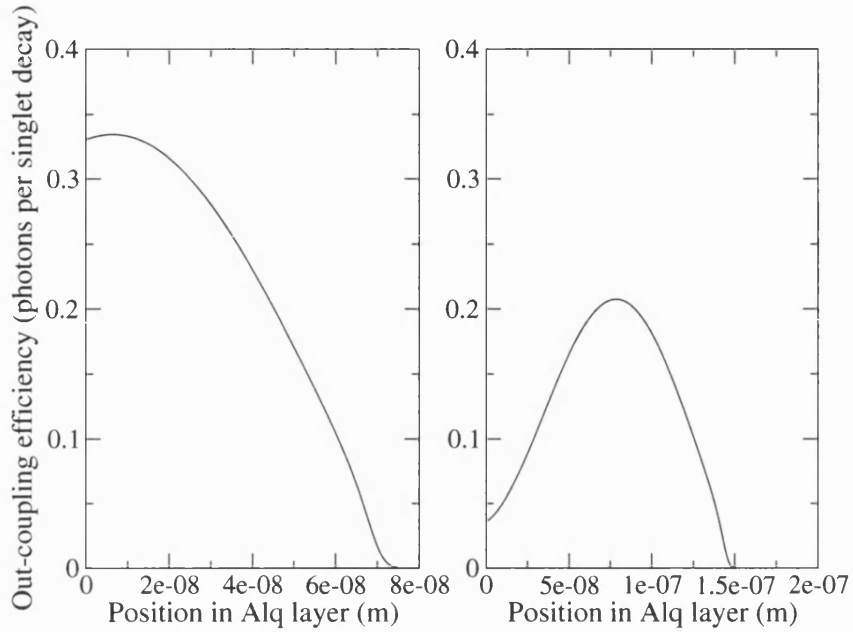

Figure 6.7: The out-coupling efficiencies for Alq thicknesses of 75nm (left) and 150nm(right)

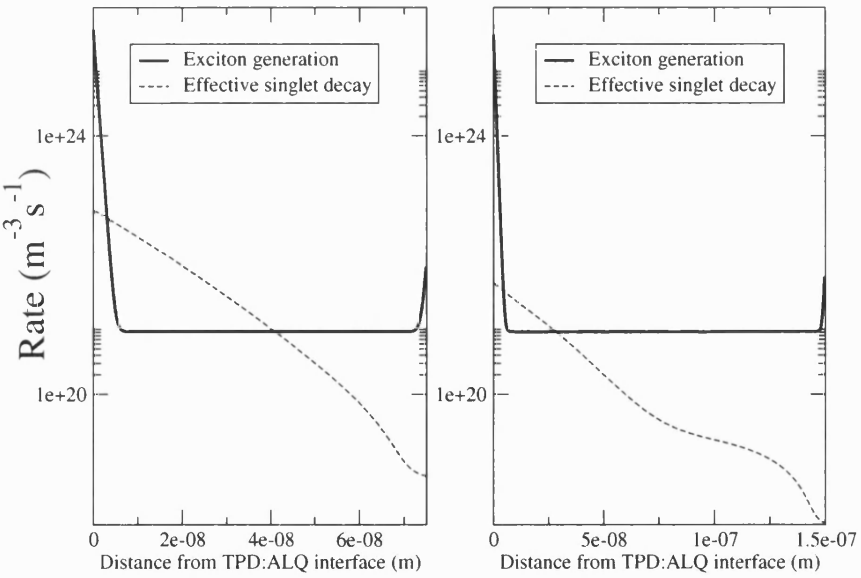

Figure 6.8: Singlet generation and out-coupled decay profiles for Alq thicknesses of 75nm (left) and 150nm(right)

Figures 6.7 and 6.8, show the outcoupling efficiencies, singlet generation (Langevin recombination) and effective (out-coupled) decay rate-densities for Alq thicknesses of 75nm and 150nm. In both cases the peak formation/decay rates occur at a different positions to the peak out-coupling efficiency, although this is more pronounced in the 150nm device. For the region near the cathode (on the right of the graph) the out-coupling efficiency is negligible, hence the decay rate is low despite the secondary singlet generation peak. Comparing singlet decay to generation rates, the decay rate-densities are much smoother, due to generated singlets diffusing before they decay.

6.2.1 The influence of Schottky barrier height on external quantum efficiency

The magnitude of the external quantum efficiency proved to be highly sensitive to the values of the injection barriers, ϕ_{Bp} and ϕ_{Bn}. Figure 6.9 shows the variation in eqe with Alq layer thickness for devices with values of $\phi_{B}n$ from 0.7 to 0.62. All other parameters were as in Tables 6.2 and 6.3.

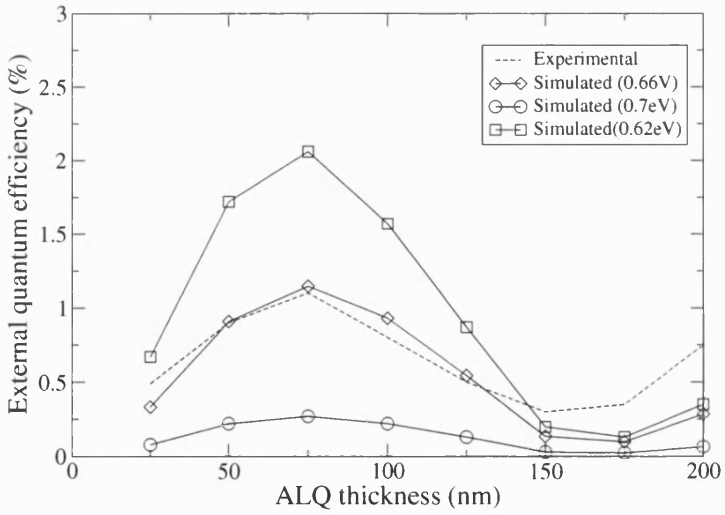

Figure 6.9: The external quantum efficiency versus Alq thickness for a series of ITO\TPD\Alq\Mg devices.

Changing the barrier height did not noticeably affect the positions of the simulated efficiency maxima/minima (75nm and 175nm for all simulations). However the peak-to-trough ratios and peak magnitudes were dependent on the barrier height. As ϕ_{bn} decreases from 0.7ev the efficiency increases, which is presumably due to the charge efficiency increasing in Equation 5.35 . Decreasing the electron injection barrier increases the number of injected electrons and so increases the electron to hole ratio. It is important to note that decreasing the electron barrier will only increase the charge efficiency up to a point: Once the ratio of injected electrons to holes reaches 1:1, injecting proportionally more electrons into the system will necessarily reduce the charge efficiency.

6.2.2 The influence of exciton diffusion length on external quantum efficiency

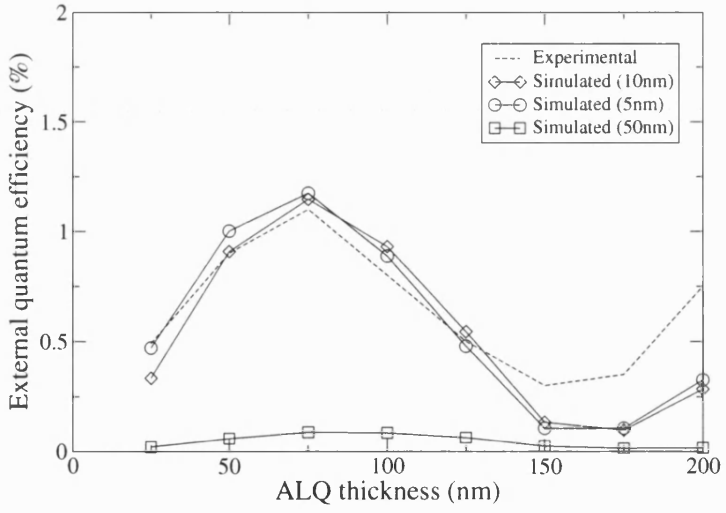

Figure 6.10: The external quantum efficiency versus Alq thickness for a series of ITO\TPD\Alq\Mg devices.

Experimental estimates of the singlet diffusion length in Alq vary by roughly 1 order of magnitude, as mentioned at the start of the section. Figure 6.10 shows the variation in eqe with Alq layer thickness for devices with values of L_D covering

the range of experimental measurements, including the "typical" value of 10nm, and the experimental data. All other parameters were as in Tables 6.2 and 6.3.

There is little difference between the 5nm and 10nm results, however the eqe's are greatly reduced when the diffusion length is set to 50nm. Since the majority of singlets are generated at the TPD:Alq interface, and the out-coupling efficiency is decreased for singlets close to the Alq:Mg:Ag interface, increasing the diffusion length will result in an increased displacement of singlets through the system and, if the displacement is wide enough, reduced optical efficiency.

6.2.3 The influence of cathode material on external quantum efficiency

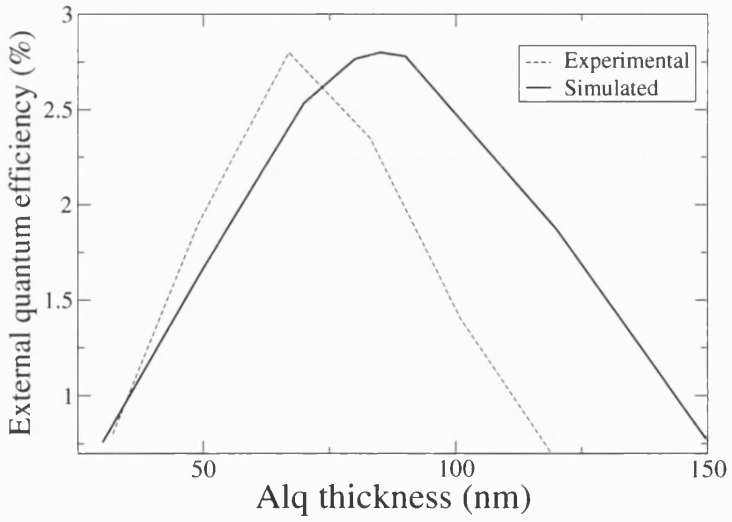

Figure 6.11: The external quantum efficiency versus Alq thickness for a series of ITO\TPD\Alq\Al devices.

The next set of devices to be simulated were based on those studied by Schmitz [17] et al. These devices were essentially the same design as [5] with the exception that the TPD layer was 40nm thick and an Al electrode was used instead of Mg:Ag. Because of this similarity the parameters from Tables 6.2 and 6.3 were

Parameter	value)
ϕ_{bn} (eV)	1.2
TPD thickness (nm)	40
Al refractive index	0.5+6.5i

Table 6.4: Updated simulation parameters.

re-used. The only changes made were to the TPD thickness, ϕ_{bn} and cathode refractive index. Table 6.4 lists the pertinent values.

The results in [17] gave the photometric efficiency in arbitrary units. To allow for a comparison with the simulation, the experimental results were scaled such that the peak magnitudes of both curves were equal. Figure 6.11 shows the simulated and scaled experimental curves.

As with the results in Figure 6.6 the simulation agrees better with the experiment data for lower Alq thicknesses. The experimental peak efficiency occurs at $\sim$ 70nm while the simulated peak occurs at $\sim$ 85nm, additionally the simulated external quantum efficiency decreases less steeply than the experimental curve at larger thicknesses. This discrepancy could be caused by one of the input parameters being fitted or estimated incorrectly (as for Figure 6.6). In particular there is still some uncertainty as to the value of Alq's exciton diffusion length (as the results from Section 6.2.2 demonstrated) which can effect the location of the peak thickness.

6.3 Glare reduction via destructive interference

A common problem in the design of display devices is that of glare; ambient light being reflected from the screen. Figure 6.12 illustrates how glare can reduce the contrast between an OLED's on(active) and off states. Ambient light enters through the transparent ITO anode and is reflected back by the reflective Al cathode. Since an observer views a superposition of the internally emitted and ambient reflected light, then the contrast of a display (emitting at constant luminance) can vary according to environmental conditions. To comfortably view a monochrome display the minimum luminance required is $\sim$20% of any ambient reflections, while this increases to $\sim$900% for a full-colour display [18]. Thus

effective anti-glare techniques are required to manufacture usable full-colour displays.

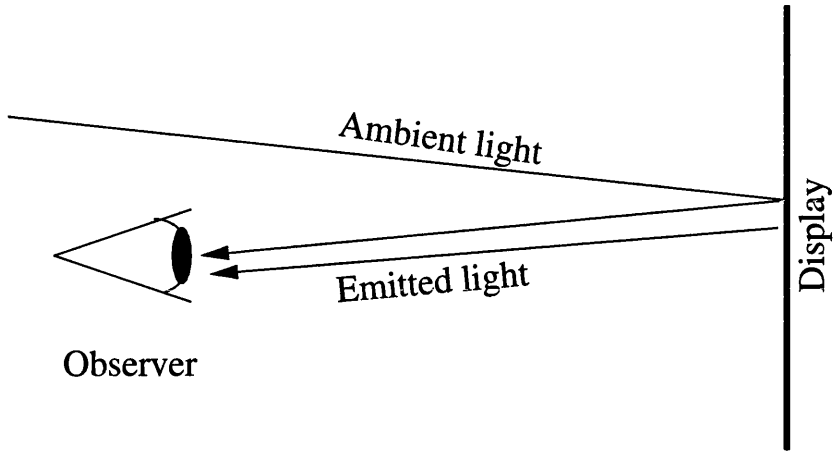

Figure 6.12: Reflected and emitted light from a display

One method of removing glare is to incorporate a circular polariser into the device's structure. This is very effective at eliminating ambient reflections and can produce a "black" off state. However for devices that emit unpolarised light, roughly 50% of emitted light will be lost to the polariser.

There are alternative glare-removal techniques (e.g [19]) which use destructive interference to eliminate ambient reflections. These techniques generally require extra layers to be incorporated into the device structure.

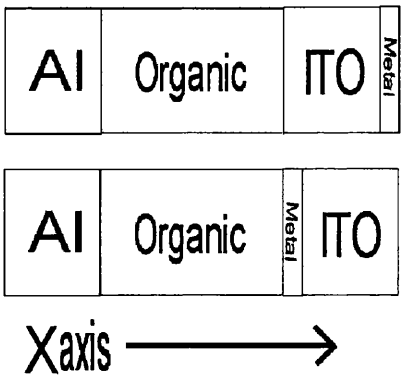

Figure 6.13: Possible device structures including a thin metal layer

It was decided to investigate how adding a thin-metal anti-glare layer affects an OLEDs optical properties. Figure 6.13 shows the possible locations where a thin metal layer could be introduced into a device. There were two options for the

Device	Structure
1	Glass/ITO(150nm)/Al(4.5nm)/Organic(variable)/Al
2	Glass/Al(4.5nm)/ITO(150nm)/Organic(variable)/Al
3	Glass/ITO(130nm)/Cr(4.5nm)/Organic(variable)/Al
4	Glass/Cr(4.5nm)/ITO(130nm)/Organic(variable)/Al
5	Glass/ITO(150nm)/Organic(variable)/Al

Table 6.5: Device composition (from [20])

metal: Chromium and Aluminium. Table 6.5 lists the relevant structures, along with a control device that has no thin-metal layer.

Figures 6.14-6.18 show the positional variation of F and $E_{coupling}$ within an organic layer against increasing layer thickness. Both axes are scaled, with the y-axis corresponding to the dipole's distance from the cathode divided by the organic's thickness, while the x-axis is scaled such that a relative thickness of 1 corresponds to a thickness of 236nm. Table 6.5 lists the structures that were modelled, while Table 6.7 lists the simulation parameters. Simulations were performed for dipoles emitting monochromatically at 550nm.

The $E_{coupling}$ plots share a common feature, of a peak contour that curves down as the relative thickness is increased. The peak plane wave out-coupling occurs at roughly the center of a device with a relative thickness of 0.5. For Devices 2,3,4 adding the thin-metal layer does not noticeably increase the peak out-coupling, which actually decreases for Devices 3 and 4. However for Device 1 the peak-outcoupling is increased to a value of 0.7. This suggests that Device 1 could be an efficient structure.

The plots of F display peak values at one or both edges depending on the position of the thin metal layer. These results highlight a potential problem with device 1: As the organic layer is sandwiched between two metal layers, exciton decay close to the metal/organic interfaces (as would be observed in a single-layer device) would be inefficient due to quenching. To fully exploit the out-coupling maximum in Device's 1 structure it might be necessary to employ a bilayer organic configuration (such as TPD:Alq) as this would allow the singlet generation peak to be co-incident with the out-coupling peak.

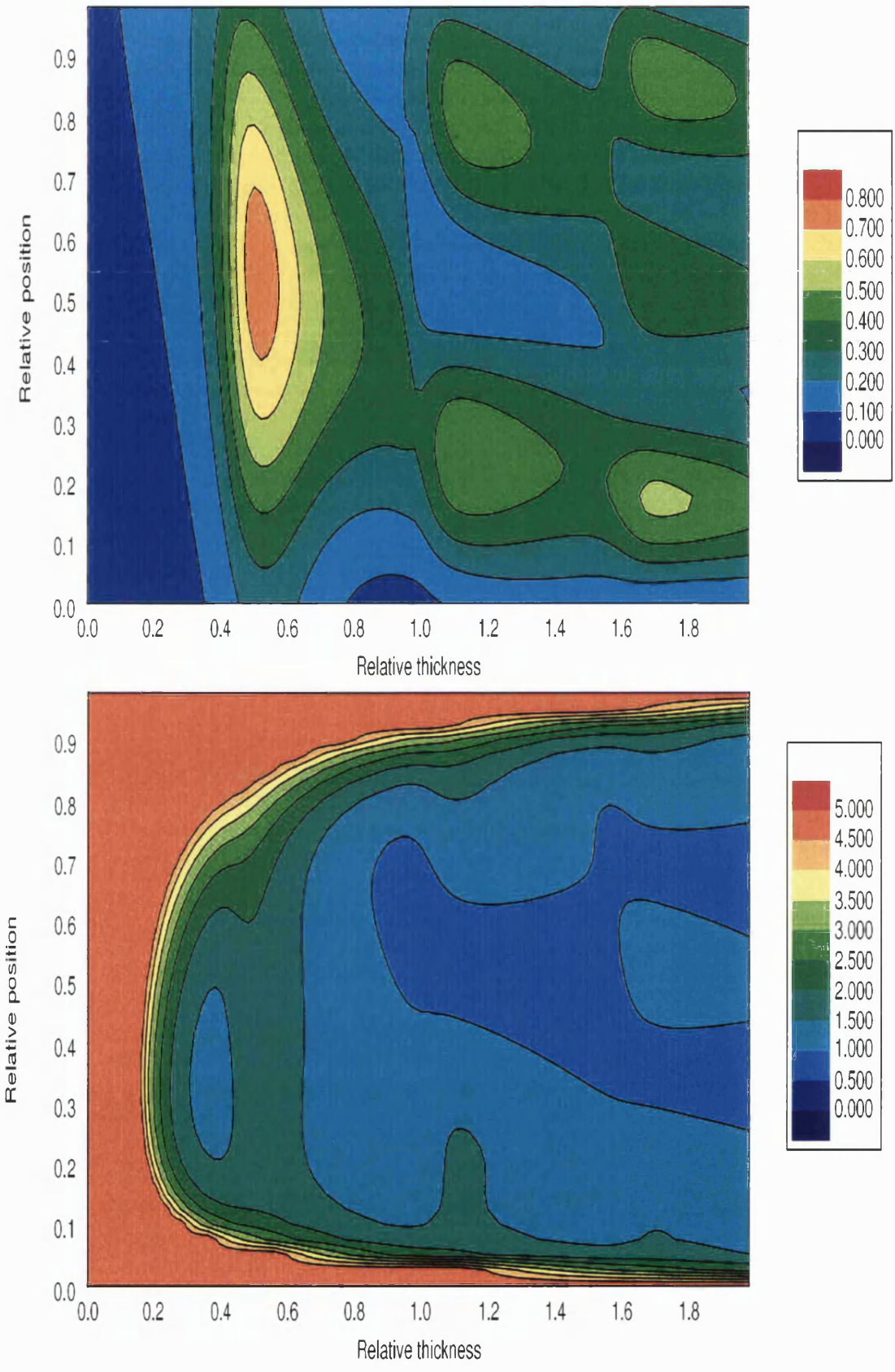

Figure 6.14: $E_{coupling}$ (top) and F (bottom) for Device 1.

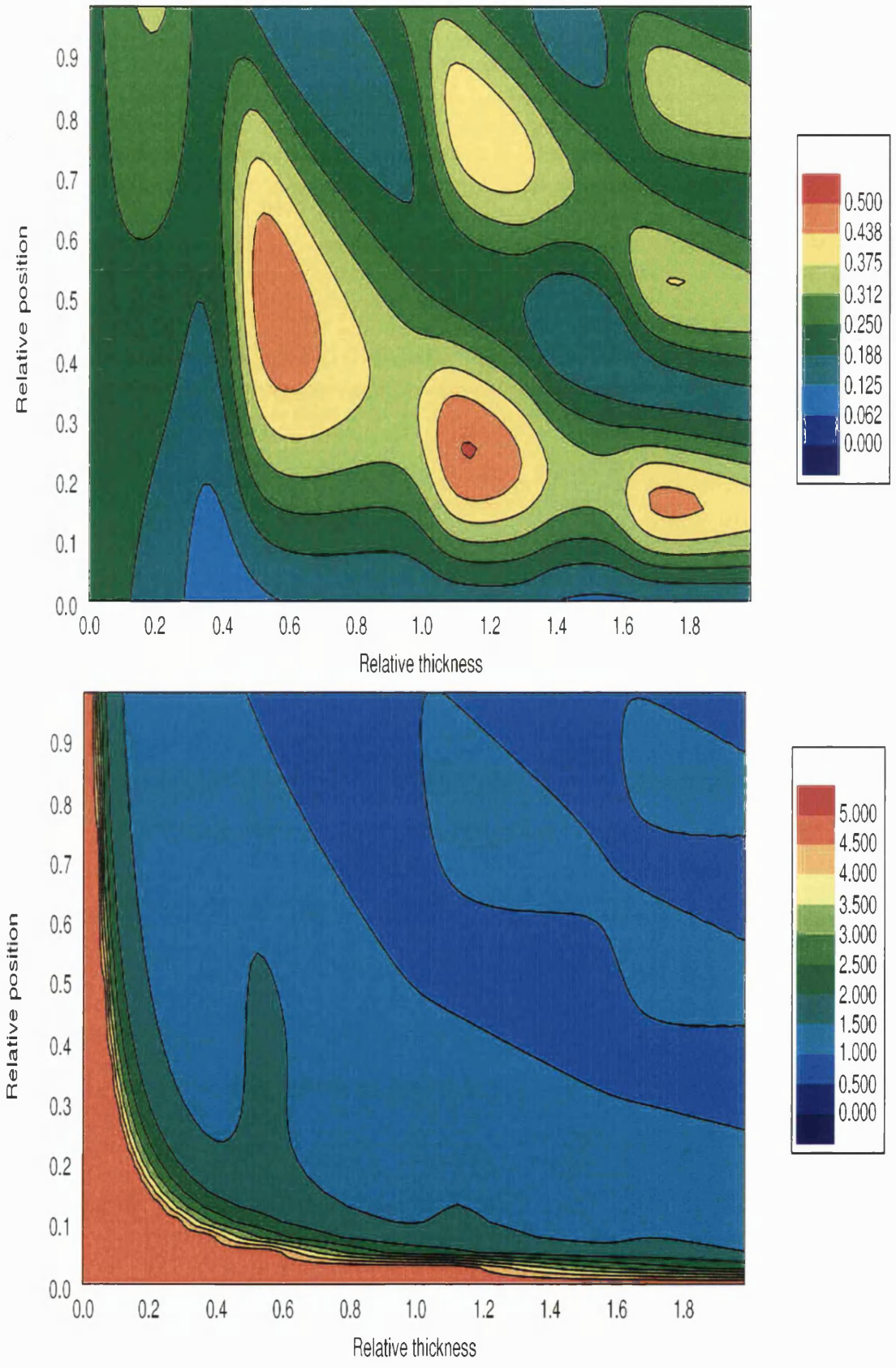

Figure 6.15: $E_{coupling}$ (top) and F (bottom) for Device 2.

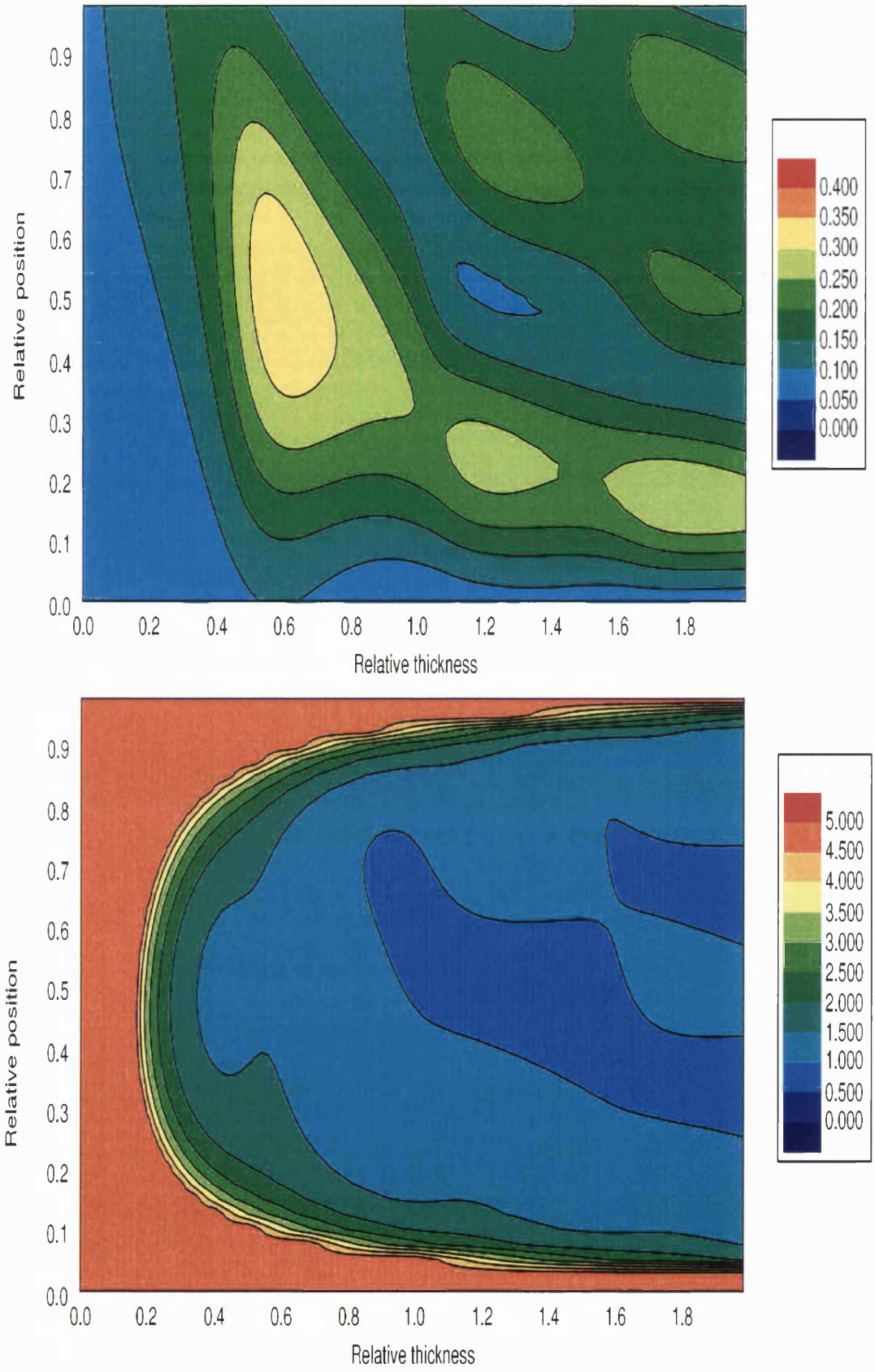

Figure 6.16: $E_{coupling}$ (top) and F (bottom) for Device 3.

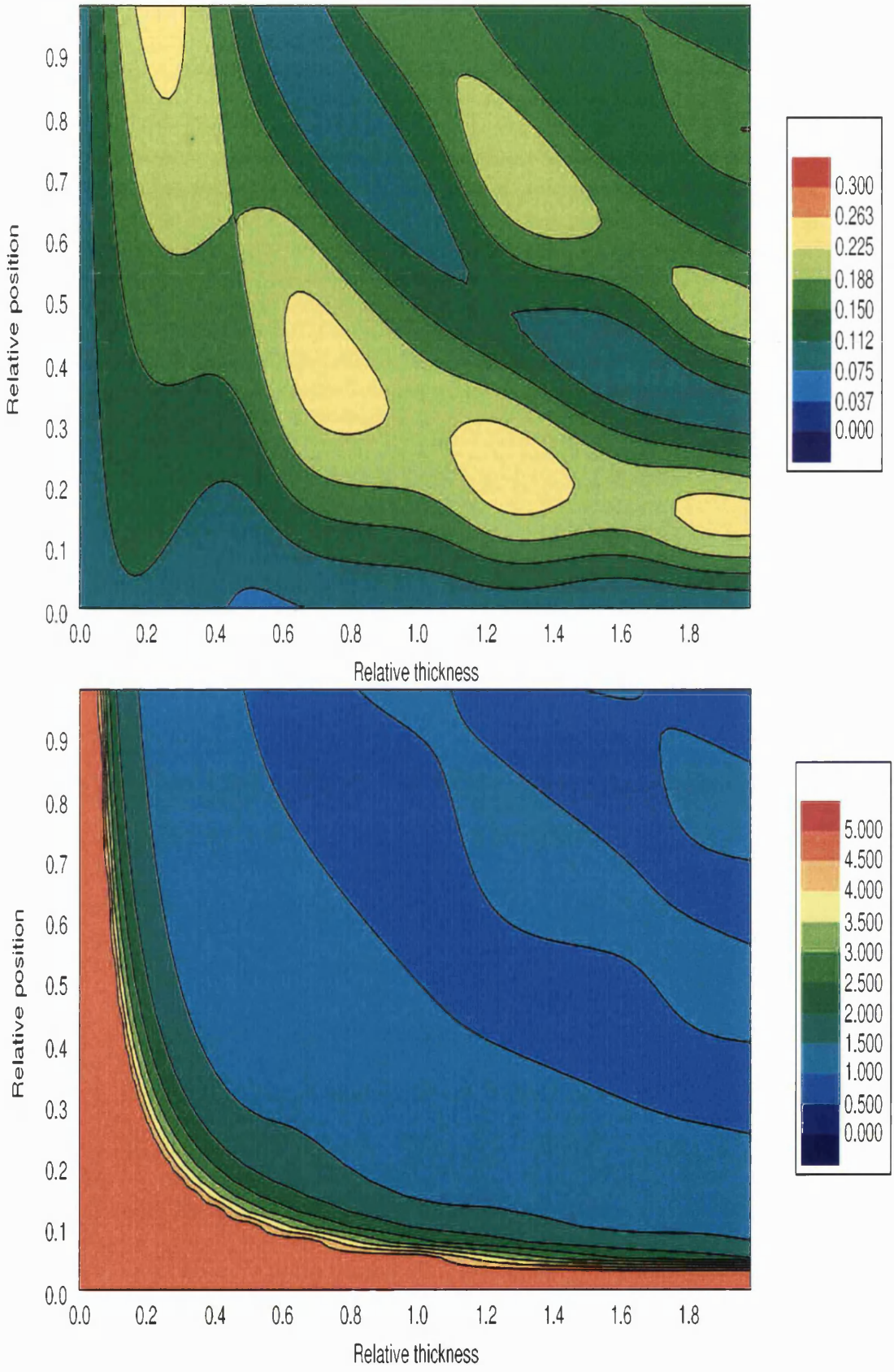

Figure 6.17: $E_{coupling}$ (top) and F (bottom) for Device 4.

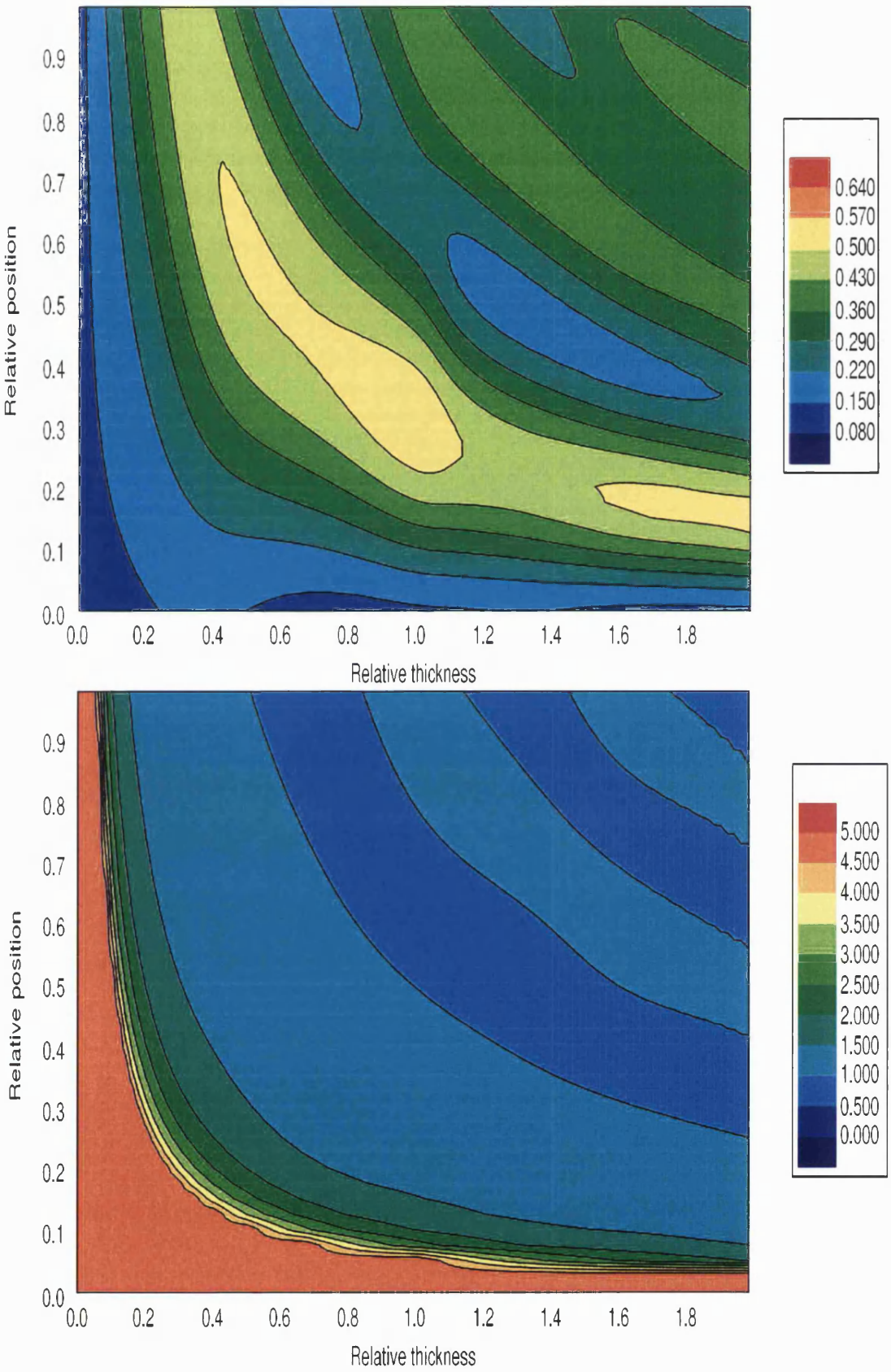

Figure 6.18: $E_{coupling}$ (top) and F (bottom) for Device 5.

[11] V. Cleave, G. Yahioglu, P. Le Barny, R. H. Friend and N. Tessler, "Harvesting singlet and triplet energy in polymer LEDs", *Adv. Mat.*, **11**, 285 (1999)

[12] J-S. Kim, P. K. H. Ho, N. C. Greenham and R. H. Friend, "Electroluminescence emission pattern of organic light-emitting diodes: Implications for device efficiency calculations" , *J. Appl. Phys.*, **88**, 1073 (2000)

Parameter	Value
ϵ_s	3.0
μ_{n0} ($m^2V^{-1}s^{-1}$)	5.0×10^{-12}
μ_{p0} ($m^2V^{-1}s^{-1}$)	1.0×10^{-10}
E_0 (Vm^{-1})	1.0×10^{7}
N_C (m^{-3})	1×10^{27}
N_V (m^{-3})	1×10^{27}
N_{dop} (m^{-3})	-1×10^{12}
E_g (eV)	2.4
χ_c (eV)	2.05
L_D (nm)	10
η_{PL}	0.33
r_{st}	0.25
τ_s (s^{-1})	7.7×10^{7}
E_t (eV)	-
N_t (m^{-3})	-
ϕ_{Bp} (eV)	0.2
ϕ_{Bn} (eV)	0.2

Table 6.6: Material parameters used in the electric transport simulation.

Material	n
Glass	1.5 [20]
ITO	1.8 [20]
Organic	1.8 [20]
Al	0.86+6.38i [20]
Cr	3.0+4.6i [20]

Table 6.7: Refractive index values used in the optical simulation.

To study the effect of a thin metal layer on luminance the devices were simulated using the full electro-optical model. Tables 6.6, 6.7 and 6.8 list the parameters used in the simulation. The organic was treated as having electrical properties similar to PPV, although the electron and hole Schottky barriers were set artificially to 0.2eV each (although in practice placing a thin metal layer next to a semiconductor can alter injection barriers [19]). For each device the organic thickness was set according to [20] for optimal destructive interference of ambient light. The organic semiconductors were again assumed to be mono-chromatic emitters at 550nm-PPV's free-space peak wavelength[21]. Figure 6.19 shows the photon density-voltage curves obtained with these parameters.

For Devices 1-4 including thin-metal layers reduces the luminance (which is pro-

Device	Organic Thickness
1	Organic(108nm)
2	Organic(110nm)
3	Organic(85nm)
4	Organic(110nm)
5	Organic(108nm)

Table 6.8: Device composition from [20])

portional to photon density) curves by ~30% to ~60% (compared to the results for Device 5). Devices 2,3 and 4 have roughly similar luminance characteristics while Device 1's luminance is noticeably higher. It should be noted that the results do not account for ambient light sources and although Device 1's luminance is ~30% less than that of Device 5, it could actually appear brighter (due to an increased contrast) in intense ambient light, due to glare cancellation.

It would be interesting to re-run the simulations with a bilayer organic structure, designed so that the singlet generation and out-coupling peaks are co-incident. Since Device 1 has a greater peak out-coupling value than Device 5, it is entirely possible that Device 1's luminance could exceed that of Device 5, which in conjunction with reduced glare could make Device 1 appear far brighter than Device 5.

6.4 Conclusions

The results in this chapter demonstrate the increased range of phenomena that can be studied with an electro-optical model. Starting with an examination of exciton decay near a metal-semiconductor interface, the model was then used to simulate the external quantum efficiencies of a series of ITO/TPD/Alq/Mg:Ag devices. The simulated results are consistent with experimental measurements for the same set of devices, demonstrating the validity of the model.

The external quantum efficiencies were shown to be sensitive to the Schottky barrier height and exciton diffusion length. By adjusting the Mg:Ag electron injection barrier in small increments, a value of 0.66eV was found to give the best fit to the experimental data. The results obtained by varying the exciton

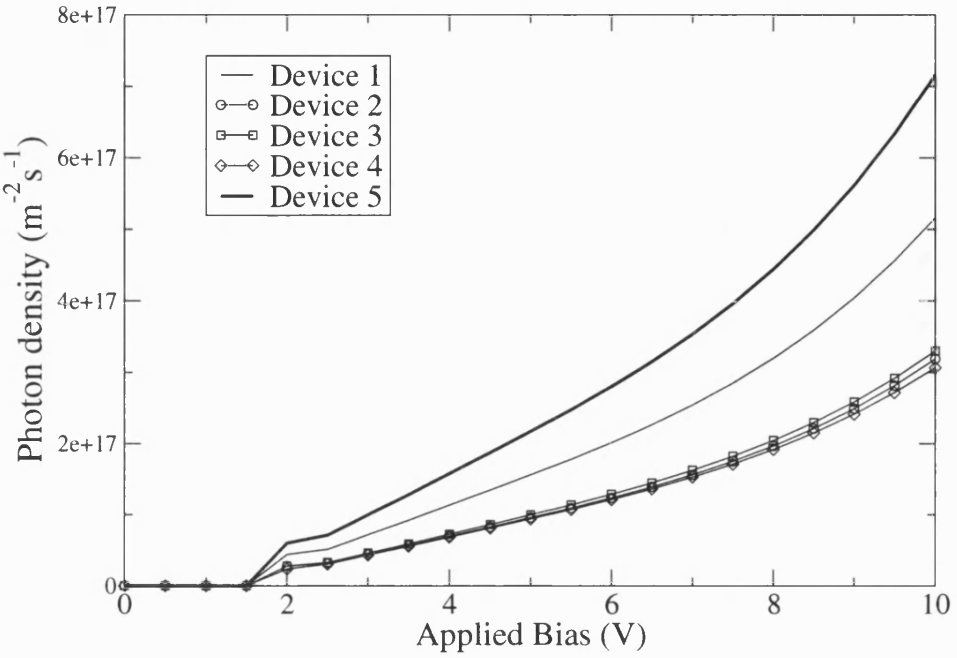

Figure 6.19: Emitted photon densities for Devices 1-5

diffusion length demonstrated that using the largest experimental estimates (of $\sim$ 50nm) produced quantum efficiencies inconsistent with the experimental results. Exciton diffusion lengths between 5nm and 10nm provided the best agreement with experiment.

When thin metal anti-glare filters are introduced into a device structure (Section 6.3) the location and composition of the metal has a noticeable effect on emissive output. By using thin Al layers it is possible to obtain regions in the device with high out-coupling efficiencies, although the device's electrical characteristics must also be considered to fully exploit these regions.

References

[1] C. M. Ramsdale and N. C. Greenham, "The Optical Constants of Emitter and Electrode Materials in Polymer Light-Emitting Diodes", *J. Phys. D: Appl. Phys.*, **36**, 543 (2003).

[2] M. A. Baldo, D. F. O'Brien, M. E. Thompson and S. R. Forrest, "Excitonic singlet-triplet ratio in a semiconducting organic thin film", *Phys. Rev. B*, **60**, 14422 (1999).

[3] V. Bulovic, V. B. Khalfin, G. Gu, P. E. Burrows, D. Z. Garbuzov and S. R. Forrest "Weak microcavity effects in organic light-emitting devices", *Phys. Rev. B* , **58**, 3730 (1998).

[4] S. J. Martin, *PhD Thesis*, University of Bath, (2002)

[5] M. Yahiro and T. Tsutsui, "Influence of Device Configuration on External Quantum Efficiency in Organic Light-Emitting Devices", *Mat. Res. Soc. Symp. Proc.*, **660**, JJ5.27.1 (2001).

[6] S. Berleb, W. Brütting and G. Paasch, "Device physics of organic light-emitting diodes based on thin films", *Org. Electron.*, **1**, 41 (2000)

[7] L. Bozano, S. Carter, .J C. Scott, G. G. Malliaras and P. J .Brock, "Temperature- and field-dependent electron and hole mobilities in polymer light-emitting diodes", *Appl. Phys. Lett.*, **74**, 1132 (1999).

[8] R. Priestley, A.D. Walser, R. Dorsinville, "Temperature dependence of transient photoluminescence in tris 8-hydroxyquinoline aluminum Alq", *Opt. Comm.*, **158** , 93(1998)

[9] P. E. Burrows and S. R. Forrest, "Electroluminescence from trap-limited current transport in vacuum-deposited organic light-emitting devices", *Appl. Phys. Lett.*, **64**, 2285 (1994)

[10] J. J. M. Halls, K. Pichler, R. H. Friend, S. C. Moratti and A. B. Holmes, "Exciton diffusion and dissociation in a poly(p-phenylenevinylene)/C-60 heterojunction photovoltaic cell", *Appl. Phys. Lett.,* **68**, 3120 (1996)

[11] P. E. Burrows, Z. Shen, V. Bulovic, D. M. McCarty, S. R. Forrest, J. A. Cronin and M. E. Thompson, "Relationship between electroluminescence and current transport in organic heterojunction light-emitting devices", *J. Appl. Phys.*, **79**, 7991-8006 (1996)

[12] J Staudigel, M Stößel, F Steuber and J Simmerer, "A quantitative numerical model of multilayer vapor-deposited organic light emitting diodes", *J. Appl. Phys.*, **86**, 3895 (1999)

[13] J. H. Burroughes, D. D. C. Bradley, A. R. Brown, R. N. Marks, K. Mackay, R. H. Friend, P. L. Burns and A. B. Holmes, "Light-emitting diodes based on conjugated polymers", *Nature*, **47**, 539 (1990)

[14] N. C. Greenham, R. H. Friend, and D. D. C. Bradley, "Angular-dependence of the emission from a conjugated polymer light-emitting diode - implications for efficiency calculations", *Adv. Mat* **6**, 491 (1994).

[15] M.E. Thompson, P.E. Burrows, S.R. Forrest, "Electrophosphorescence in organic light emitting diodes", *Curr. Op. Mat. Sci.*, **4**, 369 (1999)

[16] W. Brütting, S. Berleb, and A. G. Mückl, "Device physics of organic light-emitting diodes based on molecular materials" *Org. Elec.*, **2**, 1 (2000)

[17] C. Schmitz, P. Poesch, M. Thelakkat and H.-W. Schmidt, "Combinatorial methods for optimization of materials selection and device parameters in OLEDs" *Phys. Chem. Chem. Phys.*, **1**, 1777 (1999)

[18] ViewPoint Flat Panel Display, Inc, *http://www.viewpointdisplay.com/*, (2003)

[19] A. N. Krasnov, "High-contrast organic light-emitting diodes on flexible substrates", *Appl. Phys. Lett*, **80**, 3853 (2002)

[20] Geraldine Verschoor, *Private Communication* (2002-2003)

[21] R H Friend, R W Gymer, A B Holmes, J H Burroughes, R N Marks, C Taliani, D D C Bradley, D A Dos Santos, J L Brédas, M Löglund, and W R Salaneck, *Nature*, "Electroluminescence in conjugated polymers", **397**, 121 (1999).

Chapter 7

Conclusions and Further Work

The electro-optical simulation, described in this thesis, has shown itself capable of reproducing experimental observations and also of acting in a predictive fashion, for both bulk device behaviour (such as J-V curves) and material characteristics (such as trap densities).

The middle chapters (Chapters 2 to 4) dealt with the drift-diffusion model and included details of improvements and modifications made to the simulation. Section 4.2 presented two different methods for modelling charge transport across an organic heterojunction; Continuous drift-diffusion across the interface and thermionic emission over the heterojunction barrier. In general explicitly including energetic barrier effects caused a small reduction in currents and a small increase in charge densities at the barrier, although these variations did not scale greatly with the magnitude of the barrier. The choice of method to simulate the heterojunction seems relatively less important than accurately determining parameters such as the Schottky barrier heights.

Modelling the blue co-polymer SCB11 (Sections 4.4 and 4.5) posed several challenges in explaining the observations of Reference [1]. Resistive effects (both series and parallel) had to added to the drift-diffusion model to fit the experimental data. In particular, a parallel resistance was essential in reproducing the low forward and reverse bias electric fields and currents.

While the drift-diffusion model can be used for a very approximate study of light-

output (Section 4.3) previous work [2] has concluded that microcavity effects must be considered to accurately simulate properties such as quantum efficiency. The electro-optical model, as detailed in Chapters 5 and 6 was able to reproduce the external quantum efficiency of a series of TPD:Alq devices (Section 6.2). As with the stand-alone drift-diffusion model, the results were particularly sensitive to a few key variables (Schottky barrier height, exciton decay parameters). When fitting was necessary, attempts were made to keep parameter alterations within experimentally measured limits.

The electro-optical model also allows a more in-depth study of sophisticated device structures, such as the anti-glare filters in Section 6.3. While the optical model is able to provide a guide to optimal layer thickness and efficiency, L-V curves are preferable when discriminating between various device configurations.

7.0.1 Further work

The drift-diffusion and optical models are essentially complete, in that they take account of sufficient physical effects to accurately model the majority of one-dimensional systems. However both models could be extended to increase the simulations level of detail.

The linear regions of the SCB11 I-V curves, discussed in Section 4.5, were modelled phenomenologically by incorporating a parallel resistance into the electrical simulation. It was hypothesised that this resistance arose from conduction via trap states within the band-gap. Other groups (e.g. [3]) have also attributed divergences from pure-band injection to conduction via impurity states. Additionally, Monte-Carlo simulations of charge injection from a metal into a disordered hopping system [4] indicate that neither thermionic emission or Fowler-Nordheim tunneling are entirely appropriate to model carrier injection in OLEDs (for reasons such as incorrect temperature dependence). Future modifications to the drift-diffusion simulation could include a more explicit treatment of the effect of impurity states on charge transport and injection [5].

In this thesis, simulations performed with the optical model assumed that the excitons behaved as monochromatic light sources, while in reality an OLED emits over a spectrum of wavelengths. These spectra have been observed to shift de-

pending on whether the organic semiconductor is in a free-space or microcavity configuration [6, 7]. The optical model could be extended to model these effects by calculating quantities such as F and $E_{coupling}$ for an appropriate range of wavelength values. Alterations to an exciton's emission profile due to microcavity effects could then be obtained by multiplying these values by the relative intensities of a reference (free-space) spectrum.

Although it was possible to improve the estimate for Alq's exciton diffusion length from those obtained experimentally, it was perhaps the least well-defined input parameter in Section 6.2. By simulating a wider selection of devices it might be possible to obtain a more precise value for the diffusion length.

The investigation of thin metal anti-glare filters (Section 6.3) could be extended by simulating a wider range of structures. In particular, the nature of the microcavity's out-coupling profile suggests that device efficiency could be increased by employing a bilayer organic configuration, also structures with multiple thin metal layers could be investigated [8]. Additionally an ambient light source could be incorporated into the optical simulation, which would allow a device's contrast to be calculated. Alterations to the Schottky barrier height due to the thin metal layer [9] could be also be included.

There are many other potential applications of the electro-optical model including: Determination of peak operating voltages (by comparing quantum and power efficiencies [10]), radiative triplet decay (for phosphorescent dye-doped systems [11]) or studying angular emission characteristics [12].

References

[1] R. U. A. Khan, *Private Communication* (2002-2003)

[2] S. J. Martin, *PhD Thesis*, University of Bath, (2002)

[3] J. M. Lupton and I. D. W. Samuel, "Temperature-dependent single carrier device model for polymeric light emitting diodes", *J. Phys. D.:Appl. Phys.*, **32**, 2973 (1999).

[4] U. Wolf, V. I. Arkhipov and H. Bässler, "Current injection from a metal to a disordered hopping system. II. Comparison between analytic theory and simulation" , *Phys. Rev. B* , **59**, 7507 (1999)

[5] N. F. Mott and E. A. Davis, *Electronic Processes in Non-Crystalline Materials*, Clarendon Press, Oxford (1971)

[6] R. H. Friend, R. W. Gymer, A. B. Holmes, J. H. Burroughes, R. N. Marks, C. Taliani, D. D. C. Bradley, D. A. Dos Santos, J. L. Brédas, M. Löglund, and W. R. Salaneck, "Electroluminescence in conjugated polymers", *Nature*, **397**, 121 (1999).

[7] V. Bulovic, V. B. Khalfin, G. Gu, P. E. Burrows, D. Z. Garbuzov and S. R. Forrest, "Weak microcavity effects in organic light-emitting devices", *Phys. Rev. B* , **58**, 3730 (1998)

[8] Geraldine Verschoor, *Private Communication* (2002-2003)

[9] A. N. Krasnov, "High-contrast organic light-emitting diodes on flexible substrates", *Appl. Phys. Lett*, **80**, 3853 (2002)

[10] C. Schmitz, M. Thelakkat and H-W. Schmidt, "A combinatorial study of the dependence of organic LED characteristics on layer thickness", *Adv. Mat.*, **11**, 821 (1999)

[11] V. Cleave, G. Yahioglu, P. Le Barny, R. H. Friend and N. Tessler, "Harvesting singlet and triplet energy in polymer LEDs", *Adv. Mat.*, **11**, 285 (1999)

[12] J-S. Kim, P. K. H. Ho, N. C. Greenham and R. H. Friend, "Electroluminescence emission pattern of organic light-emitting diodes: Implications for device efficiency calculations" , *J. Appl. Phys.*, **88**, 1073 (2000)